Semimagnetic heterostructures for spintronics

Dissertation zur Erlangung des
naturwissenschaftlichen Doktorgrades

der Julius–Maximilians–Universität
Würzburg

vorgelegt von

Taras Slobodskyy

Würzburg, 2006

Eingereicht am: ....
bei der Fakultat fur Physik und Astronomie

1. Gutachter: Prof. Dr. L. W. Molenkamp
2. Gutachter: Priv. Doz. Dr. L. Worschech
der Dissertation.

1. Prüfer: Prof. Dr. L. W. Molenkamp
2. Prüfer: Priv. Doz. Dr. L. Worschech
2. Prüfer: ....
im Promotionskolloquium

Tag des Promotionskolloquiums: ....

Doktorurkunde ausgehändigt am: ....

Contents

Introduction **1**

1 Growth and properties of diluted magnetic semiconductors **3**

1.1 Diluted magnetic semiconductor (Zn,Cd,Be,Mn)Se 3

1.1.1 Crystallographic properties of (Zn,Cd,Be,Mn)Se 3

1.1.2 Band structure of (Zn,Cd,Be,Mn)Se 5

1.1.3 Giant Zeeman splitting 8

1.2 Molecular beam epitaxy 10

1.3 GaAs - (Zn,Cd,Be,Mn)Se heterointerface 12

1.4 Reflection high-energy electron diffraction growth monitoring 15

1.5 High resolution X-ray sample characterization 16

2 Semimagnetic tunneling structures **19**

2.1 Tunnel barrier for spintronics and basics of resonant tunneling 19

2.2 Growth and characterization of all-II-VI magnetic RTDs 23

2.2.1 Superlattice approach to screening of the interface field 23

2.2.2 Big and Nano RTD structure processing 25

2.2.3 Contacting RTD devices 26

2.2.4 Current-voltage characteristic of a RTD 27
2.2.5 Collector and injector band profile 29
2.2.6 Quantum well preparation and analysis 31
2.2.7 Strain in the barriers and the quantum well 32
2.3 Magneto-transport investigations of all-II-VI magnetic RTDs 35
2.3.1 Magnetic RTD with magnetic impurities in the Quantum Well 35
2.3.2 Magnetic RTD with magnetic impurities in the Injector, Collector . . . 39
2.3.3 Magnetic RTD with magnetic impurities in the Barriers 41
2.3.4 Double quantum well triple barrier magnetic RTDs 43
2.3.5 Magnetic RTDs in series 47
2.3.6 Gated magnetic RTDs 49
2.4 Resonant tunneling through quantum dots in magnetic media 49
2.4.1 Growth of self-organized semimagnetic structures 49
2.4.2 Optical investigation of semimagnetic quantum dots 53
2.4.3 Transport investigation of quantum dots by means of resonant tunneling 56

3 (Zn,Mn)Se on silicon 59

3.1 Comparison of (Zn,Mn)Se and Silicon 60
3.1.1 Surface morphology of (Zn,Mn)Se (100) and Si (100) 61
3.2 Si (100) surface preparation and characterization 64
3.2.1 Modified RCA Si (100) surface preparation 64
3.2.2 Si (100):H surface 66
3.3 Growth of (Zn,Mn)Se on Si (100) surface 68

3.3.1 Hydrogen desorption and arsenic passivation of Si (100) surface 68
3.3.2 Si (100)-(Zn,Mn)Se interface 70
3.3.3 Growth start and MBE growth 71
3.4 (Zn,Mn)Se layer characterization 74
3.4.1 Nomarski differential interference contrast microscopy 74
3.4.2 HRXRD analysis of (Zn,Mn)Se layers 75
3.4.3 Layer relaxation 77
3.4.4 SQUID measurements 79
3.4.5 Magneto optical measurements 80
3.5 Electrical properties of Si (100)-(Zn,Mn)Se interface 81
3.5.1 Band offset 81
3.5.2 I-V characteristics 83

Summary **87**

Zusammenfassung **91**

Bibliograhy **105**

Introduction

The recent remarkable progress in the electronic industry is governed by the dictum known as Moore's law [Moo65], which predicts that the density of transistors on an integrated circuit doubles about once every two years. Since the transistor density is a rough measure of the attainable processing power, the consumers gain higher processing capabilities, smaller devices, and smaller prices per unit.

So far, manufacturers have been able to keep up with the dictum and increase transistor density by reducing element size in a planar lithography process. Current developments show that with lithographical processes, it will be possible to decrease structure sizes to the scale of a few nanometers. Soon, the dimensions of an individual device will reach a limit where quantum mechanical processes start to dominate carrier transport. Even now, as a result of interface quality and quantum mechanical effects (such as tunneling), most of the power consumed by modern electronics is wasted on parasitic currents.

Integrated circuit manufacturing is almost exclusively based on Silicon , and the material properties of this semiconductor have been well established. Manufacturing techniques are precisely controlled and employed in large-scale productions. Technologies like the silicon on insulator and strained SiGe allow for an additional time shift of the size limit for conventional electronics.

For manufacturers, it would be desirable to use elements of standard electronic circuits and extend them for performing novel functions with quantum mechanical effects in mind. The field of spintronics presents a modern answer to this challenge; it covers a wide area of investigations using the spin degree of freedom. The search for novel magnetic materials, the optimization of existing paramagnetic and ferromagnetic semiconductors and metals, and the study of carrier transport through domain walls and interfaces are only a fraction of the activities in the field of spintronics. Spin-polarized transport through interfaces is a very crucial topic, since spin-related computations may require the spin to be transferred from magnetic into nonmagnetic semiconductors which in long time scale preserve the spin orientation and in some cases the spin coherence.

II/VI diluted magnetic semiconductors are able to produce up to 100% carrier spin polarization when an external magnetic field is applied. This property allows for the generation of spin-polarized carriers and, using electric fields, their transfer into a nonmagnetic semiconductor.

Injection of spin-polarized carriers from (Zn,Mn)Se into GaAs light emitting diodes demonstrates that the spin-polarized carriers can be transferred through the heterointerface [FKR+99]. In these experiments up to 90% of the carriers preserve their spin polarization.

In this work, diluted magnetic (Zn,Mn)Se layers grown on Si (100) for the very first time are presented. These layers exhibit very good structural, optical, magnetic and electrical properties which indicate their superior quality. Results of initial transport measurements through (Zn,Mn)Se/Si interface will be discussed.

In addition we used (Zn,Mn)Se in all-II-VI magnetic resonant tunneling diodes (RTDs) to achieve spin-filtering as current was passed through spin split levels in a magnetic quantum well [SGS+03]. The RTDs present a very interesting system for investigation of spin-related phenomena. Their spin-filtering property may be used to generate spin current and to detect the spin polarization of incoming currents.

In this work, the world's first observation of spin splitting of resonances in all-II-VI magnetic RTDs is presented. In the RTDs, magnetic layers lead to spin-selective transport. Growth, electrical and structural properties of all-II-VI magnetic RTDs will be discussed, together with tunneling barriers for spintronics, spin-filtering in double and triple quantum well RTDs.

Most of the devices used in spin transport experiments are grown on almost lattice-matched substrates. For example, the lattice mismatch between (Zn,Mn)Se and GaAs can be accounted for by growing films below the critical relaxation thickness ($\sim$100 nm for a (Zn,Mn)Se layer containing 3% Mn) or compensated by adding a certain fraction of Be to the compound.

However the lattice mismatch between different layers during epitaxial growth may be used to produce self-organized structures (e.g. quantum dots). By means of resonant tunneling an individual CdSe quantum dot embedded into a (Zn,Be,Mn)Se matrix was accessed [GSS+06]. Observation of carrier-mediated local ferromagnetic interaction between magnetic atoms in vicinity of the dot will be discussed in this work.

Chapter 1

Growth and properties of diluted magnetic semiconductors

Crystal - a body that is formed by the solidification of a chemical element, a compound, or a mixture and has a regularly repeating internal arrangement of its atoms and often external plane faces [MWD03].

1.1 Diluted magnetic semiconductor (Zn,Cd,Be,Mn)Se

In Diluted Magnetic Semiconductors (DMS's), like (Zn,Mn)Se, a fraction of the atoms is replaced by magnetic ions. The ions contribute local magnetic moments to the band structure of the semiconductor. The s,p-d exchange interaction between these local moments and the band electrons gives rise to a rich spectrum of collective magnetic behavior. When an external magnetic field is applied to DMS's, they exhibit two distinct band gaps, one for each spin direction. This splitting of conduction and valance band (giant Zeeman splitting) can lead to a sizable spin polarization on the carriers in the DMS. This property is used to inject spin-polarized carriers in nonmagnetic semiconductors.

1.1.1 Crystallographic properties of (Zn,Cd,Be,Mn)Se

In compound semiconductors, such as (Zn,Be,Mn)Se, the material composition is varied in order to achieve desired compound properties. A change in the chemical composition of the compound leads to changes in electrical, magnetic and mechanical properties. Increase in Be content in the (Zn,Be,Mn)Se leads to an increase in the band gap of the compound, decreasing the lattice constant of the compound at the same time. Adding Mn in the compound changes the band gap, increasing the lattice constant concurrently.

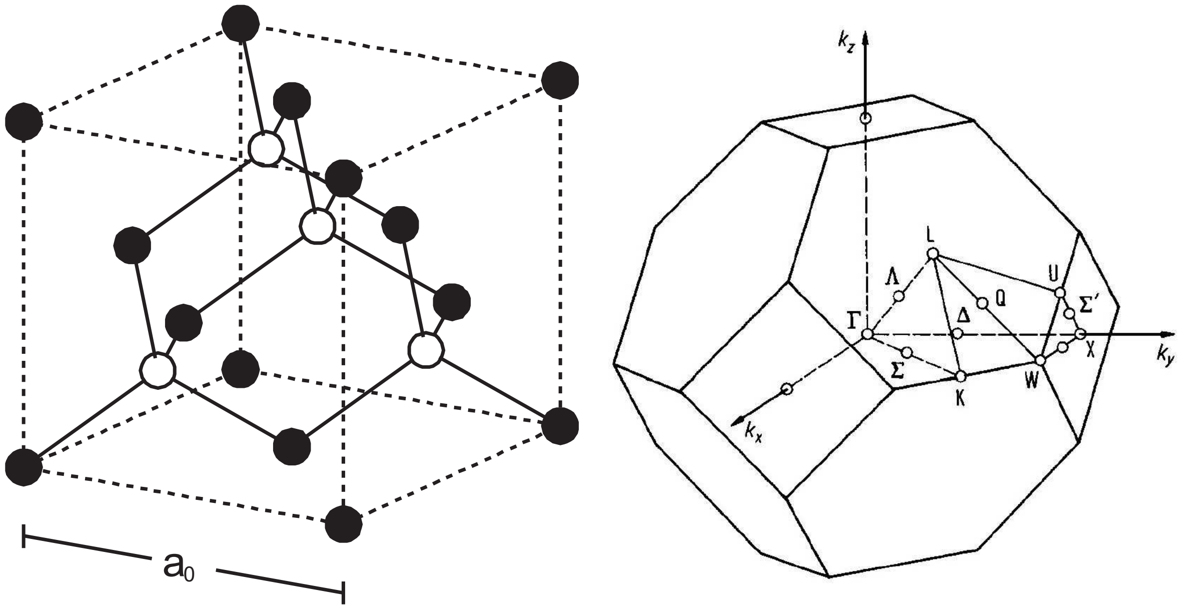

Figure 1.1: *Elementary cell of zinc-blende crystal structure and brillouin zone of f.c.c. and zinc-blende lattice.*

For most semiconductor alloys, the change in the lattice constant is governed by Vegard's law [DA91]. To understand this law, consider a semiconductor "A" with the lattice constant a_0^A and semiconductor "B" with the lattice constant a_0^B.

Then the lattice constant of the alloy $\mathrm{A}_x\mathrm{B}_{1-x}$ is given by the Vegard's law which states:

$$a_0^{AB} = a_0^A x + a_0^B (1-x) \tag{1.1}$$

For most semiconductor structures, it is imperative that the equilibrium lattice constant does not change thoughout the structure. Such structures are called lattice-matched structures. If semiconductors are not lattice-matched, the strain accumulates, and after some critical thickness, relaxes, leading to extended defects. The defects degrade the quality of the semiconductor layers. Hence, the lattice-mismatched layers must be grown below the critical relaxation thickness, when possible.

In Fig. 1.1, a zinc-blende lattice cell and the corresponding first Brillouin zone of a fcc-Bravais lattice are depicted [LB99]. Increasing Be or Mn concentrations in (Zn,Be,Mn)Se will lead to a random homogeneous replacement of group two elements; atomic positions of the group six will always be occupied by Se. The lattice constant a_0 of ZnSe is 5.65 Å. When the composition of the compound is changed, the lattice constant is changed accordingly.

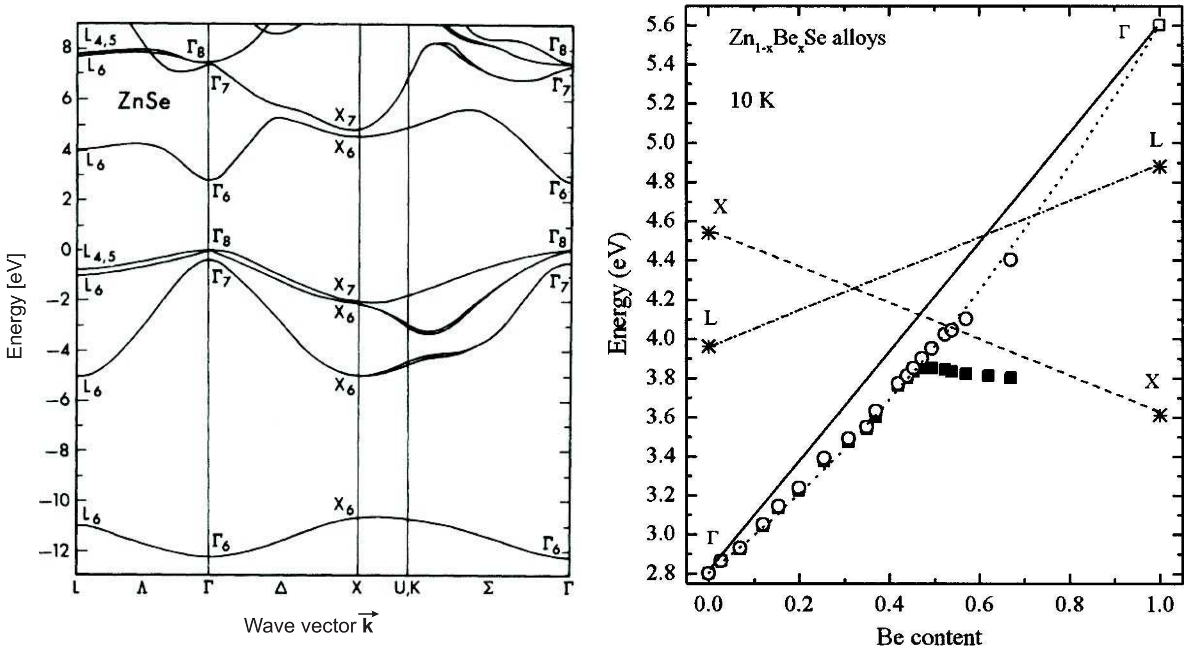

Figure 1.2: *ZnSe band structure, and the evolution of the direct band gap (O) and of the position of the main PL peak (■) as a function of the Be content in (Zn,Be)Se alloys. The direct-band gap of BeSe (□). The theoretical positions of the L and X band gaps of ZnSe and BeSe have been reported and connected by guiding lines. The dotted line represents the best fit for the direct band gap of the (Zn,Be)Se compound (after [CC76, CTF00]).*

1.1.2 Band structure of (Zn,Cd,Be,Mn)Se

The band structure of the ZnSe compound is presented on the left in Fig. 1.2; it is produced using nonlocal pseudopotential calculations [CC76]. These computations are supported by good correlation with experimental data (mainly x-ray photoemission spectroscopy and ultraviolet photoemission spectroscopy). The band structure provides evidence that ZnSe is a direct band gap semiconductor with the fundamental band gap of $\Gamma \longrightarrow \Gamma$.

The situation changes when Be is added to the compound, as is demonstrated on the right in Fig. 1.2, where the change of direct band gap at low temperatures in the (Zn,Be)Se compound at different Be concentrations is obtained from reflectivity measurements [CTF00]. The figure indicates that the fundamental band gap of (Zn,Be)Se with Be concentrations over 46% is $\Gamma \longrightarrow X$. This is an indirect band gap and leads to a rapid degradation of optical properties of the compound.

Fig. 1.2 demonstrates that the band gap change with Be concentrations does not follow a linear approximation in all ranges of compositions. While the band gap evolution has previously been extensively described [CTF00], an excellent linear fit in the range of $x < 0.60$, which will be the useful range for most applications, can be calculated from the following equation:

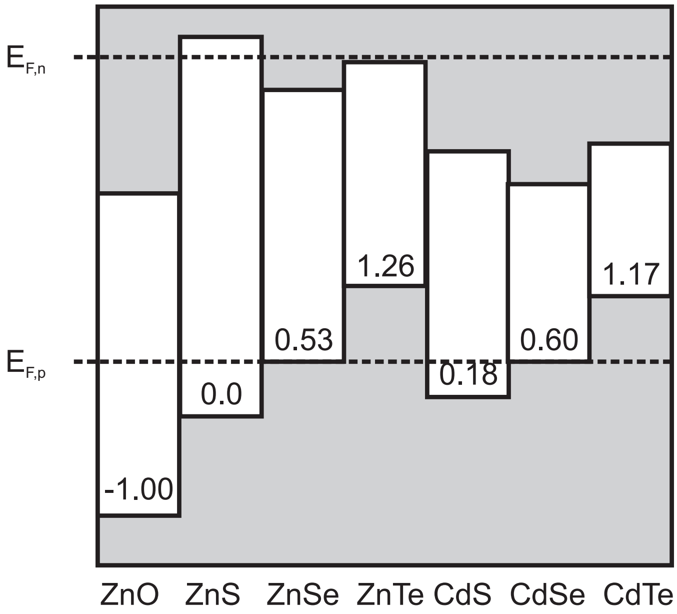

Figure 1.3: *Relative band-edge positions of various II-VI compounds (after [WZ98]).*

$$E_g^{\Gamma}(x) = 2.80 + 2.3x \quad \text{for } x \leq 0.60, \tag{1.2}$$

The band gap plays a vital role in defining optical and transport properties of semiconductors; it determines several material specific properties and plays a crucial role in the classification of semiconductors. The chemical nature of the semiconductor compound is additionally an important parameter. It determines the band offset at semiconductor interfaces and at any interfaces in general. The chemical nature defines the maximum doping based not only on the band gap but also on the relative band edge energy positions to the dopant pinning energies.

Fig. 1.3 shows approximate positions of *n*-type pining energy $\varepsilon_{F,n}$ and *p*-type pining energy $\varepsilon_{F,p}$ relative to the absolute positions of the band-edge energies. The values are obtained from first principles calculations [WZ98] and confirmed by independent maximum carrier concentration measurements for unstrained layers [ZWZ98].

For example, CdTe can be easily doped *n*- and *p*-type because the pinning energy of the dopants lies within the conduction and the valence bands of the semiconductor. Whereas ZnS can hardly be doped since the pinning energies are located deep in the band gap. ZnSe has been shown to have a maximum of over 10^{19} cm^{-3} for *n*-type and over 10^{18} cm^{-3} for *p*-type doping [GF01].

Increasing Be concentration in (Zn,Be)Se strongly influences the maximum doping by changing the chemical nature of the compound and by changing its band gap. The band gap of (Zn,Be)Se increases almost linearly with increasing Be content as we describe before. Change in the chemical nature of the compound leads to change in the valence band offset. The valence band offset of (Zn,Be)Se to ZnSe is about 40% of the total band gap change [KKL^{+}00], meaning $\triangle E_C/\triangle E_V = 60/40$.

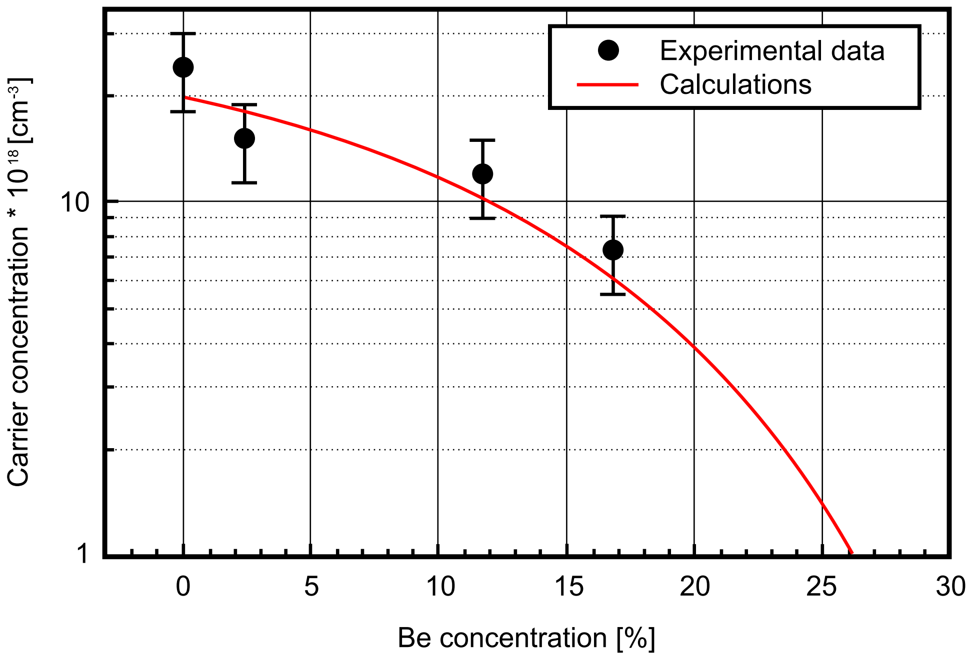

Figure 1.4: *Maximum* n*-type doping of (Zn,Be)Se (after [Reu00]).*

The resulting dependence of the doping on the Be concentration is presented in Fig. 1.4, where the values depicted by black dots with error bars were obtained using Hall measurements. The red line represents a fit obtained from defect model calculations. A reference energy parameter $E_{SI} = 2.26 + 0.9x$ [eV] and the maximum doping concentration d= 3×10^{19} cm^{-3} were used for the calculations [Reu00].

Since the band gap change alone can not be responsible for the rapid degradation of the doping in the samples [TMM64], the amphoteric native defect model [Cha94] is the more appropriate description of the process. It accounts for a formation of DX-like deep donor centers in compound semiconductors. Such defect centers lead to rapid doping degradation [PC95]. Different solubilities of dopants may be important factors influencing the (Zn,Be)Se doping [LdWNP91].

The band gap of the ZnSe compound may be changed by adding a fraction of Cd to the compound [TBN^{+}91]; this reduces the band gap, and a linear approximation of the concentration dependence fits well, up to 20%.

For a given Cd concentration the maximum width of a pseudomorphic layer is limited due to the strain buildup. However, since (Zn,Cd)Se accumulates compressive strain, which is opposite to tensile strain in (Zn,Be)Se, the materials can be combined to grow strain balanced structures with large band gap variations.

The valence band offset of (Zn,Cd)Se to ZnSe is about 13% of the total band gap change [GaAFL^{+}00] or $\triangle E_C/\triangle E_V = 87/13$. The values change slightly when a magnetic field is applied [YSP^{+}97].

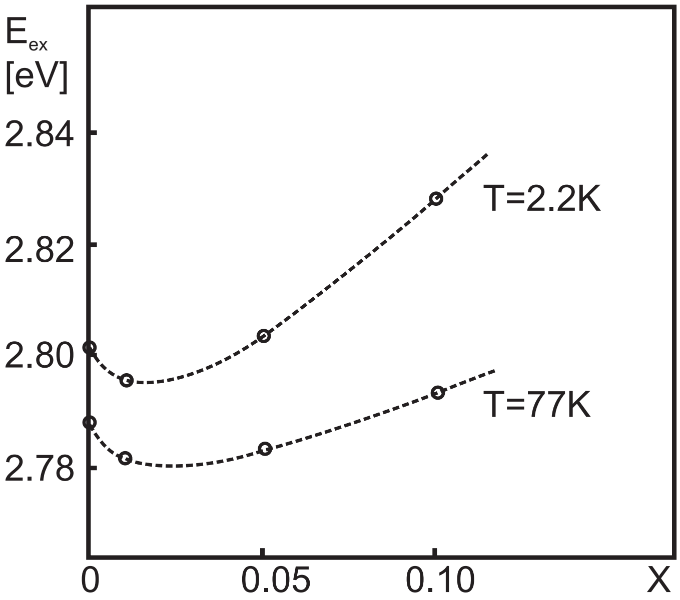

Figure 1.5: *Composition dependence of the free exciton energy E_{ex} of (Zn,Mn)Se without a magnetic field. The lines are eye guides (after [TDD83]).*

Adding Mn into a ZnSe compound will change the properties of the compound as well [TDD83]. Without an applied magnetic field, the band gap of the compound changes as is reflected in Fig. 1.5. The change of a free exciton energy with the change in the concentration is also reported in the figure; as it is evident, that the trend reflects a change in the band gap.

The energy of the band edge increases linearly with increasing Mn concentrations above 10%. The curving of the energy gap below 10% is explained in terms of magnetic and chemical disorders in the DMS [Tak99]. This means that the density of states changes with the magnetic ion mole fraction and with the exchange strength.

More details on the (Zn,Mn)Se band gap dependence without an external magnetic field being applied can be found in [BBK$^+$86]. The magnetic nature of the Mn will lead to the strong magnetic field dependence of the band gap for different spin orientations.

1.1.3 Giant Zeeman splitting

A paramagnetic DMS in a magnetic field has a spin splitting of the levels in the conduction and valence band that is much larger than the value caused by the regular Zeeman term and is called "giant Zeeman splitting".

In DMS's, a strong exchange interaction exists between the localized d-electrons of magnetic ions and the band electrons. When an external magnetic field is applied to such materials, the

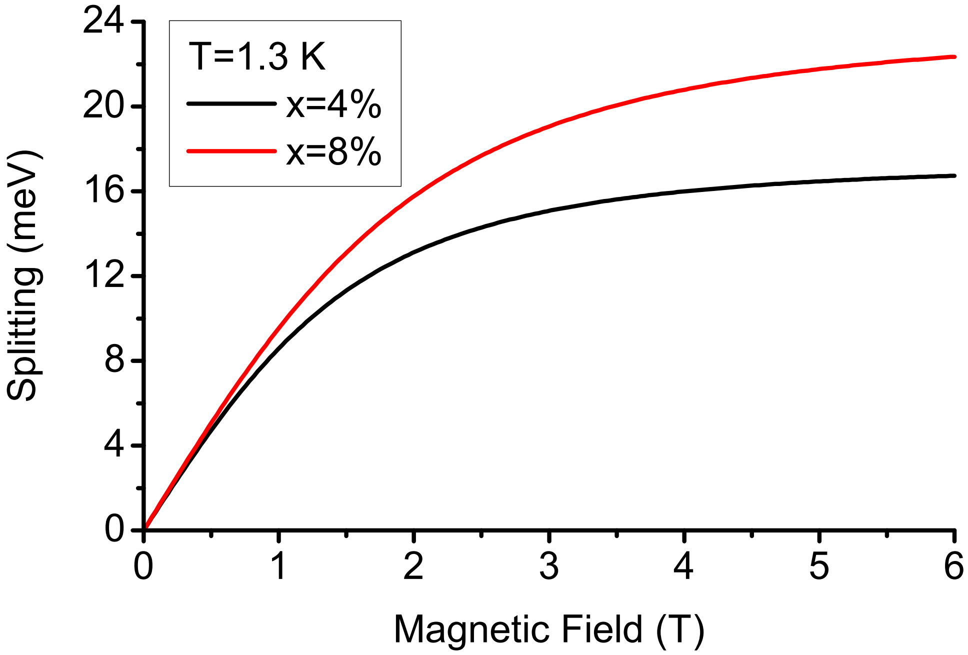

Figure 1.6: *Simulated giant Zeeman splitting of the conduction band in an external magnetic field for two different Mn concentrations*

net alignment of the ion spins leads to the splitting of energy levels of free carriers with opposite spin orientations. In this case, the splitting of spin levels at the bottom of the conduction band ΔE of the DMS as a function of the magnetic field *B* is given by a modified Brillouin function [GPF79].

$$\Delta E = N_0\alpha\, x\, s_0 B_s\left(s\, g\, \mu_B B / k_B(T+T_{eff})\right) \tag{1.3}$$

where $N_0\alpha$ is the s-d exchange integral, x, s and g are the manganese concentration, manganese spin, and g-factor, respectively, and μ_B is the Bohr magneton. B_s is the Brillouin function of the spin s . s_0 and T_{eff} are the effective manganese spin and the effective temperature, respectively. These phenomenological parameters are needed to account for antiferromagnetic $Mn^{++} - Mn^{++}$ exchange interactions [TvODP84, Fur88]. Functional dependencies of these parameters on composition based on the data for $Zn_{1-x}Mn_xSe$ epilayers is given by $S_{eff} = -0.804 + 0.364/(x - 0.109)$ and $T_{eff} = 47.2x - 281x^2 + 714x^3$ [KYK$^+$02].

Fig. 1.6 illustrates the simulated giant Zeeman splitting of the (Zn,Mn)Se conduction band in an external magnetic field for two different Mn concentrations using Eq. 1.3. As it is shown, the giant Zeeman splitting increases with increasing concentration. At the same time, the fraction of atoms coupled in antiferromagnetic $Mn^{++} - Mn^{++}$ exchange interactions increases as well. Therefore, increasing the Mn concentration up to approximately 12 percent increases the value of the splitting, however further increase in the concentration leads to a suppression of the effect.

Giant Zeeman splitting at low magnetic fields increases with decreasing temperatures. Since the splitting is a collective influence of oriented Mn^{++} atoms, increased temperature disorients the manganese system and, therefore, decreases the effect of the magnetic field. Hence, in order to reach the same giant Zeeman splitting higher magnetic fields are needed. This does not apply to the entire temperature range since temperatures below T_{eff} do not have much influence on the value of the splitting. In this case, the constant T_{eff} term dominates and the decreased temperature does not increase the value of the giant Zeeman splitting in a constant magnetic field. This effect can be qualitatively understood as an interaction between manganese atoms that dominate small temperature disorder (see Eq 1.3).

1.2 Molecular beam epitaxy

Molecular beam epitaxy (MBE) is a technique for epitaxial growth via the interactions of one, or several, molecular or atomic beams that a on the surface of a heated crystalline substrate. In Fig. 1.7 a scheme of a RIBER 2300 MBE system is shown. The solid source materials are placed in evaporation cells to provide an angular distribution of atoms or molecules in the beam. The substrate is heated to the necessary temperature, and when needed continuously rotated to improve the growth homogeneity.

Taking into account that the mean free path λ of particles increases with decreasing pressure, the molecular beam condition that the mean free path of the particles should be larger than the geometrical size of the chamber $\lambda > L$ is easily fulfilled if the total pressure does not exceed about 10^{-5} Torr. Also, the condition for growing a sufficiently clean epilayer must be satisfied, meaning that the monolayer deposition times of the beams t_b and the background residual vapor t_{res} must meet the relation $t_{res} < 10^{-5}t_b$. For a typical zinc flux Γ of 10^{19} atoms $m^{-2}s^{-1}$ and for a growth rate of 1 $\mu m/h$, the conclusion is that $P_{res} \leq$ is 10^{-11} Torr. Considering that the sticking coefficient of Zn on the ZnSe surface under normal growth conditions is about 0.63 and the sticking coefficient of the typical residual gas is much less, the strength of the above condition can be softened; however, ultra high vacuum (UHV) is required.

MBE systems permit control of the composition and doping of the grown structure at a monolayer level by changing the incoming beams. This is done by changing the cell temperatures and opening and closing mechanical shutters. The operation time of a shutter of approximately 0.1 s is normally much shorter than the time needed to grow one monolayer (typically 1-5 s). The careful variation of the temperatures of the cells via PID controllers permits control of the flux of every component or dopant that is better than 1%.

The UHV environment of the system is also ideal for many in-situ characterization tools, such as reflection high-energy electron diffraction (RHEED). An oscillation of the RHEED signal exactly corresponds to the time needed to grow a monolayer, and the diffraction pattern on the RHEED window gives direct indication over the state of the surface, as will be described later.

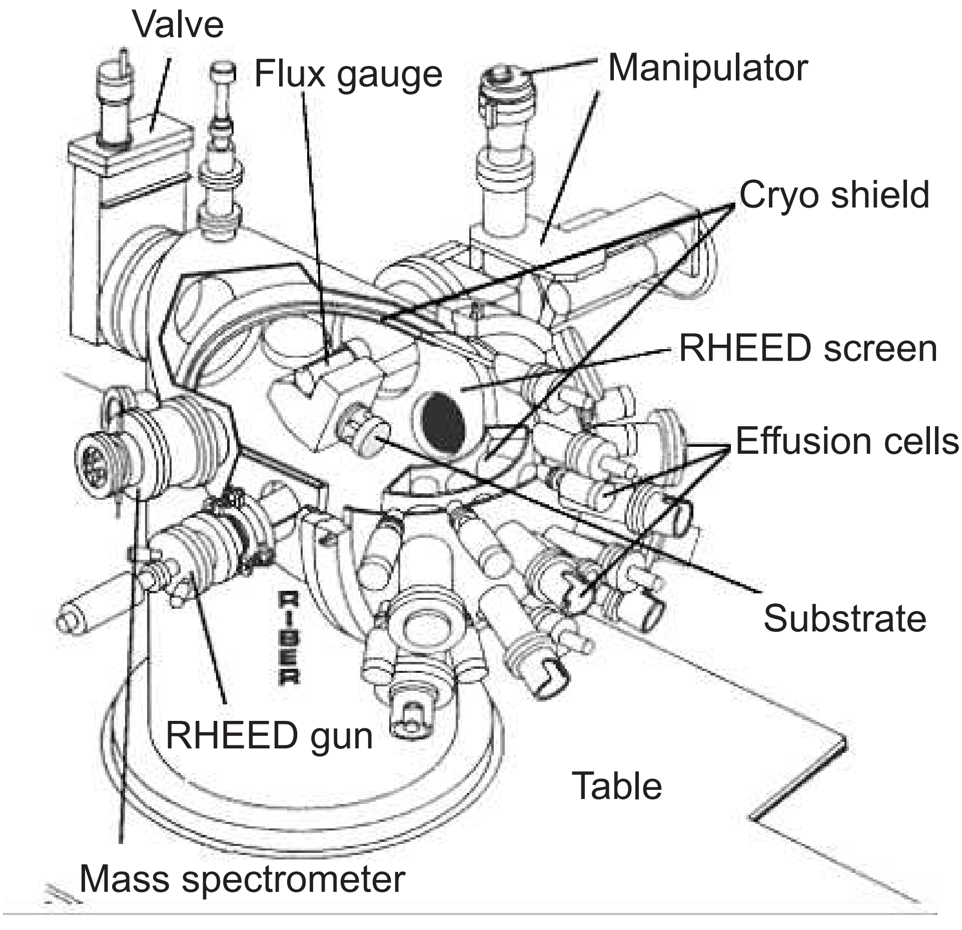

Figure 1.7: *RIBER MBE system.*

The process of epitaxial MBE crystal growth can be described using the generalized Burton-Cabrera-Frank theory for growth and equilibration on stepped surfaces [MBV91]. The theory explains the dynamic and process in so-called edge flow mode.

During II-VI MBE, the group VI to group II atomic flux ratio plays an important role. It is generally accepted that flux ratios of about two produce a higher quality of epitaxial layers at standard ZnSe growth temperatures of 300 °C [WEWR00]. Since for atomic flux ratios smaller than two, the Zn sticking coefficient is smaller than the maximum one, not all Zn is incorporated into the crystal, and a substantial fraction of the atoms is desorbed from the substrate. This leads to an increase in the stacking fault density.

At atomic flux ratios above two, the growth speed is controlled by Zn flux and extra Se is desorbed from the surface [RWWE96]. This process leads to the smallest stacking fault density. Since Zn defines the MBE growth speed, precise control over the cell temperature is vital for epitaxial growth. When the Se to Zn atomic flux ratio exceeds 4, the desorption rate for Se atoms becomes smaller than the incoming flux and the stacking fault density slowly rises again [Gai94].

1.3 GaAs - (Zn,Cd,Be,Mn)Se heterointerface

Since the most suitable and commonly used substrates for MBE of (Zn,Be,Mn)Se based II/VI compounds, are GaAs wafers, which belong to the III-V group, it is necessary to accept advantages and disadvantages of such a partnership. Among the main advantages are a very good matching of the lattice constants and a commercial availability of high-quality epiready wafers. In the case of ZnSe the lattice mismatch to the substrate is 0.267%; this means that layers as thick as 150 nm can be grown without relaxation [PJJ$^+$98, LLV02]. Moreover, a (Zn,Be)Se layer containing 2,83% Be is lattice-matched to the GaAs substrate. However, composition, doping and quality of the layer will influence the relaxation process [WON$^+$00]. One of the most prominent disadvantages of the interface is a heterointerface potential which is discussed later in this Section.

GaAs substrate preparation is initiated by mounting GaAs wafers on molybdenum blocks and transferring them into the UHV MBE system. Indium is used as an adhesive to mount the substrates on the molybdenum blocks by heating it to a temperature of about 210 °C.

The layers are deposited in a multichamber MBE system, thus allowing UHV transfer between the various growth chambers. Growth is performed in RIBER 2300 systems using elementary sources (6N purity). Se and As are deposited from EPI valved cracker cells and all other elements from standard effusion cells.

After degassing at 300 °C for 15 min, the molybdenum blocks are transferred to the III–V growth chamber. The oxide layer is removed by heating the samples to 620 °C for 10 min.

Already at 450 °C, the samples are subjected to constant As flux to compensate As desorption at higher temperatures and prevent formation of Ga droplets on the surface. At 582 °C, oxide desorption can be observed by the transition of a not reconstructed RHEED image to (2x4) reconstruction. The surface at this step has a roughness defined by the inhomogeneity in the oxide layer thickness. 300 nm of GaAs subsequently grown at 600 °C create an atomically flat surface.

When the growth is finished, the samples are cooled under As flux. Depending on the minimum temperature until which the As is supplied during the cooling process, it is possible to prepare two surface reconstructions (2x4) and c(4x4). The first one is prepared by removing As flux at 550 °C and the second by removing the flux at 450 °C.

There is a distinct difference between the two reconstructions in terms of the ZnSe growth start. c(4x4) reconstruction leads to a decreased amount of dislocations at the interface, but at the same time, due to uniform interface bondings, it increases the heterointerface potential. On the other hand, layers grown on (2x4) reconstructed surfaces exhibit higher dislocation density but decrease heterointerface potential due to a mixture of interface bondings.

A very significant feature of the interface is the strong interface effect on the electrical characteristics of ZnSe/GaAs heterojunctions [SHG^{+}99]. The effect appears as a result of the interface influence on the charge distribution in the near interface region.

In the first instance using chemical trends and cation d orbitals, the natural band offsets at II–VI and III–V semiconductor interfaces can be calculated [WZ98]. Combined with the effective dipole theory for band lineups in semiconductor heterojunctions [RC87], these calculations lead to reliable values of band discontinuities at an ideal ZnSe/GaAs interface.

A simulation of the band bonding at the interface using a one-dimensional poisson solver [sim] is shown in Fig. 1.8. At first glance, a tunnel barrier at the interface may be observed. The barrier is created due to the conduction band discontinuity at the interface. This band discontinuity is strongly dependant on the Se/Zn beam pressure ratio [NVM^{+}94] during epitaxial growth due to local interface composition in heterovalent heterostructures.

As Li *et al.* have shown [LP94], GaAs-Se highly ordered structures must be avoided because of to island formation. They observed growth of three-dimensional ZnSe islands several monolayers high on the Se-terminated GaAs surface, while much of the surface remained uncovered. The authors suggest that an initial exposure of GaAs to Zn may prohibit the formation of these islands.

In the experiments presented here, Zn rich interfaces were prepared by exposing the GaAs surfaces to Zn flux for 40 second. This allowed for much lower stacking fault densities as compared to Se-rich interfaces [HPS^{+}97]. The ZnSe/GaAs valence band offset at such an interface, as was determined by deep-level transient spectroscopy and photocurrent measurements [SAD^{+}99], was assumed to be $\triangle E_V = 1.00 \pm 0.05$ eV.

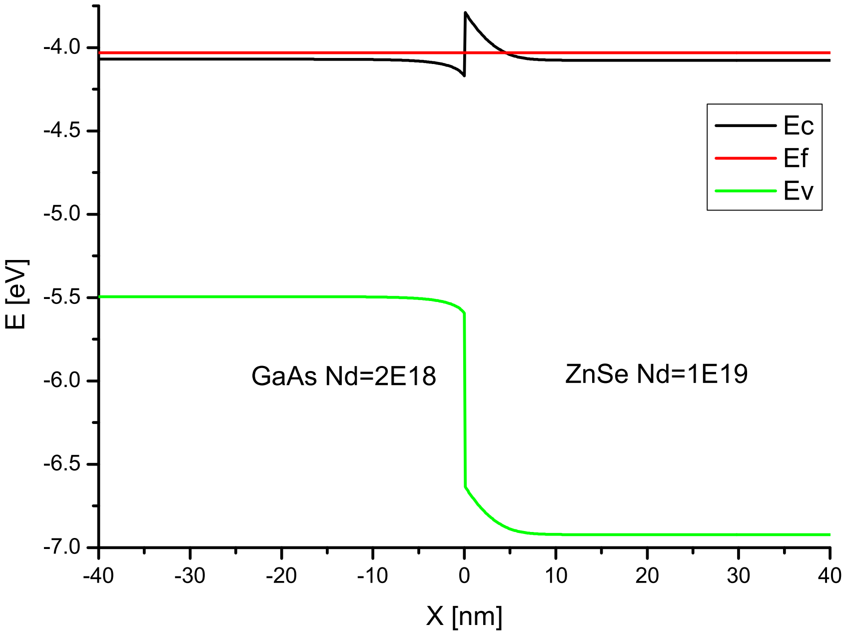

Figure 1.8: *Calculated band diagram for GaAs($n = 5 \times 10^{18}$ cm^{-3}) - ZnSe($n = 1 \times 10^{19}$ cm^{-3}) at 0.0 V applied bias.*

Since lattice mismatch at the interface induces strain in the epilayer, and the band discontinuities depend strongly upon the specific strain conditions [dWM86], details of the strain accumulation and relaxation will lead to a significant change in the band offset.

Interface chemistry plays an important and not always trivial role in the interface formation. Influence of the interface chemistry can be used to control and tune band offsets in GaAs/ZnSe(001) heterovalent heterostructures. By varying Zn and Se surface bonding, it is possible to control the valence band offsets in the heterostructures in the range of 0.6 to 1.1 eV [FAFF99].

Finally, ZnSe layers grown on GaAs substrates thicker than their critical thickness will relax, and a part of the strain will induce stress in GaAs substrates [CNCRF^{+}98]. The latter will change the band offset, as was discussed earlier.

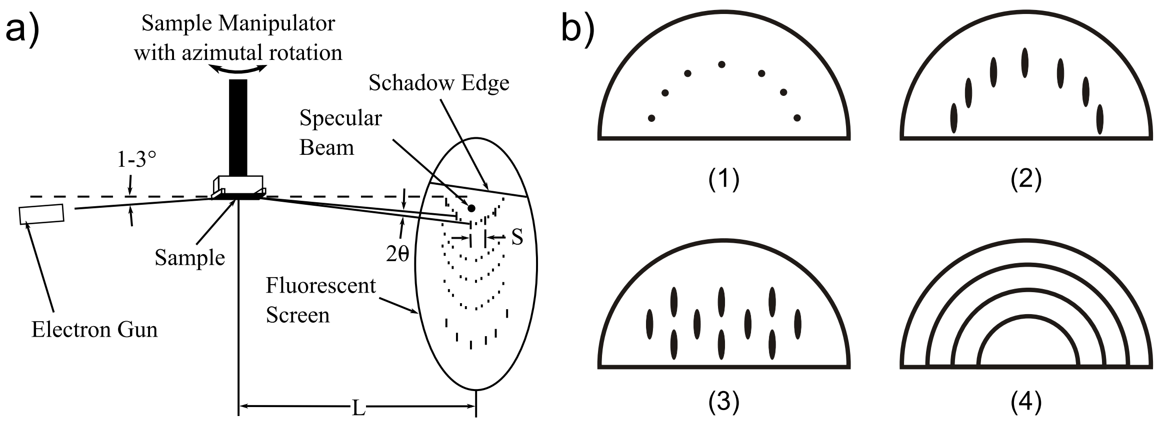

Figure 1.9: *a) Schematic view of a RHEED setup. b) typical diffraction patterns: (1) - from ideal smooth surface, (2) - from real smooth surface, (3) - transition through 3D clusters, (4) - from polycrystalline or textured surface.*

1.4 Reflection high-energy electron diffraction growth monitoring

Reflection High-Energy Electron Diffraction (RHEED) is a powerful technique for studying the surface structures of flat surfaces [BME78] as well as surface phase transitions [ZLEKEA99]. RHEED is sensitive to surface changes that are either due to structural changes or due to adsorption. Thus, it is widely used as an in-situ probe to monitor MBE growth of thin films.

The geometry of a RHEED setup is relatively simple (see Fig. 1.9(a)). An accelerated electron beam (5-100 keV) is incident with the surface at a glancing angle (<3 deg) and is reflected. The high-energy electrons result in a high-penetration depth; however, because of the glancing angle of incidence, only a few atomic layers are probed. This is the reason for the high-surface sensitivity of RHEED. Upon reflection, electrons diffract, forming a pattern that depends on the structure and the morphology of the probed surface.

A comparison between sketches of RHEED patterns obtained for different surfaces is shown in Fig. 1.9(b). Conceptually, perfectly flat surfaces should result in diffraction patterns that consist of spots arranged on Laue rings (see Fig. 1.9(b)(1)). However, because of the non-idealities in the electron beam and the sample's surface, streaks, instead of spots, can be observed in Fig. 1.9(b)(2). The distance between the streaks is an indication of the surface lattice unit cell size. An example of patterns produced by 3D structures can be seen in Fig. 1.9(b)(3). In the case of polycrystalline or textured surfaces diffraction rings may be observed (see Fig. 1.9(b)(4)). All these types of the patterns are frequently observed during MBE growth, indicating either expected growth conditions or an unwanted deviation from the growth parameters.

Despite the popularity of RHEED, there is no complete formal theory for it. However, a number of simplified kinematical approaches have been introduced, which are useful for understanding the basic idea of RHEED. They are sufficient for the determination of the unit cell dimension, the crystal orientation, and the crystal shape. The lack of a formal theory is the reason for the debate over the interpretation of RHEED results [MB96].

The left side of Figure 1.9 gives some insight into the basic analysis of results seen on the RHEED screen. The Bragg relation for first order diffraction is $2d\sin\theta = n\lambda$. By substituting $\tan 2\theta \cong 2\theta$ and $\theta \cong t/2L$, and since L is long compared to t, the equation can be simplified to $t = \lambda L/d$, where t is the distance between spots at the screen, and d is the reciprocal space distance. This simplified equation can be used to determine the reciprocal lattice separation giving rise to the adjacent spots in the first Laue Zone (the zone of diffraction spots closest to the shadow edge on the screen). The inverse of this separation is the associated real space separation along the crystal direction, which is defined by the two adjacent spots.

RHEED intensity oscillations recorded during sample growth present an additional powerful tool for understanding growth mechanisms during MBE. There is a close relationship between the RHEED intensity oscillations and the growth rate of MBE films. Specifically, a period of the intensity oscillations of the specular diffraction spot corresponds to the time required to grow exactly 1ML of crystal over a broad range of growth conditions.

Because the RHEED oscillations are recorded without the substrate rotation, the results are particularly susceptible to variations in growth rate across the substrate [HBH^{+}03]. When the substrate is rotating under normal growth conditions, the variations have a much smaller effect.

The most obvious inaccuracy is that the growth rate at the substrate center is one that most closely approximates the growth rate that is produced on a larger rotating substrate. This implies that the electron beam must be located in the center of the substrate. By moving the electron beam on the substrate, a substantial growth rate variation of up to several percent and in a direction perpendicular to the electron beam path can be observed.

1.5 High resolution X-ray sample characterization

High resolution X-ray diffraction (HRXRD) is a versatile and non-destructive technique that reveals detailed information about the chemical composition and crystallographic structure of natural and manufactured materials.

Due to the characteristic X-ray wave length of around 0.15 nm (for CuK$_{\alpha}$), the matter is not seen homogeneously, but, instead, its atomic nature is revealed. If the atoms are arranged periodically in a crystal, then interference plays a crucial role in spreading the beam. Since a crystal lattice is a regular three-dimensional distribution of atoms in space, the atoms are arranged so that they form a series of parallel planes separated from one another by a distance d. The distance varies according to the nature of the material. For any crystal exists a set of planes in a number of different diffraction orientations, each with its own specific d-spacing.

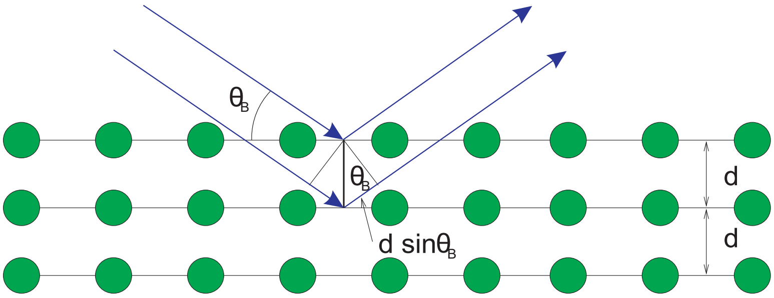

Figure 1.10: *Geometrical presentation of Bragg's law.*

When a monochromatic X-ray beam with wavelength lambda is projected onto a crystalline material at an angle Θ, diffraction occurs only when the distance traveled by the rays reflected from successive planes differs by a complete number n of wavelengths.

This effect is known as Bragg's law and is demonstrated in Fig. 1.10. An incoming X-ray beam scatters on the surface of ordered atoms, and the scattered beam is created by a constructive interference of secondary beams produced by each of the atoms. The new direction of the beam is defined by the path difference of two beams created by parallel atomic layers.

The mathematical form of the law is written as:

$$2 \times d \times \sin\theta_B = n \times \lambda \tag{1.4}$$

where

θ_B - Bragg's angle
λ - wave length
d - distance between atomic layers
n - integer number

By varying the angle theta, the Bragg's law conditions are satisfied by different d-spacings in crystalline materials. Plotting the angular positions and intensities of the resultant diffracted peaks of radiation produces a pattern which is characteristic of the sample. When a mixture of different phases is present, the resultant diffractogram is formed by the addition of the individual patterns. Based on the interpretation of the diffractogram, a wealth of structural, physical and chemical information about the material investigated can be obtained.

In the investigations described here, the PANalytical's X'Pert PRO X-ray diffraction system was used to characterize properties of MBE produced films and their interfaces. The system is equipped with automation software and is especially suitable for thin film analysis applications. Main applications of the device include rocking curve analysis and reciprocal space mapping, reflectometry and thin film phase analysis and residual stress and texture analysis.

The measurement setup places a limitation on the minimum planar size of investigated surfaces by defining the beam spot size and minimum intensity of the collected signal. The limitation

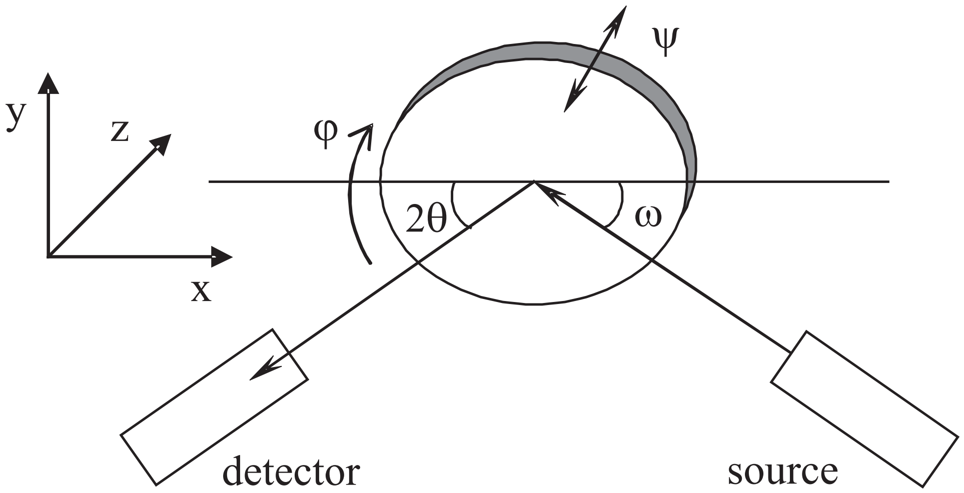

Figure 1.11: *HRXRD setup configuration.*

on the maximum access depth and complexity of investigated structures is much stronger. The depth limitation comes from X-ray penetration depth into the sample. The setup used allowed for an investigation of structures with a thickness up to more than 4 μm.

A schematic plot of the experimental setup is shown in Fig. 1.11. By varying the angles ω, 2θ, φ and ψ, it is possible to scan different diffraction angles moving in the reciprocal space. The entire axis must be coordinated to move in reciprocal space during the measurements. Therefore, in order to take a scan in 004 reflex, ω and 2θ angles have to be changed simultaneously.

Dynamic simulations of the diffractograms were performed using "X'Pert Epitaxy" software version 4.1. The program has been specially developed to display and analyze data scans from substrates and heteroepitaxial layers. It allows for easy calculations of layer composition, relaxation, thickness and other sets of parameters based on diffraction data.

The correct interpretation of results of HRXRD experiments is impossible without the knowledge of right material parameters. A list of material parameters for II-VI material systems can be found in other sources [Reß98].

Chapter 2

Semimagnetic tunneling structures

Since most of the ways of creating spin-polarized carriers used in the modern research have limited control over polarization of created carriers, it would be desirable to have a voltage controlled spin polarized injection and detection [DiV99].

In the following we will describe a novel way of creating and detecting spin polarization of carriers using resonant tunneling devices (RTDs) [SGS^{+}03]. All-II-VI semiconductor RTDs based on the (Zn,Be,Mn)Se material system, containing dilute magnetic semiconductor (DMS) in the quantum well were fabricated. When subjected to an external magnetic field, the resulting spin splitting of the levels in the quantum well leads to a splitting of the transmission resonance into two separate peaks. This is observed trough a distinct splitting of the resonance peaks on I-V characteristics on the device.

Detailed simulations of the I-V characteristics show an excellent agreement with experiment. Extracted values of the giant Zeeman splitting agree well with the magnetic field dependence expected from (Zn,Mn)Se DMS. This is interpreted as evidence of tunneling transport through spin polarized levels.

Furthermore, details of the growth and fabrication of the RTDs, principles of designing the band profile and the strain accumulation during the growth will be described. Analysis of the I-V characteristics of the RTDs for the devices with varied structure will be presented.

2.1 Tunnel barrier for spintronics and basics of resonant tunneling

The tunneling process is a very fundamental quantum mechanical effect. It is involved in many areas of modern device design in form of tunnel junctions, Esaki and Zener diodes and the like.

Tunneling magnetoresistance is being used in memory storage. The most recent discovery of the tunneling anisotropic magneto resistance hints at a number of new discoveries related to tunneling as research is moving towards nanoscale devices.

It is well documented that the conductivity mismatch problem presents a fundamental obstacle for electrical spin injection from a ferromagnetic metal into a diffusive semiconductor [SFM$^+$00]. Furthermore, it has been suggested that the tunnel contacts can serve as a solution to the conductivity mismatch problem [Ras00]. Later, it was found that the conditions for efficient spin injection from a ferromagnetic metal into a semiconductor include a spin-dependent interface resistance (preferably a tunnel junction) [FJ01]. In fact, using a tunnel contact, it is possible to create a highly spin-polarized room-temperature tunnel injector for semiconductor spintronics, as it was recently demonstrated using MgO(100) [JWS$^+$05].

A classic example of the use of tunneling for spin-filtering is the study of Perel' *et al.* [PTY$^+$03]. They investigated the problem of electron tunneling through a symmetric semiconductor barrier based on zinc-blende structure material and concluded that the k^3 Dresselhaus terms in the effective Hamiltonian of bulk semiconductor of the barrier results in a dependence of the tunneling transmission on the spin orientation. The resulting difference of the transmission probabilities for opposite spin orientations can reach several percent for a reasonable width of the barriers.

Tunneling is the quantum-mechanical effect of transmission through a classically-forbidden energy state. This means that a particle can overcome barriers higher than the energy of the particle which would not be possible in a classical case. The phenomenon has to do with the wave nature of the particle. In other words, the wave function can enter into the barrier and into existing states on the other side of the barrier. Hence, availability of states on both sides of the barrier is necessary for tunneling to occur. Based on this, the barrier can be described as a region with no available states for a particle to reside in.

While the most correct description of the tunneling process may be obtained using a quantum mechanical formalism (e.g. transfer matrix method), in most cases simplified equations are sufficient approximations to describe the process. While many approaches have been proposed in early days, only the most commonly accepted one will be considered here.

The generalized formula for the electric tunnel effect between similar electrodes separated by a thin insulating film [Sim63] is written as follows:

$$j = (6.2 \times 10^{10}/\Delta s^2)\{\varphi_I \exp(-1.025\Delta s \varphi_I^{\frac{1}{2}}) - (\varphi_I + V)\exp[-1.025\Delta s(\varphi_I + V)^{\frac{1}{4}}]\} \quad (2.1)$$

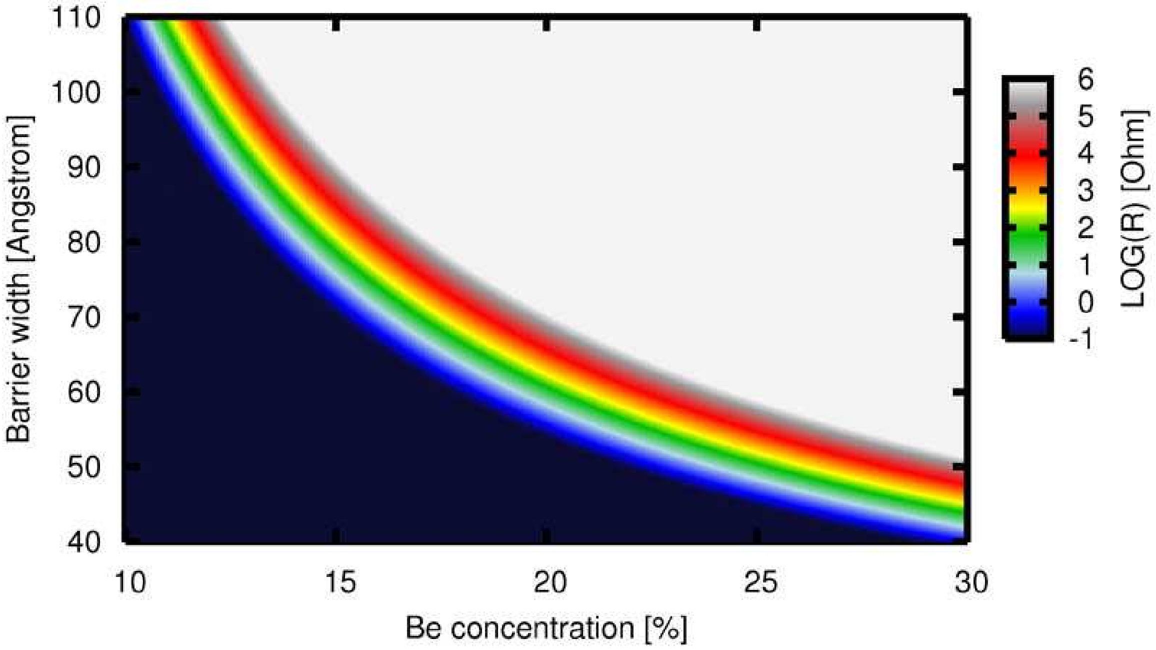

Figure 2.1: *Resistance of a (Zn,Be)Se tunneling barrier of size 100x100 micron at 100 [mV] bias*

where

$$\varphi_I = \varphi_0 - V\frac{s_1+s_2}{2s} - 5.75\frac{\Delta s}{K}\ln[\frac{s_2}{s_1}\frac{s-s_1}{s-s_2}]$$

and

$$\left.\begin{array}{l} s_1 = 6/K\varphi_0 \\ s_2 = s[1-46/(3\varphi_0 Ks + 20 - 2VKs)] + 6/K\varphi_0 \end{array}\right\} \quad V < \varphi_0$$

$$\left.\begin{array}{l} s_1 = 6/K\varphi_0 \\ s_2 = (\varphi_0 Ks - 28)/KV \end{array}\right\} \quad V > \varphi_0$$

where j [A/cm^2] is the tunneling current, K is a dielectric constant, φ_0 [eV] is the height of a rectangular barrier, s_1 and s_2 are the corrections for image force and $\Delta s = s_2 - s_1$ is the real width of the tunnel barrier at the Fermi level.

Applying equation 2.1 to (Zn,Be)Se/ZnSe yields the color plot shown in Fig. 2.1, where the resistance of a single (Zn,Be)Se tunnel barrier for conduction electrons in ZnSe is summarized. The plot shows the resistance of a tunnel barrier with the area of 100x100 micron at different Be concentrations. The Fermi level is assumed to be pinned to the bottom of the conduction band. The change of the band gap with composition is assumed to follow Eq. 1.2. The conduction band offset is assumed to be 60% of the total band gap change [KKL$^+$00], as was explained in Section 1.1.2.

Fig. 2.1 presents an easy way to estimate the resistance of a tunnel junction. The rainbow colors reflect experimentally the most relevant parameters. While a junction with parameters moving further into a white area will have a tunneling resistance too large for reliable measurements at the given dimensions, the junction with parameters corresponding to the black area will result in a very low device resistance , thus leading to difficulties in performing reliable experiments.

In this context, it must be mentioned that the resistance of a tunnel barrier is strongly bias dependant. Therefore, results presented in Fig. 2.1 change when different bias is applied. Specifically, increasing the applied bias results in an exponential decrease of resistance of the tunnel barrier. The value of 100 mV is chosen to reflect the most common experimental conditions.

A spin-selective tunnel barrier produces a spin-polarization of the transmitted current depending on barrier parameters and applied voltage. This means that the spin-polarization of the transmitted current strongly depends on the voltage drop over the device. The smaller the height of the spin-selective tunnel barrier, the stronger the voltage dependence.

This case can be illustrated by a spin-selective tunnel barrier with a certain height for carriers with spin-down orientation and no tunnel barrier for spin-up carriers. Then the spin-down tunneling current $j_\downarrow$ is given by equation 2.1. At the same time, the spin-up current $j_\uparrow$ is defined as the product of voltage drop over the barrier and the spin channel resistance. Therefore, resulting spin-polarization of the current is given by $\alpha \equiv \frac{j_\uparrow - j_\downarrow}{j_\uparrow + j_\downarrow}$.

As the voltage drop rises, the tunneling resistance of the spin-down channel decreases. Taking into account that the resistance of the spin-up channel remains the same, the total spin-polarization of the transmitted current α decreases as well.

Other types of tunneling devices such as Schottky barriers and interband-tunneling devices [KOT$^+$01] may be successfully used to produce and manipulate the spin orientation of carriers. When dealing with compound semiconductors such as (Zn,Be)Se, it is important to take into account that layers with different composition usually have different lattice parameters. This difference consequently induces strain in the lattice as mentioned in section 1.3. As a result of the accumulated strain, the lattice of a layer with a thickness exceeding a certain critical value relaxes, thus producing multiple defects. To avoid such a scenario, the width of the tunnel barrier should be kept below the critical thickness.

The most practical solution for the calculation of the critical thickness can be expressed in the following form. When introducing misfit parameter f_m defined as

$$f_m = \frac{a_l - a_{sub}}{a_{sub}}$$

the critical thickness h_c is calculated from

$$h_c = A^* f_m^{-2/3} \tag{2.2}$$

where A^* is an adjustable parameter [CSBB94].

By adjusting the empirical parameter to $A^* = 0.45$ Å, a very reasonable agreement with experimental data can be achieved for most of II-VI semiconductor epilayers [PJJ$^+$98].

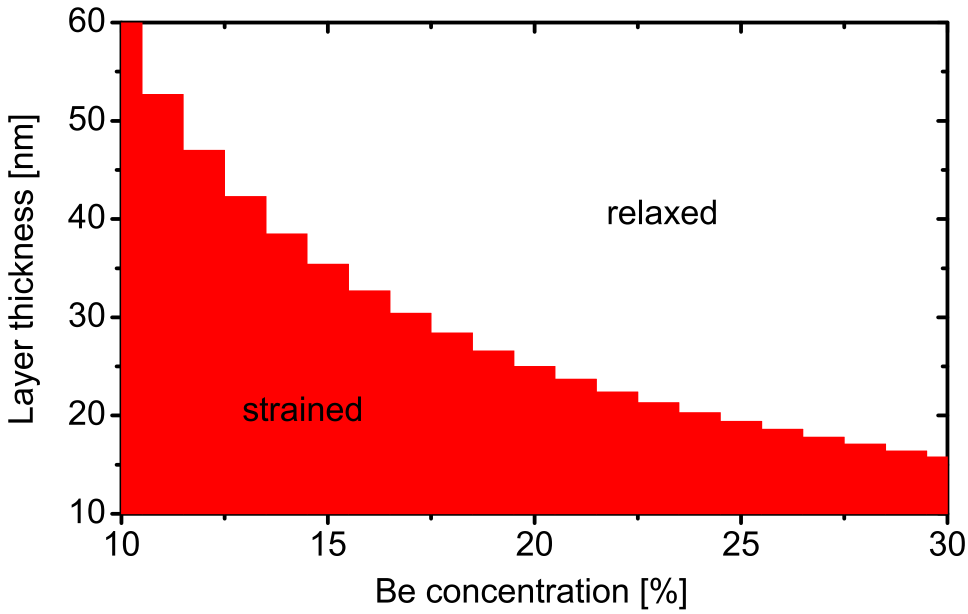

Figure 2.2: *Relaxation diagram of a (Zn,Be)Se epitaxial layer grown on a GaAs substrate.*

Fig. 2.2 presents a relaxation diagram of a (Zn,Be)Se barrier grown strained on a GaAs substrate, and calculated using Eq. 2.1. The barriers that have parameters in the red zone grow strained. Whenever parameters of a barrier exceed the red area the strained layers are most likely to relax creating high defect densities. This must be avoided.

2.2 Growth and characterization of all-II-VI magnetic RTDs

Since all-II-VI magnetic resonant tunneling devices (RTDs) have been suggested (see for example [SY92]), many research groups have been trying to reach the goal. But the progress has been hampered by material issues [GKF$^+$01].

As result of choosing proper material systems, and improving the quality and design of the structures, all-electrical spin manipulation in magnetic all-II-VI RTDswas performed in the experiments described here [SGS$^+$03, GSS$^+$06, GSS$^+$04].

2.2.1 Superlattice approach to screening of the interface field

The samples were prepared and a GaAs buffer was grown as described in section 1.3

The growth start of II-VI semiconductors was initiated by exposing the sample to Zn flux for 40 seconds at the standard growth temperature of 300 ^{0}C. The growth surfaces during the stan-

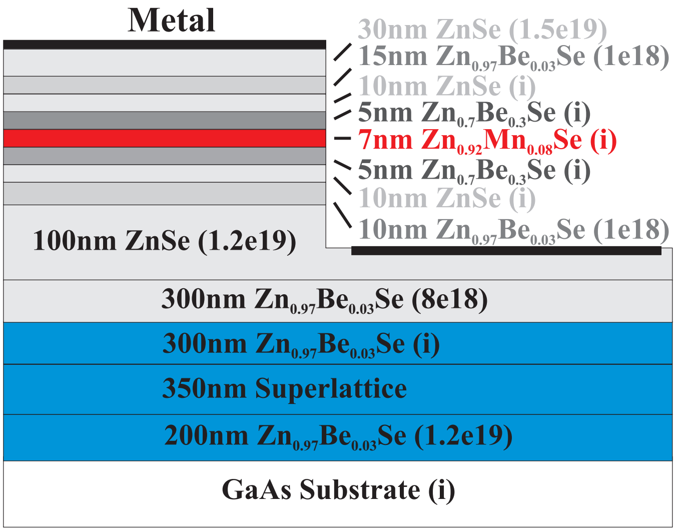

Figure 2.3: *Layer structure of the reference magnetic RTD featuring an interface screening buffer with superlattice.*

dard MBE growth show clear (2x1) RHEED patterns, indicating a very good crystalline quality.

As shown in Section 1.3, GaAs/ZnSe heterovalent interface has a strong effect on transport structures [SHG$^+$99]. The interface creates significant charge depletion in the near interface region of the epilayers. A more detailed description of the depletion on transport structures can be found in [Leh05].

To avoid the negative influence of the interface charge depletion on the transport structures, a screening buffer that consist of a highly doped (Zn,Be)Se layer containing 3% Be was developed and applied to screen the interface fields. This was followed by a five-periods strain-balanced ZnSe/$Zn_{0.9}Be_{0.1}Se$ superlattice. The superlattice prevents charge from the bottom layer from penetrating to the screened region and improves crystalline quality. The buffer was ended by an undoped (Zn,Be)Se layer containing 3% Be. The layer prepares a reliable surface for growth of high-quality transport devices.

The superlattice presents a barrier for electrons of about 138 meV. The thicknesses of the ZnSe layer (50nm) and the (Zn,Be)Se layer containing 10% Be (20nm) were designed to prevent formation of minibands in the short period superlattice, which would drastically reduce the barrier height.

A surface prepared in such a way is screened from the heterointerface effects and leads to an improved reproducibility of the transport structures, as is demonstrated in Section 2.3.

2.2.2 Big and Nano RTD structure processing

On top of the buffer (see Fig. 2.3) a magnetic RTD is formed. At first a 300 nm (Zn,Be)Se layer containing 3$\%$ Be doped to a concentration of $n = 8 \times 10^{18}$ cm^{-3} was grown, then the 100 nm ZnSe back side contact layer was deposited and doped to $n = 1 \times 10^{19}$ cm^{-3}.

In order to achieve a lower Fermi level penetration into the conduction band and prevent a charge accumulation in the injector and the collector a moderately doped $n = 1 \times 10^{18}$ cm^{-3} 10 nm (Zn,Be)Se layer containing 3$\%$ Be barrier and a 10 nm undoped ZnSe layer are grown.

The active part of the RTD was created by sandwiching a 7 nm quantum well of a (Zn,Mn)Se layer containing 8$\%$ Mn between strained barriers of a (Zn,Be)Se layer containing 30$\%$ Be. For symmetry reasons, the collector structure was repeated in reverse on the top injector side.

A 30 nm highly doped $n = 1 \times 10^{19}$ cm^{-3} ZnSe layer serves as a top-side contact. In-situ metallization of the sample ensures high quality and low resistance of the top contact.

After removing the sample from the growth chamber, negative optical lithography was used to define the mesa structure for large-area samples. Cl_2-based chemically assisted ion beam etching (CAIBE) was used to etch the mesa structure down to the highly doped ZnSe layer, on which ohmic contacts can be defined by ex-situ metallization (creating good ex-situ contacts on the bottom (Zn,Be)Se layer proved to be impossible).

A ring-pattern for the bottom contact was then defined around each mesa, again using optical lithography. Subsequently, Ti/Au was evaporated resulting, after lift-off, in ring-shaped bottom contacts, ensuring a homogeneous current distribution in the mesa. The samples were then bonded and investigated in a ^4He bath cryostat.

Fig. 2.4 illustrates the resulting pillar on the semiconductor surface. The top contact is evaporated in-situ an the larger back contact is an ex-situ contact. The electrons are moving from the top contact to the bottom one. The double-barrier quantum well structure of the RTD is located inside of the pillar and perpendicular to the growth direction.

Scaling down the RTDs does not necessarily leave their transport properties unaffected. It is well established that for semiconductors such as GaAs or ZnSe, surface depletion can be in the range of several hundred nm, which has to be taken into account when trying to fabricate RTDs of comparable dimensions.

Since the distance between the top and the bottom contacts is defined by the layer layout during epitaxial growth, scaling down the structure increases the height to width ratio. This fact further complicates the matter.

The etching process for the definition of the mesa has to be carefully chosen in order to achieve reliable results. Using several optimization steps, RTD structures with lateral dimensions under

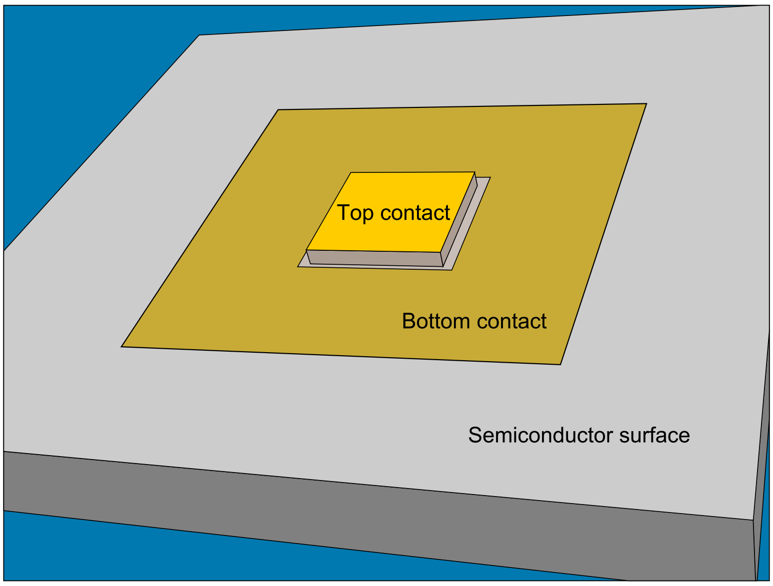

Figure 2.4: *Sketch drawing of the final RTD pillar with the back contact.*

800 nm were successfully fabricated [MSaFL+04].

In the first lithography step, electron beam lithography on a negative resist was used to define the mesa. After development, etching was done using a similar Cl_2-based CAIBE process as for the large-area samples. After the dry etching step, a short (3 s) wet etching step using a mixture of H_2SO_4 and Cr_2O_3 was introduced in order to remove a few nanometers of the semiconductor surface.

Subsequently, a polyimide layer was deposited in order to achieve an insulating sample surface. On top of this layer, a positive-contrast electron beam resist was deposited. Using 30 kV electron beam lithography again, two windows were opened in the resist and subsequently transferred into the polyimide. Optical lithography and lift-off were used to deposit bond pads and leads through the open windows in the polyimide.

Another technique which is also routinely used is the fabrication of metallic air bridges to the mesa.

2.2.3 Contacting RTD devices

It is established that the serial resistance modifies I-V characteristics of a real device [MLSE94, LMS+94]. Therefore, it is important to decrease the parasitic serial resistance. This resistance can be introduced by wires the measurement circuit is made of, by the structure of the device, and frequently, by contacts between the semiconducting device and measurement leads. The serial resistance is the product of multiplying the sheet resistance of the interface by the surface

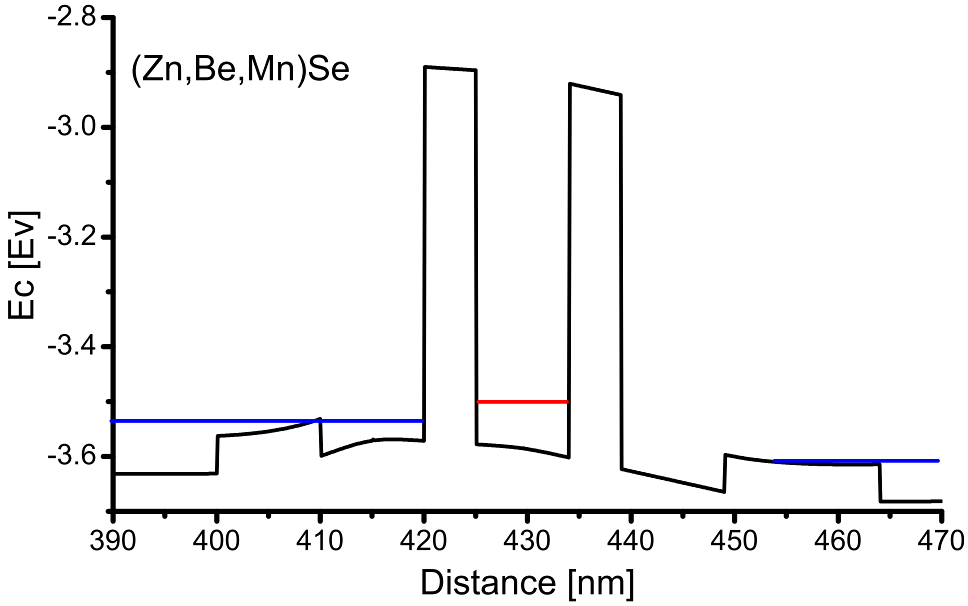

Figure 2.5: *Conduction band profile of a (Zn,Be,Mn)Se RTD out of resonance conditions.*

of the contact. Therefore, interface resistance must be decreased and the surface of the contacts increased.

In presented devices, the top metal contact is made by an in-situ growth of 10 nm Al to achieve low contact resistance, 10 nm Ti as a diffusion barrier, and 30 nm Au to avoid oxidation. This procedure reliably yields a contact resistivity of the order of 10^{-3} Ω cm^2. Since the bottom contact can only be fabricated after processing, it must rely on an ex-situ technique where the contact resistivity is typically 1–3 orders of magnitude higher. Its resistance is kept reasonably low by a combination of the incorporation of a highly n doped 100 nm ZnSe contact layer in the heterostructure and the use of a relatively large (500x500 μm^2) Ti-Au contact pad.

2.2.4 Current-voltage characteristic of a RTD

The samples were measured in a ^{4}He bath cryostat equipped with a 6 T superconducting magnet. Standard low-noise electrical characterization techniques were applied to investigate I-V characteristics of the devices. To prevent the measurement circuit from going into oscillations in the region of the negative differential resistance extra measures were taken. A stabilized voltage source was used to apply bias to the circuit. The circuit was built to have the RTD and a 33 Ω reference resistance in series and a 40 Ω resistor in parallel. Such a configuration prevents bistability of the circuit [LAE+89]. By measuring the voltage drop over the RTD and the reference resistor as the bias voltage is swept, I-V curves of the RTD can be extracted. By comparing I-V curves with different sweep directions, no charging in the devices was found [MLSE94].

The band profile of a magnetic RTD calculated using one-dimensional poisson solver [sim] is shown in Fig. 2.5. Details on material parameters used in the calculation are presented in Section 1.1.2. To give a better understanding of the growth process, it should be pointed out that even though the current is passed from left to right on the band profile, the sample is grown from right to left. This means that the growth sequence is the collector, the double-barrier quantum well, the injector, and so on, as is described in Section 2.2.2. Even though the band structure is typical for resonant tunneling structures, a few important features of the band profile still deserve a more detailed description.

The lowly doped $n = 1 \times 10^{18}$ cm^{-3} (Zn,Be)Se layer containing $\%$ Bespace layer containing 3$\%$ Be before and after the tunneling structure is designed to improve peak-to-valley ratio by creating the right charge distribution in the injector region [WC91]. The undoped ZnSe layer is balancing the band profile and prevents the quantization of the electron states in the injector due to the charge accumulation.

In order to achieve ultimate device performance, the lowly doped spacer layer and the undoped region in the injector must be precisely designed to form the right band profile at the resonance conditions. This means that, ideally, their values need to be adjusted for each value of the barrier thickness, the barrier height, and the quantum well width. The same applies if one changes the composition of the quantum well or the barriers.

By applying voltage to the device, the injector Fermi level is aligned with the level in the quantum well, therefore satisfying resonant tunneling conditions. At the point where the injector Fermi level is aligned with the level in the quantum well additional current connected to quantum mechanical resonant tunneling starts to flow. This leads to a decrease in the device resistance and as a result, the current on the I-V characteristics rises. When the level in the quantum well passes the bottom of the conduction band in the injector, resonant tunneling conditions are not satisfied anymore, and the current returns to a non-resonant tunneling current. Even though the complete quantum-mechanical picture is more complex than this simplified model, it is sufficient to explain fundamentals of the observed effects. A more detailed explanation of the resonant tunneling effect can be found in [Slo05].

I-V characteristics of a typical RTD structure can be seen in Fig. 2.6. The curve shows a resonant peak followed by a negative differential resistance slope. The valley after the main peak is formed as an interplay of the decreasing resonant tunneling current and increasing non-resonant tunneling current through the device. The peak-to-valley ratio is a very common characteristic of RTDs. For the presented device, the peak-to-valley ratio is equal to 3. The second broad feature placed on the distance of about 70 mV from the resonant peak is the LO phonon replica [GTC87].

A comparison of LO phonon energy in ZnSe (31.7 meV) with the difference in voltage positions of the main and phonon assisted resonant peaks yields a leverage factor of around 2 [LB99]. The leverage factor determines which part of the voltage applied to the device drops over the first barrier, and is thus effective in determining the alignment condition for the resonance. Having the leverage factor about 2 is a natural case since only a half of the total voltage drops on the first barrier in the double-barrier structure.

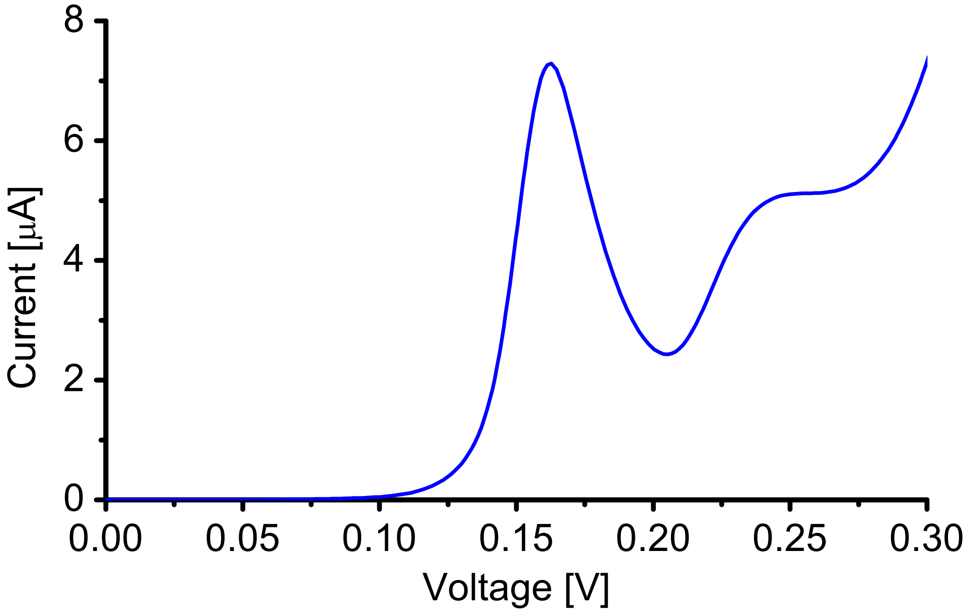

Figure 2.6: *Typical I-V characteristic of a RTD at low temperature.*

Using the leverage factor we can connect the change in the positions of the resonant peaks to the change of the energies of the levels in the quantum well.

2.2.5 Collector and injector band profile

As was already mentioned in Section 2.2.4, the performance of an RTD depends among others on the band profile of the injector region. Wie and Choi [WC91] demonstrated that profiling the injector region is important to improve the peak-to-valley ratio.

For the devices used in these experiments, a step in the band profile followed by an undoped region before the tunneling barriers was used to increase the ratio. The same feature was repeated on the other side of the double-barrier quantum well as is shown in Fig. 2.5.

Since the collector is energetically located below the energy of tunneling electrons, it has no direct influence on the resonant tunneling current. However, by changing the band alignment, it may change the symmetry of the structure and in this way alter its I-V characteristic. Therefore, placing symmetric steps in the band profile on both sides of the barriers improves parameters of the structure.

The electrons accumulated in the injector regionhave a pseudo three-dimensional nature. These accumulated electrons are distributed continuously below the emitter launching energy, down to a certain minimum energy [CW92]. The process leads to an increase in the resonance peak current. For some experiments it is useful to have the resonance at lower energies. One way to achieve this is to increase the conduction band in the emitter.

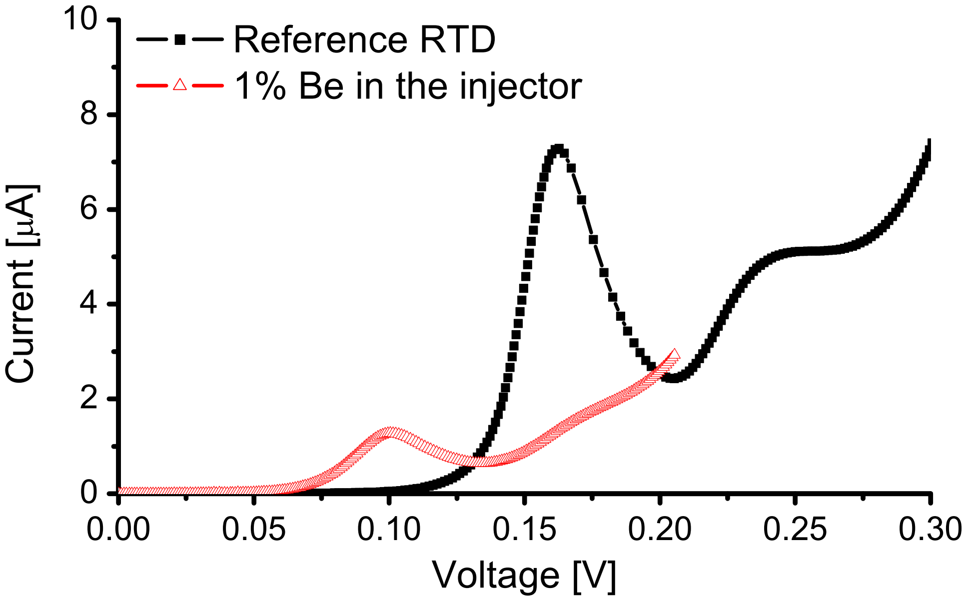

Figure 2.7: *Influence of change in the injector band profile on I-V characteristics of RTDs.*

A change in I-V characteristics of a RTD with incorporation of (Zn,Be)Se in the injector and the collector is shown in Fig. 2.7. The curve of a reference device with ZnSe in the injector and collector is depicted by black squares. The curve depicted by red triangles corresponds to the device with a (Zn,Be)Se layer containing 1% Be in the injector and collector.

The change in the I-V curve is caused by increase in the band gap of the (Zn,Be)Se compound located in the injector. As a result, the band profile shown in Fig. 2.5 changes in such a way that the bottom of the conduction band in the injector is higher in energy relative to the level in the quantum well. This leads to smaller energies needed to satisfy resonance conditions, which results in the resonance peak moving towards lower voltages on the I-V characteristics.

The reduction in intensity of the resonant peak is caused by the change of the carrier distribution in the injector region, as well as by an increase in the electron dwell time [CW92]. As a result, the resonant peak position decreases from 205 mV to 163 mV. The peak-to-valley ratio changes from 3 to 1.96 with the incorporation of 1% Be in the injector. This indicates a deviation from the optimum band profile at resonance conditions due to the change in the injector composition. Besides the dramatic changes to the resonant peak in the I-V characteristic, there is no sizable effect on the background non-resonant current. This shows that the changes in the injector band profile do not affect the active part of the RTD.

In order to incorporate (Zn,Be)Se in the injector, the growth procedure must be altered by introducing a 10 minute growth interruption just after the second resonant tunneling barrier. The pause gives time to decrease the temperature of the Be cell. The interruption is done under Se flux at the standard growth temperature. The same pause is needed before the first barrier to increase the Be cell temperature after introducing Be in the collector.

A similar effect may be achieved by putting magnetic impurities in the injector of a RTD [Slo05]. When an external magnetic field is applied to the structure, (Zn,Mn)Se splits and the lower spin sub-level increases localization of the carriers in the injector. This effect is just opposite to increasing the Be concentration in the injector layer.

2.2.6 Quantum well preparation and analysis

In order to achieve ultimate device performance and excellent interface properties, the quantum well is grown without growth interruption. An interruption after the collector step is needed to heat the Be cell preparing it for the barriers growth. After the injector well another interruption is needed to cool the Be cell down.

For the resonant tunneling to occur, resonant levels in the quantum well must be available. A correct design of the quantum well is needed to achieve the right energy position of the levels.

If the width of the quantum well is too small, the voltage needed to reach the first level in the quantum well is too high. This leads to a formation of strong 2D states in the injector, which might interfere with the investigated effects or even suppress them.

On the other hand, if the width of the quantum well is too big, then the levels in the quantum well merge, leading to an absence of resonant tunneling. The latter situation may be seen as two tunnel barriers in series.

To accurately calculate the positions of the levels in the quantum well, it is essential to take into account that the wave function of the particle on the level is coupled to the outer leads and, therefore, significantly differs from the one in the isolated quantum well.

Fig. 2.8 illustrates the influence of the width of the quantum well on the I-V characteristics of the RTDs. The curve of the device with a 6 nm wide quantum well is depicted by black squares. The resonant peak is at 162 mV, and the peak-to-valley ratio is about 3. The curve depicted by blue triangles corresponds to the device with a 7 nm wide quantum well. The resonant peak is at 180 mV, and the peak-to-valley ratio is about 2.

The fact that the resonant peak of a RTD with a smaller width of the quantum well is placed at higher energies can be explained by taking into account that the levels in the quantum well are moving to higher energies when the width of the quantum well is decreased. Since the resonant level in the quantum well is at a higher energy, a higher voltage must be applied to the device in order to align the Fermi level in the injector with the level in the quantum well.

At the same time, the non-resonant current increases when the total width of the tunneling device is decreased. It should be considered that an electron tunneling non resonantly must tunnel through a potential barrier of the total width of the RTD. Therefore, as the width of the RTD decreases, the non-resonant tunneling probability increases.

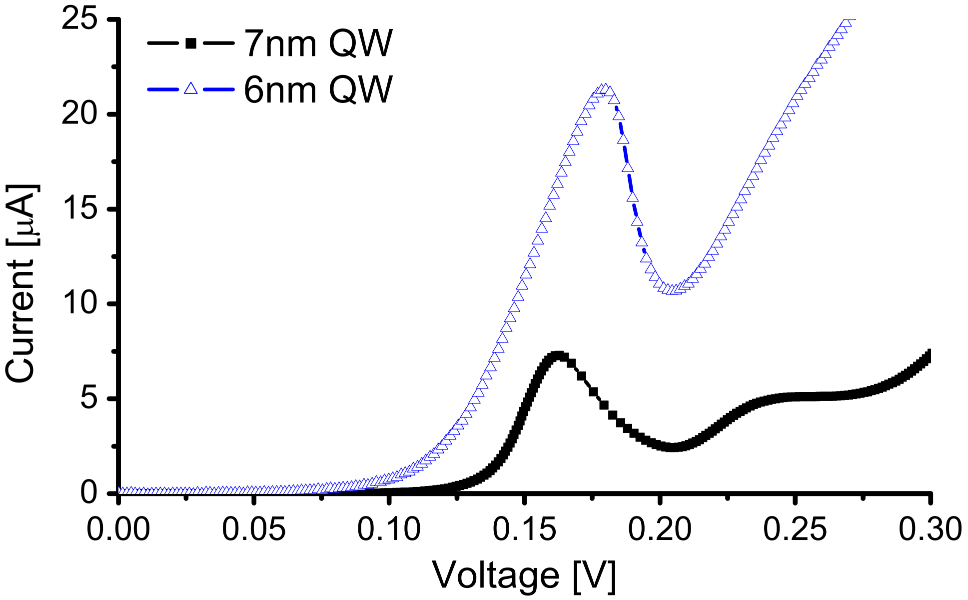

Figure 2.8: *I-V characteristics of two RTDs with the different width of the quantum well.*

The change in the shape of the resonant peak for the two devices is caused by a change in the serial resistance. In fact, not the serial resistance but the ratio of the peak resistance to the serial resistance influences the shape of the resonance. Hence, as the resonant peak resistance changes, its shape changes as well.

2.2.7 Strain in the barriers and the quantum well

In Section 2.1, the critical thickness for a single (Zn,Be)Se tunnel burrier was discussed. In the case of a double-barrier tunneling structure, the strain accumulates, implying that the critical thickness for the sum of both barriers will remain similar to the thickness of a single barrier of the total width. Hence, two barriers of 18nm total width with 30% Be in the lattice should produce relaxation, as is shown in Fig. 2.2.

Since the quantum well is made of (Zn,Mn)Se, and has a strain direction opposite to (Zn,Be)Se relative to the GaAs substrate, the strain in the quantum well compensates for part of the strain in the barriers and in this way prevents the lattice relaxation. Apart from the quantum well, injector and collector regions are also important to improve strain distribution in the device.

A HRXRD $\omega/2\theta$ scan of a RTD with a (Zn,Mn)Se layer containing 8% Mn in the quantum well and a (Zn,Be)Se layer containing 30% Be in the barriers taken with a (004) reflex is shown in Fig. 2.9. The measurements are presented by a blue, solid curve. The red, dashed curve represents a dynamic simulation of the device. The most intense peak corresponds to the GaAs substrate. The sequence of the peaks on the right from 5000 relative arcseconds is formed by interference on the interfaces of (Zn,Be)Se barriers. The simulation is offset in intensity for

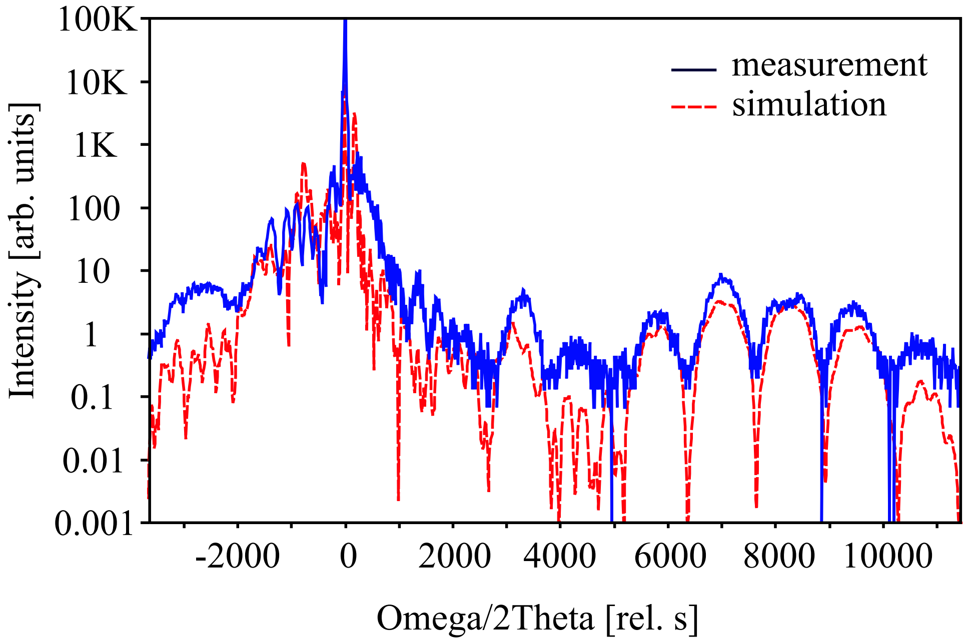

Figure 2.9: *$\omega/2\theta$ scan of a RTD with 8% Mn in the quantum well and 30% Be in the barriers taken with a (004) reflex (blue) and dynamic simulation of the layer (red).*

clarity.

As can easily be observed, the simulation agrees well with the measurement. The lattice mismatch of 0.05 Å extracted using Bragg's law from the 2.25 degree difference in the peaks positions agrees well with the lattice mismatch between a fully strained (Zn,Be)Se layer containing 32.5% Be and a GaAs(100) substrate. The value is consistent with the calibration of the MBE system.

Based on this, the conclusion was drawn that the layers are grown fully strained, with a lateral lattice constant of the GaAs substrate, and that a relaxation, which might occur at about 135 Å [PJJ$^+$98] for a single (Zn,Be)Se layer containing 32.5% Be is not observed.

The presence of multiple thickness fringes on the HRXRD scan indicates a high quality of the layers and interfaces. The partial mismatch between the measurement and the simulation curves can be explained by errors in the simulation of the buffer layers, which are not essential for the analysis.

An increase in Be concentration in the barriers means that, during the growth, the Be cell has a higher temperature at that point. Since the Be cell is operated at high temperatures, the thermal radiation of the cell may heat the epitaxial surface, thus changing the growth conditions. This fact is essential for the samples containing a high Be concentration.

Hence, a proper degassing of the Be cell shutter before the sample growth start is a must. Because the cell is heated to maximum temperatures during growth of the most crucial part of

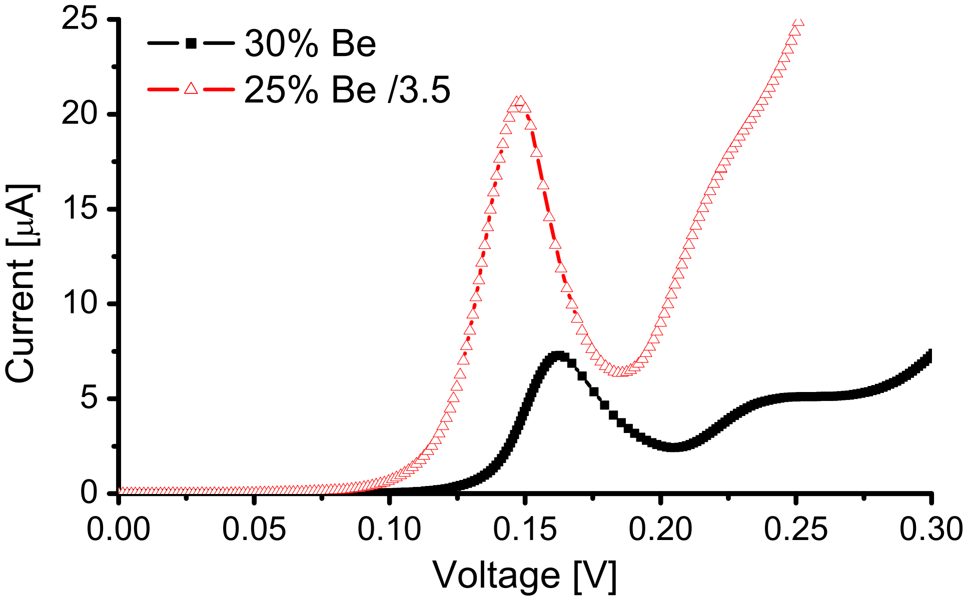

Figure 2.10: *Change in I-V characteristics of RTDs with different Be content in the barriers.*

the device, any contaminations originating from the Be shutter would alter performance of the RTD.

The influence of the barrier height on I-V characteristics of two RTDs is shown in Fig. 2.10. The curve depicted by black squares corresponds to the I-V characteristics of a RTD with (Zn,Be)Se layer containing 30% Be as a barrier material. The resonant peak of the curve is placed at 162 mV and the peak-to-valley ratio is 3.0. The I-V characteristics of the device with the (Zn,Be)Se layer containing 25% Be as a barrier material is depicted by red triangles. The resonant peak in this case moves to the value of 148 mV and the peak-to-valley ratio increases to 3.2. The current of the RTD with (Zn,Be)Se layer containing 25% Be in the barriers is divided by 3.5 in order to have a comfortable visual comparison of the curves.

Adding Be to the (Zn,Be)Se barrier material leads to a change in the height of the barriers of the RTDs. This decreases the coupling of the carriers in the quantum well to the outer leads, increasing the confinement of the QW at the same time. As confinement of the quantum well increases, the levels in the quantum well increase their energy positions. This increases the voltage needed to satisfy resonance conditions, resulting in a shift of the resonant peak on the I-V characteristics to higher voltages.

The non-resonant tunneling current is decreasing due to an effective increase of the total barrier height. The resonant current decreases since it is a product of the resonant and non-resonant tunneling currents. The shape of the resonant peak is modified by the ratio of the RTD resistance and the serial resistance.

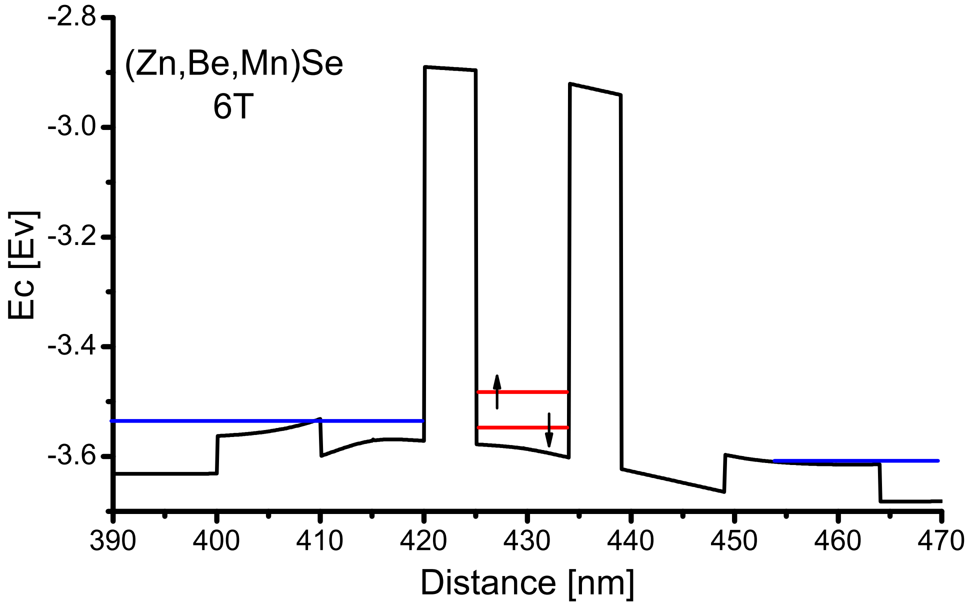

Figure 2.11: *Calculated conduction band profile of a (Zn,Be,Mn)Se RTD at small applied bias. The energy is measured relative to the Fermi level.*

2.3 Magneto-transport investigations of all-II-VI magnetic RTDs

2.3.1 Magnetic RTD with magnetic impurities in the Quantum Well

Without the external magnetic field applied all-II-VI magnetic RTDs behave as a non-magnetic devices, implying that all physical phenomena can be explained by the standard theory developed for the non-magnetic case. Nevertheless, as an external magnetic field is applied the situation changes. The field leads to the giant Zeeman splitting in the DMS layer, as described in section 1.1.3.

Fig. 2.11 shows the conduction band profile of an all-II-VI magnetic RTD with an external magnetic field applied. The profile is calculated using a one-dimensional poisson solver [sim]. Due to the action of the external magnetic field, each level in the DMS quantum well splits into two sublevels, which are depicted by red lines. The sublevels are spin-polarized; that means that the carriers with only one spin orientation can be sustained on a sublevel.

The sublevels for different spin orientations are shown in Fig. 2.11 by arrows. The sublevel with the arrow pointing up can contain only spin-up carriers, while the sublevel with the arrow pointing down contains only carriers with spin-down orientation.

The splitting between the sublevels depends strongly on the external magnetic field and follows the Brillouin function as the magnetic field is increased (see Section 1.1.3). The fact that this magnetic field behavior of the DMS can be distinguished from other magnetic effects simplifies the device characterization.

When a constant magnetic field is applied to the device, the sublevels in the DMS quantum well are split. Applying voltage to the device moves the Fermi level in the injector up in energy relative to the levels in the quantum well. When the Fermi level in the injector is aligned with a sublevel in the quantum well, resonant tunneling current starts to flow. Since the sublevel in the quantum well is spin-polarized, the resonant tunneling current of this defined spin-polarization flows through the device.

The situation is illustrated in Fig. 2.11 where only the spin-down level in the quantum well is aligned with the Fermi level in the injector, and the spin-up level is out of the resonance. This means that the resonance current passing through such a device is spin-down-polarized.

If the external voltage increases further, the spin-down level moves below the bottom of the conduction band in the injector and the resonant current stops to flow through the channel. Further increase in the voltage leads to the alignment of the spin-up sublevel in the quantum well with the Fermi level in the injector. The resonant tunneling conditions are satisfied, and the current of an opposite spin orientation starts to flow though the device.

This indicates that such a device may function as a voltage controlled spin polarizer, since depending on the applied voltage, one or another spin-polarization of the passing current may be selected without changing the direction or mgnitude of an external magnetic field. This is achieved by simply aligning different sublevels in the quantum well with the Fermi level in the injector.

The possibility to control spin-polarization in such a way may be used in the new generation of the devices that will use a spin degree of freedom in addition to the charge of the particles. The field of spintronics has been long anticipating such a device.

Regardless, to have a sizable effect on I-V characteristics of the device, a few conditions have to be met. The splitting of the sublevels in the quantum well has to be bigger than the depth of the Fermi level in the injector. By engineering the band profile in the injector, it is possible to reduce the depth of penetration of the Fermi level, thus improving this relation. Subsequently, the natural broadening of the resonant peak should be smaller than the distance between the sublevels. Since the natural broadening depends on the material properties, the temperature, and the magnetic field, these parameters should be taken into account.

The splitting of the sublevels can be increased by a proper choice of the magnetic material. In this study paramagnetic DMS (Zn,Mn)Se was utilized as the quantum well material. The depth of the Fermi level in the conduction band was controlled by the band profile. At typical operating conditions, the natural broadening is not significant, as is shown on AlGaAs RTDs [TSY85]. From this, it was concluded that there is no fundamental obstacle for the room temperature device operation.

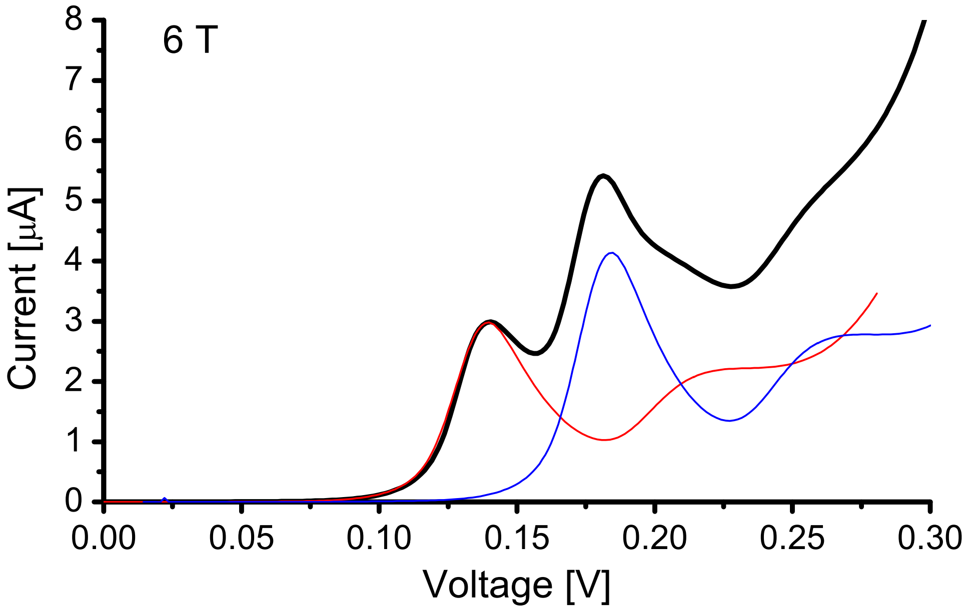

Figure 2.12: *I-V characteristic of a magnetic RTD with an applied magnetic field of 6 T. The lines represent currents flowing through individual spin channels.*

Fig. 2.12 shows I-V characteristics of an all-II-VI magnetic RTD having a (Zn,Mn)Se layer containing 8% Mn in the quantum well at an applied magnetic field of 6 T at 4K superconducting magnet. The black line represents the experimental data. The simulations of the current flowing through individual spin channels are shown in red and blue.

Two distinct peaks are present on the I-V characteristics of the device. The peaks correspond to resonances on two spin degenerate sublevels. As illustrated in Fig 2.11 using the band diagram, two separate sublevels come to resonance at different voltages, producing separate peaks on the I-V characteristics. The first resonant peak is placed at 140 mV, and the second one is placed at 181 mV.

From the comparison of the LO phonon energy in ZnSe with the difference in voltage positions of the main and phonon assisted resonant peaks at a zero magnetic field, a leverage factor is obtained, as described in Section 2.2.4.

Since the magnetic field dependence of the giant Zeeman splitting is known (see Section 1.1.3) the values of the energy splitting of the sublevels in the quantum well could be compared with the expected giant Zeeman splitting at different magnetic fields, and an excellent agreement between them was found [SGS^{+}03].

To simulate the magnetic field behavior of the resonances, a model based on the giant Zeeman splitting of the resonant levels in the DMS (Zn,Mn)Se quantum well was developed. The conductances of the individual tunneling sublevels were assumed to remain identical as they split apart.

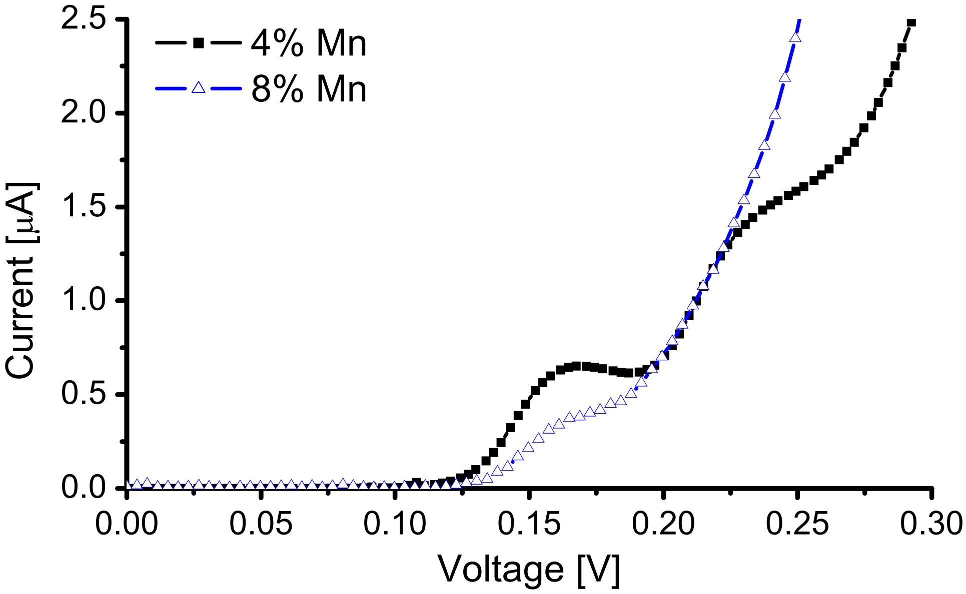

Figure 2.13: *Change in I-V characteristics of RTDs with magnetic impurities in the injector.*

A zero magnetic field I-V curve was used as a starting point. Then, the series contact resistance of the RTD was extracted from the measured I-V curve at zero magnetic field [MLSE94]. In the next step, the curves corresponding to different sublevels were translated into energy to reproduce their splitting.

For demonstration purposes, the separate curves of the current flowing through individual spin channels with added serial resistance are depicted in Fig. 2.12. The peak current intensities of the resonant peaks are different, due to the fact that the sublevels have the same conductance, and, therefore, the current flowing through the sublevel at lover voltages is smaller, following Ohm's law.

Finally, conductivity contributions of both the spin-up and the spin-down curves were added and the series resistance reinserted to yield a modeled I-V curve at a given magnetic field.

By comparing this I-V curve with the actual experimental curve at 6 T, an optimal value of the serial resistance was determined. Using this value of the series resistance for all modeled curves, and fitting the modeled curves at each field to the experimental ones, the voltage splitting of the sublevels in the quantum well as a function of an applied magnetic field was extracted. Then using the leverage factor, the voltage splitting was translated to the energy aplitting, and the values of the actual splitting were compared with expected giant Zeeman splitting [GSS$^+$04].

2.3.2 Magnetic RTD with magnetic impurities in the Injector, Collector

Fig. 2.13 shows the change in the I-V characteristic of a resonant tunneling diode with incorporation of a (Zn,Mn)Se layer containing 4% Mn (black squares) and a (Zn,Mn)Se layer containing 8% Mn (blue triangles) in the injector. For both samples the resonant peaks are located at about 164 mV. For the sample containing 4% Mn in the injector, the peak-to-valley ratio is about 1.05.

Intuitively, the presented figure would be expected to be similar to Fig. 2.7, where (Zn,Be)Se was used to alter the band profile of the injector. Even though, in contrast to section 2.2.5 (Zn,Mn)Se was used to change the band profile.

Changing the Mn concentration from 4% to 8% in the (Zn,Mn)Se increases the band gap of the compound by about 24 meV (see Fig. 1.5). The value can be well compared to the change in the (Zn,Be)Se band gap of about 23 meV by incorporating 1% Be (see Eq. 1.2). From this, the value of the shift in the resonant peak would be expected to be similar to that of (Zn,Be)Se which is 42 mV.

While the resonant peaks seem not to change their position with increasing Mn content in the injector, this is a false impression. The change can be deducted from comparison of nonresonant currents. These currents are increasing exponentially in both figures, but in Fig. 2.7, nonresonant currents for both of the curves follow the same slope, whereas in Fig. 2.13 they have different slopes for the curves with different Mn contents.

This leads to the conclusion that by adding Mn in the injector, the chemical nature of the compound is altered and an additional band offset is introduced. Indeed, shifting the curves in order to match their nonresonant exponential slopes yields the expected shift of about 40 mV.

The magnetic field dependence of the I-V characteristics will no doubt be different depending on the position of magnetic impurities. Having magnetic material in the injector (collector) and in the quantum well at the same time opens new possibilities for investigating the spin transport in resonant tunneling structures.

Fig. 2.14 presents a magnetic field evolution of the resonant peaks for the device with a (Zn,Mn)Se layer containing 4% Mn in the injector and a (Zn,Mn)Se layer containing 8% Mn in the quantum well. Positive voltages on the I-V correspond to the DMS layer located in the injector; the resonant peak is located at about 164 mV. Negative voltages present a situation when DMS is located in the collector. The resonant peak in this case is located at -350 mV and has a peak-to-valley ratio of 1.61.

Comparing the shapes and positions of the resonant peaks at positive and negative voltages combined with the magnetic field evolution of the peaks it was concluded that the peak, at negative voltages, most likely corresponds to resonant tunneling through the second resonance level in the quantum well.

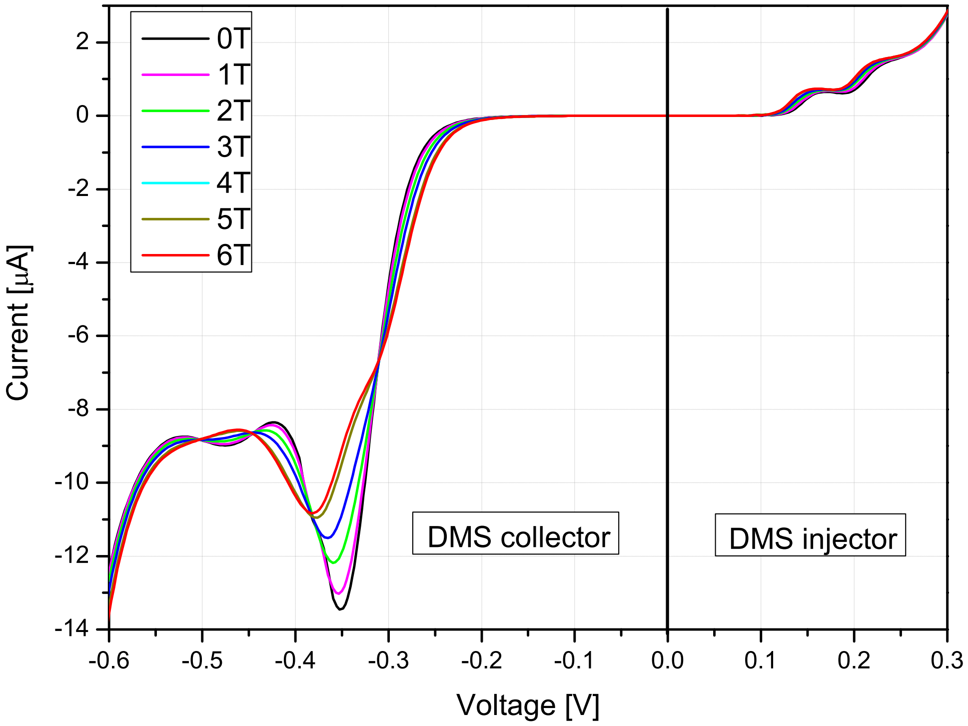

Figure 2.14: *Magnetic field evolution of resonant peaks for the sample having a (Zn,Mn)Se layer containing 4% Mn in the injector (positive voltages) and the collector (negative voltages). A (Zn,Mn)Se layer containing 8% Mn located in the quantum well.*

When the current direction is such that the magnetic impurities are in the collector, the I-V characteristics of a magnetic RTD can hardly be influenced by the giant Zeeman splitting in the DMS. In this case, the magnetic field dependence of the I-V characteristic follows the dependence described in Section 2.3.1. The magnetic field dependence of the resonant peak located at negative voltages in Fig. 2.14 proves the above statement. Hence, the I-V characteristics of a RTD can not be directly influenced by the collector band profile, since it is well below the energy of the transmitted carriers.

The situation changes quite a bit when the current is passed in the opposite direction. The injector appears to be spin-polarized at even small magnetic fields, and the I-V characteristics of the RTD are strongly affected.

To describe the effect of a spin-polarized current on the I-V characteristics of a magnetic RTD, resonant tunneling must be examined more closely. Resonant tunneling as any tunneling process is described by tunneling transmission probabilities for individual sublevels. The current is then defined as the product of the multiplication of available carriers on the transmission probability. Since the transmission probability of each of the sublevels in the quantum well is constant, the carrier spin-polarization in the injector is crucial for determining currents flowing through the channels.

The DMS (Zn,Mn)Se layer containing 4% Mn in the injector creates 100% carrier spin-polarization even at small applied magnetic fields. Therefore, all the current is expected to flow through only one of the spin channels. However, since the total carrier concentration in the injector is not changed, the total current at this resonance would not be changed either.

With rising magnetic field, the giant Zeeman splitting separates the sublevels in the quantum well, leading to a change in energy of corresponding resonant peaks. Finally, the resonant peak is the I-V characteristics of a magnetic RTD with magnetic impurities in the injector would move down, or up, in energy depending on the direction of the carrier spin-polarization. Again, the magnetic field dependence of the resonance peak located at positive voltages on the I-V characteristics of the device presented in Fig. 2.14 precisely follows the description.

An even better understanding of the influence of the spin-polarized current on the I-V characteristics of magnetic RTDs can give an introduction a smaller amount of Mn in the injector. For example having a (Zn,Mn)Se layer containing 0.5% Mn in the injector introduces no big change to the injector band profile when the magnetic field is applied. At the same time, by increasing the spin-polarization of the carriers in the injector, it strongly modifies the I-V characteristics of the device. Investigations of this phenomenon are in progress.

Following the same logic, it may be concluded that the spin-polarized transport through a nonmagnetic RTD does not lead to strong changes in the I-V characteristics of the device. The statement is easy to confirm by taking into account that the total carrier concentration of the carriers in the injector does not change as carrier spin orientation changes. Since spin-polarized sublevels in the quantum well of a nonmagnetic RTD are located at the same energy, even when the current flows through one of the spin channels, the total I-V characteristics of the device is not affected.

The fact that barely any spin transport is observed in nonmagnetic RTDs at regular conditions can now be explained. At very high magnetic fields, however, the regular Zeeman splitting splits spin-polarized sublevels even in a nonmagnetic RTD.

From the growth point of view, introducing Mn in the injector means that an extra growth interruption of 2 minutes has to be introduced between the growth of the second barrier and the injector. The growth interruption gives time for the Mn cell to stabilize its temperature. The interuption is done under standard growth temperature and constant Se flux.

2.3.3 Magnetic RTD with magnetic impurities in the Barriers

Fig. 2.15 presents I-V characteristics of an RTD having a (Zn,Be,Mn)Se layer containing 6% Mn and 30% Be in the barriers and a nonmagnetic quantum well. I-V characteristics of the device without applied magnetic field are shown by the black squares. The resonant tunneling peak is located at 70 mV and the peak-to-valley ratio is 2.4. I-V characteristics of the RTD with an applied magnetic field of 13 T are shown by the red triangles. In this case the voltage of the resonant tunneling peak moves to 73 mV and the peak-to-valley ratio increases to 2.55.

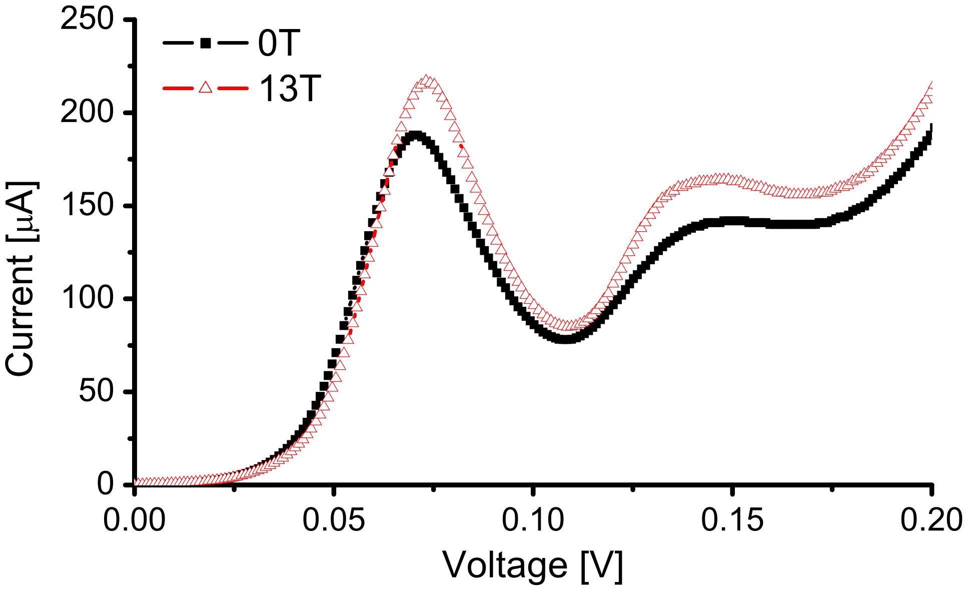

Figure 2.15: *Magnetic field induced change in the I-V characteristics of a RTD having a (Zn,Be,Mn)Se layer with 6% Mn and 30% Be in the barriers and a nonmagnetic quantum well.*

The presence of magnetic material in the barriers means that the giant Zeeman splitting leads to the splitting of the bottom of the conduction band for different spin orientations when an external magnetic field is applied. This means that for one spin orientation, the height of the tunneling barrier increases, whereas for the other one it decreases. Therefore, the 13 T I-V characteristics presented in Fig. 2.15 is the result of a superposition of both effects.

The change in the height of the tunnel barriers for individual spin channels follows the dependence described in section 2.2.7. The increase in the tunneling current for one of the spin channels is stronger than the decrease for the other one, because it follows an exponential dependence with the barriers' height. This results in an enlargement of the overall current. However, the superposition of the proportional increase and decrease in the height of the barriers decreases the effect on the total current.

On the quantum well, magnetic material in the barriers has a negligible effect, but by changing the height of the barriers, it changes the confinement for the separate spin species and, therefore, leads to a splitting of the spin sublevels in the quantum well. However, due to the small value of the giant Zeeman splitting of the conduction band (about 11 meV for a (Zn,Mn)Se layer containing 6% Mn at 13 T) as compared to the large height of the tunneling barriers (about 400 meV for a (Zn,Be)Se layer containing 30% Be), the splitting of the sublevels in the quantum well is relatively small. This explains why no distinct spin dependant splitting of the resonant tunneling peak is observed in the I-V characteristics.

An increase in the resonant peak current, as well as an increase in the peak-to-valley ratio, is consistent with change in the height of the barriers. In contrast, the shift of the resonant peak to higher voltages is not expected from the change in the barrier height.

Since a high magnetic field is employed to manipulate the magnetic RTD, it has a side effect by inducing a regular Zeeman splitting in whole the structure. Following an analogy with Section 2.2.5, a change in the band profile of the injector leads to a change in the voltage of the resonant tunneling peak and its peak-to-valley ratio. Taking into account that such a behavior is consistent with the effect expected from a decrease of the injector step, it may be concluded that the magnetic field induced change in the I-V characteristics of the RTD with magnetic impurities in the barrier is caused by the interplay of the decrease in the barrier height and the regular Zeeman splitting in the injector.

2.3.4 Double quantum well triple barrier magnetic RTDs

Natural extensions of a double-barrier tunneling system are the two coupled wells or a triple-barrier system. The devices are known as double quantum well triple barrier resonant tunneling diodes (TBRTDs). TBRTDs have attracted much interest due to the rich set of physical phenomena which can be studied and applied to fabricate more flexible devices [Has02]. The presence of a middle barrier places TBRTDs in a complexity between double-barrier RTDs and superlattices consisting of multiple quantum wells.

Numerous detailed studies of the tunneling current through TBRTDs provide insight into the more complex processes of the resonant tunneling in strongly coupled superlattices [DKK85], sequential resonant tunneling through multiquantum well superlattices [CMC86] and an even better understanding of the resonant tunneling process in double-barrier RTDs.

Another way to treat TBRTDs is to look at the carrier transport as tunneling between two coupled quantum wells. The quantum wells are confined in the growth direction and extended in the plane perpendicular to it [Has02]. Additionally, having more than a single quantum well may lead to an increase in temperature stability of the resonant peaks on the I-V characteristics of the device [SBTH88].

In early investigations, it was suggested that charge accumulation in the first well, and thus the overall tunneling characteristic, is controlled by the position of the lowest bound state in the second well, which identifies tunneling transitions that are unique to triple-barrier structures [NIKO86]. Ten years later, the suggestion was confirmed by applying intense pulsed magnetic fields [MBC^{+}96].

Magnetic properties of DMS (Zn,Mn)Se layers were used in this experiment to investigate the TBRTDs and to explore the potential applications of the phenomenon for spin-polarized transport.

Fig. 2.16 presents the calculated local density of states of a TBRTD at 0.2 V applied voltage. Calculations were done using a simulation package [IM] and standard parameters for (Zn,Be)Se semiconducting epilayers. The layer structure of the TBRTDs is similar to double-barrier RTDs, except that the double-barrier structure is replaced by three 5 nm (Zn,Be)Se barriers containing

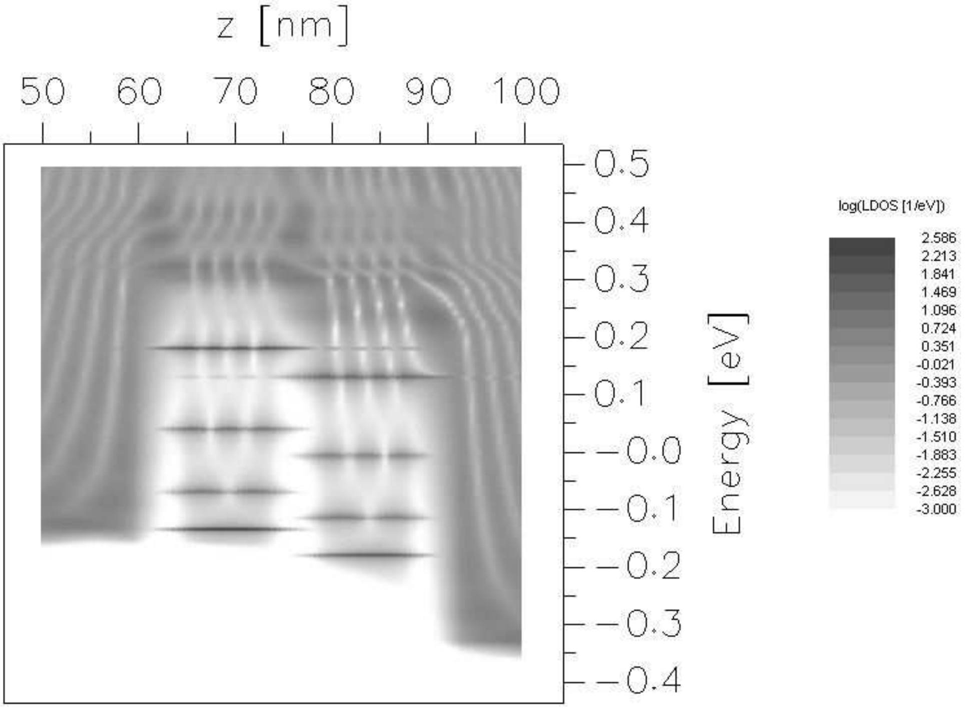

Figure 2.16: *Calculated local density of states of a TBRTD at 0.2 V applied voltage.*

25% Be confining two 7 nm ZnSe quantum wells.

Darker regions on the plot correspond to a higher local density of states in the structure. Resonance levels in the quantum wells may be observed as dark horizontal lines. At the presented voltage, the first resonance level in the first quantum well (left) is very close to the Fermi level in the injector. However, since the first resonance of the second quantum well (right) is located below in energy, the resonant tunneling will not occur.

When applied voltage is increased, the levels move relative to each other and to the Fermi level in the injector. At the point when the first resonant level in the first quantum well aligns with the Fermi level, the carriers start to tunnel through the first barrier and accumulate on the level in the quantum well. This means that the resistance of the first tunnel barrier decreases and most of the voltage drop is distributed between the two following barriers, confining the second quantum well.

At the point when the second resonance level in the second quantum well is aligned with the first resonance level in the first quantum well, the resonant current starts to flow. The situation may be compared with resonant tunneling in a double-barrier quantum well structure, except that the carriers are tunneling to two-dimensional states in the first quantum well first, and then through the double-barrier structure.

When the applied current increases further, the second resonance level in the second quantum well moves below the first resonant level in the first quantum well and the current returns to the

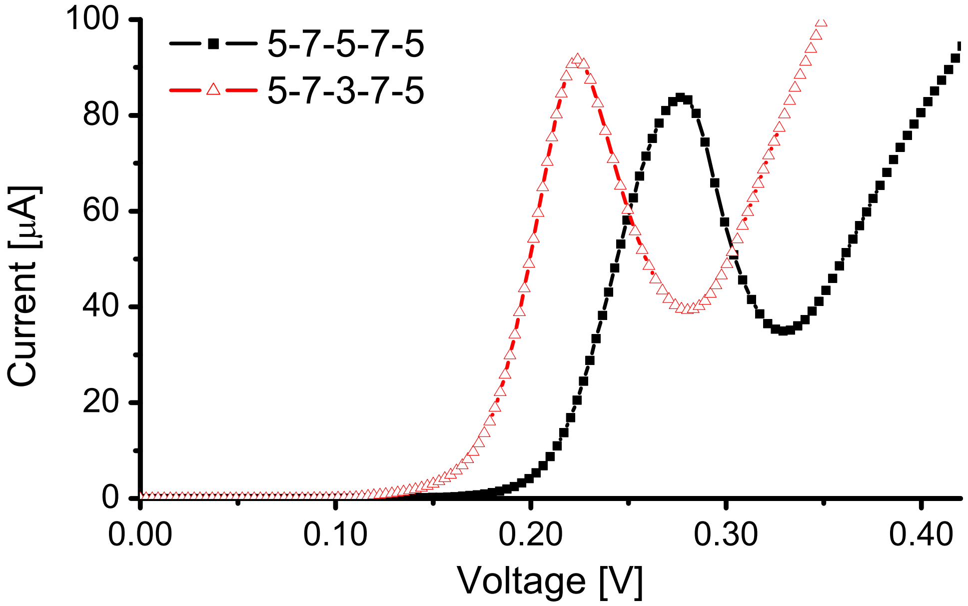

Figure 2.17: *Influence of the middle barrier width on I-V characteristics of a TBRTD.*

nonresonant tunneling current, producing a negative differential resistance.

As was previously mentioned, TBRTDs provide a great flexibility for investigation of variations in the internal structure of the device. Due to this flexibility, basic investigations of the device response were able to be performed without changing the symmetry of the device.

The change in the I-V characteristics of a magnetic TBRTDs, when changing the width of the middle barrier from 5 to 3 nm, is shown in Fig. 2.17. The I-V characteristics of the device with three 5 nm (Zn,Be)Se layers containing 25% Be barriers confining two 7 nm (Zn,Mn)Se wells containing 8% Mn is presented by black squares. The resonant peak is placed at 276 mV, and the peak-to-valley ratio is 2.39. For the TBRTD with the same structure but 3 nm width of the middle barrier (red triangles), the voltage position of the resonant peak moves to 224 mV, and the peak-to-valley ratio decreases to 2.33.

The decrease in the voltage position of the resonant peak is consistent with the increase in the coupling of the electron levels in the quantum wells. This leads to a move of the resonance levels in the individual quantum wells to lower energies and a resulting shift of the resonant peak.

The increase in the background current is also consistent with the increased tunneling probability due to the decrease in total device width. The decrease in the peak-to-valley ratio may be explained by the increase in the nonresonant current as compared to the resonant one.

Another important property of magnetic TBRTDs is the magnetic field induced splitting of spin degenerate sublevels in (Zn,Mn)Se quantum wells.

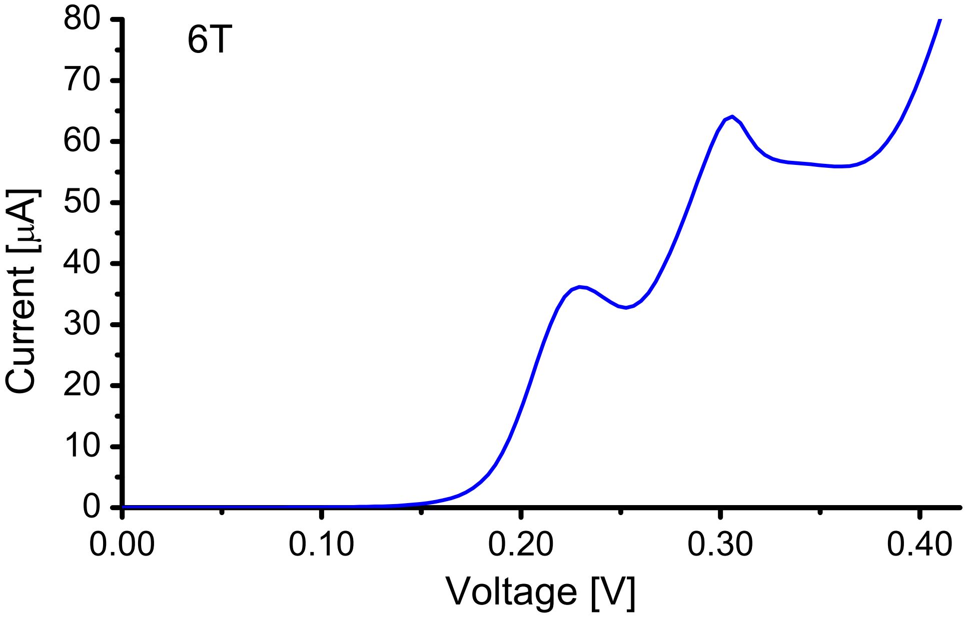

Figure 2.18: *I-V characteristics of a magnetic TBRTD at 6 T.*

I-V characteristics of a TBRTD having three 5 nm (Zn,Be)Se barriers containing 25% Be confining two 7 nm (Zn,Mn)Se wells containing 8% Mn at an external magnetic field of 6 T is shown in Fig. 2.18. As is illustrated, the resonant peak is split into two distinct features located at 229 mV and 305 mV. The splitting of the resonant tunneling peak in the external magnetic field can be attributed to the separation of two spin degenerate channels. The model is described in Section 2.3.1.

The presented figure is similar to Fig. 2.12 but there is a very important difference. It is shown in the absolute values of the resonant peak voltage splitting.

Since both the double-barrier RTD and the TBRTD have a (Zn,Mn)Se layer containing 8% Mn in the quantum well, the value of the giant Zeeman splitting at defined voltage should be the same. However, the value of the resonant peak voltage splitting for the TBRTD is 76 mV, whereas for a double-barrier RTD, it is 41 mV.

As was mentioned previously, there is a leverage factor that connects the change in the voltage position with a change in the energy position of the resonance levels. Comparing positions of the phonon replica on I-V characteristics without a magnetic field, no big change in the leverage factor is found. Therefore, the difference must be related to the property of the TBRTD.

This phenomenon can be explained by remembering that magnetic impurities are present in both of the quantum wells in the TBRTD. This means that as a magnetic field is applied, the levels in the quantum wells split into spin degenerate sublevels. Due to spin selection, the resonance conditions are satisfied only when the sublevels of the same spin orientation are aligned in both quantum wells. Hence, double difference in voltage position is needed, first between the injector and a resonance sublevel in the first quantum well, and then between the sublevel in the first quantum well and a corresponding sublevel in the second quantum well.

Taking into account the difference in the leverage factors for the devices, the fact that the splitting for TBRTD is 1.85 times bigger than that for the double-barrier RTD, is very consistent with the expectation.

From the growth perspective of the double quantum well TBRTDs, it is necessary to mention strain accumulation due to the high lattice mismatch between the triple barrier structure and the rest of the sample. Since the barriers are strained, the strain accumulates with each layer. As a result, it is possible to see slight deviations in the RHEED patterns at the final stages of the third barrier growth. The change in the RHEED patterns is caused by a slight deformation of a few atomic layers just at the growth surface. However, as soon as the injector layer starts, the strain is immediately compensated and the RHEED patterns return to a (1x2) reconstruction. This suggests that it would be difficult to further increase the width of the barriers without decreasing the Be content.

2.3.5 Magnetic RTDs in series

When an external magnetic field is applied to a magnetic RTD, a splitting of spin resolved sublevels in the quantum well leads to a splitting of the resonant peak on the I-V characteristics. As was described previously in Section 2.3.1, changing the external voltage applied to the RTD allows a creation of a spin-polarization of the transmitted current at a constant external magnetic field.

Using the same logic, it is possible to detect the spin-polarization of an incoming current by monitoring the shape of the I-V characteristic of an RTD. When the incoming current is spin-polarized, it changes the carriers' spin-polarization in the injector, and therefore, the ratio in the intensity of the subpeaks on the I-V characteristic, as is described in Section 2.3.2.

The next logical step is to combine the spin selection and spin detection of the resonant tunneling diodes by placing them in series. This means that one of the devices will produce spin-polarization, and the other will detect it.

Lateral approach

To place two devices in series, the same approach that had been used to prove electrical spin injection into a nonmagnetic semiconductor be electrical means can be used [SRG$^+$01]. Both the spin polarizer and the spin detector are placed on a layer of conducting nonmagnetic semiconductor. The configuration seems possible since the RTDs are spin-sensitive independent from the current direction.

To fabricate such a device, there is no need for a special growth procedure since even the same device that was used in vertical geometry can be lithographically processed to hold two pillars with active devices close to each other. Then, by applying voltage between the top contacts of the RTDs and the back side contact placed on the nonmagnetic semiconductor, it is possible to observe spin transport in the construction.

However, there is a very strong demand that for such a structure, the distance between the devices must not exceed the spin-scattering length in the semiconductor. The spin-scattering length in n-type doped ZnSe at low temperatures is about 1.5 μm [SRG$^+$01].

Decreasing lateral dimensions of the devices to such a scale presents bigger technological challenges than it may seem at first. Although, the surface depletion is a very limiting factor (see section 2.2.2), devices of comparable dimensions were produced. Magneto-transport investigations of such structures were performed however, they did not yield conclusive results.

Vertical approach

A different way to combine two RTDs is to grow two devices in series. A contact to the conducting layer between them can be established by etching down the pillar. Then, a back side contact for the bottom device can be prepared. Such an approach simplifies the lithographical steps and decreases the demands on the lateral size of the device.

Growth in such a configuration is not trivial, again, due to strain accumulation in the device. Even the conducting layer between the RTDs partially balances strain accumulated in the barriers. The total strain accumulation is enormous.

A device with the following layout has been grown: The first RTD with a (Zn,Be)Se layer containing 25% Be in the barriers and a (Zn,Mn)Se layer containing 8% Mn in the quantum well is followed by 50 nm of highly doped ZnSe. Then, the second RTD with the same parameters is followed by a highly doped contact layer and in-situ top contact. During the growth of the second RTD, a slight deviation in the RHEED patterns has been observed. Further observations of RHEED patterns show no lattice relaxation, and post-growth characterization using HRXRD shows a very good crystalline quality as well.

Since the distance between the devices must be maintained as small as possible, it is hard to fabricate a reliable measurement contact to the layer between the devices. The point is that the contact must hit the conducting layer and must not influence the I-V characteristic of the RTD below it, since such an influence would produce unwanted side effects.

Overall, placing two RTDs in series for spin detection proves to be a difficult task. Due to complex voltage distribution in the nonlinear devices placed in series and complex current distribution in the lithographical structures, the spin detection in RTDs in series remains yet to be demonstrated. However, measurements on the vertical devices seem more promising.

2.3.6 Gated magnetic RTDs

Since RTDs contain a two-dimensional system confined between two tunneling barriers, it is an attractive perspective to decrease the lateral size of an RTD. This increases the confinement of the carriers in the plane of the quantum well as well. It transforms a two-dimensional transport system into a zero-dimensional one. The zero-dimensional systems are often called artificial atoms or artificial quantum dots. The system attracted enormous attention in the last decade because of its potential application in quantum computing.

It is possible to produce devices of the necessary size lithographically, but since the side surface of the pillar, relative to its dimensions, is increasing, electrical properties of the device are strongly influenced by the depletion, as was described before. The surface depletion is not always easy to control with the required precision on such dimensions. Therefore, another approach must be used.

Placing electric gates on both sides, or even better, around the pillar, produces the desired effect. By applying a voltage to the gates, it is possible to control the size of the depletion region and therefore confinement of the carriers in a lateral direction.

Again, a lithographical challenge strikes in that it is complicated to place non-leaking gates sufficiently close to the active layer. As a solution to this, an extra layer with decreased carrier concentration in the collector region seems to be the answer. The gate can be created as a Schottky barrier between the gate metal and the RTD semiconductor. It is a very reasonable approach as it places the gate very close to the device and decreases the amount of interfaces.

These structures have also been grown and are currently under investigation.

2.4 Resonant tunneling through quantum dots in magnetic media

2.4.1 Growth of self-organized semimagnetic structures

Instabilities in the semiconductor heterostructure growth can be exploited for the self-organized formation of nanostructures allowing for carrier confinement in all three spatial dimensions. Using confinement effects, new device concepts with additional degrees of design freedom become feasible. Restrictions due to material properties are shifted or lifted. In particular, semiconductor nanostructures have created numerous concepts in nano- and optoelectronics, while still containing a large potential for further innovation. Multiple devices utilizing self-organized nanostructures are already on the market or close to mass production.

The ultimate limit of lowdimensional structures is, however, the quantum dot, in which the carriers are confined in all three dimensions. In early days numerous attempts were made to investigate the possibility of a lateral patterning of layered systems in order to achieve such confinement. Regrettably, it was found that the semiconductor structures of the required sizes were challenging to fabricate with conventional techniques, since the sizes must be constrained in the order of 10 nm.

On the other hand, ways to fabricate small structures in large numbers and without interface defects have been known for a long time. However, at first, spontaneous undulations and a “roughening” of the growing surface have been perceived as a problem in semiconductor epitaxy degrading the interfaces between different materials. Around 1990, it became gradually accepted that such a “rough” surface might well be considered as a surface containing nanostructures. It was discovered that the undulations were formed as a way to reduce the stress in the growing film. Obviously, a rough surface is rather far from the conventional idea of a surface of quantum dots of certain predictable properties. In many cases, the size distribution of self-organized islands is fairly broad, and due to the fact that the island nucleation process is statistical in nature, lateral ordering is typically absent.

The most prominent self-organized growth method is Stranski-Krastanow growth, which leads to the formation of nanoscale islands on top of a two-dimensional wetting layer. This growth method occurs for almost any semiconductor heterostructure with a certain lattice mismatch between the constituent materials.

The strain distribution in a growing sample is one of the main driving forces that lead to the formation of nanostructures. Particularities of the strain distribution can lead to the formation of very regular ensembles of nanostructures. The ensembles may have a narrow size distribution, and, in some cases, are lined up in wires or even lattices.

Depending on the surface energies and the lattice mismatch, a few growth modes of self-assembled structures are possible. In lattice-matched systems, island formation is driven by high interface energy γ_{12} and high epilayer surface energy σ_2. In the case of $\sigma_2 + \gamma_{12} < \sigma_1$, self-organized islands are formed. Change in the quantity of $\sigma_2 + \gamma_{12}$ defines the transition fromFrank-van der Merwe to Volmer-Weber growth. The point may be better illustrated by Fig. 2.19 where Frank-van der Merwe, Volmer-Weber and Stranski-Krastanov growth modes are presented. The arrows indicate the direction of structures with bigger amount of epitaxial material.

Frank-van der Merwe growth mode occurs when there is no lattice mismatch between the substrate and the epitaxial layer and the surface energy $\sigma_2 + \gamma_{12}$ is not sufficient to produce self-organization. In this mode epitaxial layers can be grown without relaxation as thick as needed. The situation can be observed for example when a (Zn,Be)Se layer containing 2.83% Be is grown on the GaAs substrate. Since both the layer and the substrate are lattice-matched there is no strain.

Volmer-Weber growth mode also does not require lattice mismatch. However, when the surface

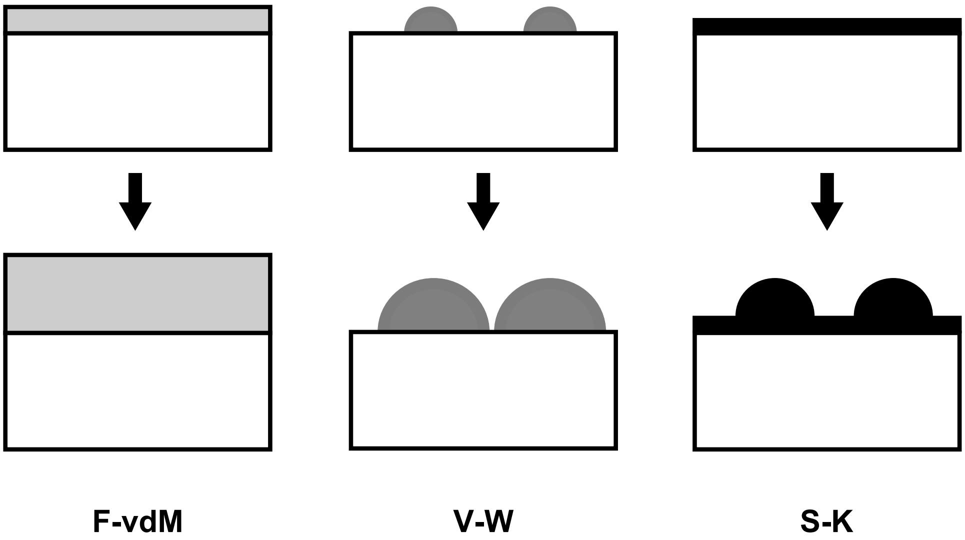

Figure 2.19: *Schematic presentation of (from left to right) Frank-van der Merwe, Volmer-Weber, and Stranski-Krastanov growth modes. (after [EC90])*

energy $\sigma_2 + \gamma_{12}$ exceeds some defined material dependant value a formation of self-organized islands on the surface occurs. The growth mode may be compared with segregation of water droplets on a Si surface, which is basically a dewetting process.

Finally, Stranski-Krastanov growth only occurs on lattice-mismatched substrates. The misfit between the substrate and the epilayer produces strain in the layer, which accumulates as the epilayer grows thicker. After some critical thickness the strain relaxes producing islands with lower strain energy.

The original publication by Stranski and Krastanov [SK38] suggested that the growth of two materials with different lattice constants would result in the formation of islands instead of flat layers beyond a critical thickness. The first strain-induced islands were reported by Goldstein et al [GGM$^+$85] in 1985, who discovered that InAs islands were formed on GaAs. These islands can have sizes in the range of a few nanometers and can confine charge carriers in both conduction band and valence band.

In the experiments described here, Stranski-Krastanov growth was used to form self-assembled CdSe quantum dots on (Zn,Be,Mn)Se surfaces. Since there is an essential lattice mismatch between the two semiconductors (about 7%) well defined quantum structures can be grown.

To better understand the properties of self-organized quantum dot, the dynamics of the dots formation need to be understood. A qualitative illustration of the change in the total energy of a lattice-mismatched epilayer versus deposition time is shown in Fig. 2.20.

In the beginning, the deposition follows a 2D layer-by-layer mechanism which leads to a perfect wetting of the substrate. Accumulated elastic strain energy increases linearly with the deposited volume (region A in the figure). At the critical wetting layer thickness point tcw, the growth

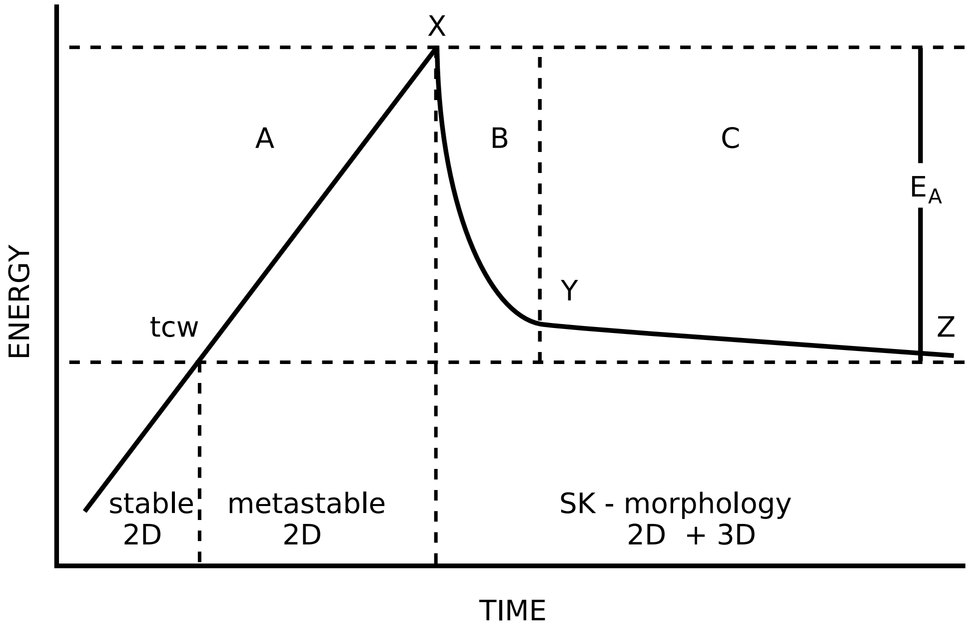

Figure 2.20: *Change in total energy during deposition. A: 2D layer-by layer growth, B: 2D-3D transition. Between Y and Z a slow ripening process continues. Further explanations in the text. (after [SCM$^+$96])*

transforms into metastable 2D growth. This means that the epilayer is potentially ready for a transition to a Stranski-Krastanow morphology. The extension of this range of metastability (and with it the amount of material which is available for the 3D island growth) depends primarily on the height of the transition barrier E_A.

Exactly at point X, the excess energy of the strained 2D layer reaches the energy of a 2D-3D transition barrier E_A and a pure strain-induced 2D-3D transition becomes possible. However, we have to consider that at real growth temperatures, a thermally activated nucleation sets in before reaching X. This is caused by thickness fluctuations in the strained layer, which lead to the formation of critical nuclei.

As soon as the first islands are created, the excess energy decreases due to partial strain relaxation (region B). The islands grow, consuming the material that is available and mobile enough to reach the islands. Due to an increase of the activation barrier for thermally activated nucleation the nucleation probability decreases. This determines the surface density of the dots.

The absolute growth rates can be extremely high in the beginning of the island formation. This is caused by the strain-induced decomposition of parts of the wetting layer. In just a few seconds, the islands grow to a height of several nanometers even if very low material fluxes are supplied.

In region C of Fig. 2.20 the process has lost most of the excess energy. The mobile material is consumed, and the potential differences between slightly smaller and larger islands maintain a further slow reaction, mediated by surface diffusion, towards equilibrium (Ostwald ripening or stable dot-arrays) [SCM^{+}96].

At the final stage of the sample preparation the dots are normally covered by a layer of the barrier material to prevent the influence of surface effects on the structural properties.

2.4.2 Optical investigation of semimagnetic quantum dots

In order to investigate the properties of II-VI CdSe quantum dots, multiple detailed investigations including high resolution X-ray diffraction and optical and magnetotransport measurements of the samples, were performed.

The substrates were prepared as described in Section 1.3.

First, an undoped, lattice matched to the GaAs substrate, 300 nm (Zn,Be)Se layer containing 3% Be was grown. It was followed by a 50 nm ZnSe layer which served as a substrate for growth of CdSe quantum dots. Following a 10 second pause under Se flux, the CdSe growth started by opening the Cd shutter.

The CdSe growth time had been selected to deposit an amount of the material equivalent to the growth of an epitaxial layer with a certain width varying between 0.6ML and 3ML. The next 10 second pause was introduced by closing the Cd shutter. During the pause RHEED patterns have been transformed into a spotty image, indicating nucleation and growth of self-organized CdSe quantum structures.

After growth of a protecting 25 nm thick ZnSe layer the samples were cooled down and taken out of the MBE system. The samples were then removed from the molybdenum blocks at 210 °C, cut into small pieces, and characterized.

Preliminary sample characterization may be done using high resolution X-ray diffraction. It is a very powerful characterization technique since it is very sensitive to change in crystallographic characteristics of epitaxial layers, as well as to properties of their interfaces. However, due to the small size of the quantum dots, the intensity of the diffracted HRXRD signal is so small, compared to the background, that it is very challenging to see the effect in a standard measurement configuration. Changes to the crystalline quality of the top and bottom ZnSe layers are negligible as well.

A tiny, but more straightforward, effect on HRXRD measurements can be explained by treating the CdSe quantum dots layer as an additional interface between two ZnSe layers. It is possible to simulate the expected diffractograms, and by comparing the simulation with experimental data, extract layer parameters, such as the amount of deposited material in the quantum dot layer. For simplicity, it is better to maintain a high symmetry of the structure, for example by growing ZnSe layers of the same thickness below and above the quantum dots.

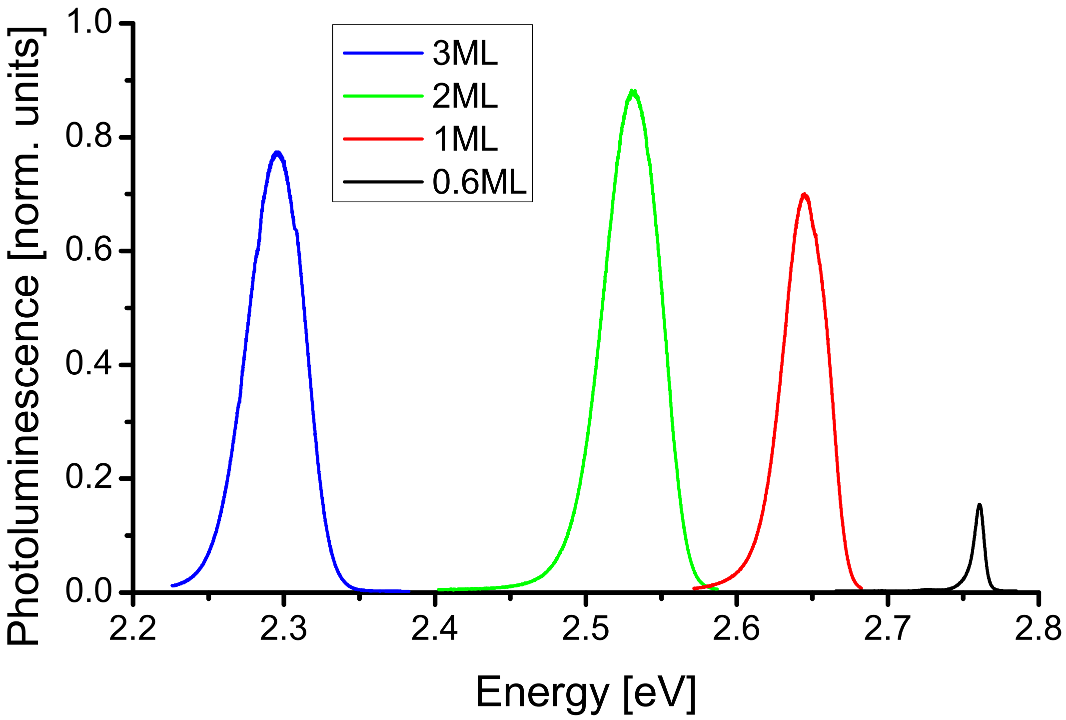

Figure 2.21: *Normalized photoluminescence spectra of CdSe quantum dots incorporated in a ZnSe matrix. The ground-state exciton transition peaks for the samples of different growth times can be observed.*

To access the optical properties of the quantum dots, magneto-optical measurements were performed. The experimental configurations allow for photoluminescence, reflectivity and transmission measurements. Unfortunately, due to the small band gap of the GaAs substrates used in these experiments, the last measurements technique could not be applied.

A set of photoluminescence spectra of CdSe quantum dots grown between two ZnSe layers is presented in Fig 2.21. The measurements were performed in ^4He magneto-optical cryostat at 1.6K. The samples were excited with the ultraviolet lines of an Ar-ion laser. The luminescence from the ZnSe layer is strongly suppressed by the dominating luminescence from the quantum dots and the GaAs substrate. The GaAs substrate exciton peak is well pronounced and is located at 1.49 eV.

A photoluminescence data of CdSe quantum dots with the growth time equivalent to the deposition of a 3ML of CdSe layer is presented in blue. The green curve represents the data from quantum dots with 2ML nominal thickness, the red curve represents the spectra of 1ML quantum dots, and the black curve represents quantum dots of 0.6ML deposition time.

A well-defined photoluminescence peak for each of the samples is observed. The energy position of the peak changes as the growth conditions change. The peaks correspond to the ground-state exciton transition in CdSe quantum dots.

As the size of the deposited layer decreases, the energy position of the exciton peak moves to higher energies. This means that the size of the individual quantum dots decreases, leading to an increase in exciton confinement inside of the quantum dot.

The peak located at 2.53 eV represents the 2ML sample. The highest normalized photoluminescence intensity of 0.87 as compared to other samples, indicates the best three-dimensional exciton confinement. This layer is closest to three-dimensional structures on top of the wetting layer which was described previously. The quantum dots consume most of the mobile material of the wetting layer, thus creating well-defined structures with strong carrier confinement.

The peak located at 2.76 eV has a normalized intensity of 0.15 and is representative of the 0.6 ML sample. This structure can hardly be defined as quantum dots because the strain energy accumulated in the layer is not sufficient to overcome the potential barrier of the Stranski-Krastanov growth. This means that the layer is grown strained on the ZnSe substrate. Since the supplied material is not enough to form a complete CdSe layer, the photoluminescence peak most likely comes from the region of (Zn,Cd)Se alloy which locally modifies the energy profile.

The photoluminescence measurements show that the best optical properties and three-dimensional confinement can be achieved for the samples having a deposition time equivalent to growth of 2-2.5 monolayers CdSe. Still, by using samples with different sizes and compositions, it is possible to tune the position of luminescence peak when needed.

Due to the confinement of carriers in self-organized structures, many low-dimensional effects start to play a significant role. The influence of confinement effects on interactions in magnetic material is an interesting question.

Using time-resolved Kerr rotation, interaction dynamics in 1.4ML CdSe quantum dots doped with magnetic impurities were investigated [SKW$^+$06]. The samples with a nominal Mn concentration of 0.5, 1, 2, and 4 percent show a strong evidence of an enhancement of the spin coherence time with respect to higher dimensional structures. The enhancement is observed for both the carrier and the manganese system.

A monoexponential decay of the time resolved Kerr rotation signal with a time constant of $T_2^* = (630 \pm 70)$ ps for the sample containing 2% Mn in the quantum dots was found. This is larger (by more than a factor of 2) than what had been obtained so far in higher-dimensional structures.

An increase in Mn spin coherence times in the absence of photoinjected carriers. is attributed to the fact that the local spin distribution in QDs gets strongly reduced, e.g. spin diffusion as compared to bulk material or quantum wells. This limits spin-spin interaction and spin-lattice relaxation to a small volume of the crystal.

Apart from the long spin coherence times of magnetic atoms and polarized carriers, the local interaction induced ordering of magnetic atoms is specific to the quantum dots. This is described in the next Section.

Due to the small dimensions of the dots, even tiny changes in their shape leads to an immense effect on the electrical and optical properties. The changes lead to strong anisotropy in the characteristics of the quantum dot ensembles and of individual quantum dots.

The morphology of the surface on which CdSe quantum dots are grown over plays an important role in defining the properties of the quantum dots. Therefore, at certain growth conditions, CdSe quantum dots grow strongly anisotropic.

Lower symmetry of the dots can for example induce quantum interference between linearly and circularly polarized photon states. The interference leads to circular-to-linear and linear-to-circular conversion of optical polarization [AKP$^+$06].

The polarization conversion occurs in CdSe quantum dots under continuous wave excitation in the absence of any magnetic field.

Provided additional technological efforts conversion values up to 50% can be achieved, despite the fact that in investigated structures circular-to-linear and linear-to-circular conversions typically do not exceed 3%.

2.4.3 Transport investigation of quantum dots by means of resonant tunneling

As was discussed in Section 2.3.1, magnetic RTDs can be used to produce a controllable spin polarization of a passing current. The same devices can be used to detect the spin polarization of incoming carriers (section 2.3.2). Still the devices require an external magnetic field to be applied during their operation.

Individual quantum dots can be investigated by growing them in a tunnel barrier stack because quantum dot ensembles have a certain size distribution. During the tunneling process, as voltage increases, levels of a single quantum well are aligned with the Fermi level in the injector. For some of the dots (the thicker ones) the barrier is thinner and their respective tunneling currents thus exponentially dominate the I-V characteristics. The levels of the quantum dots in the ensemble follow only after a certain voltage spacing [VLP$^+$00].

Properties of an individual quantum dot are altered in the presence of an external magnetic field. The changes in properties of the dot can be monitored by magnetotunneling spectroscopy. This lead to the observation of spin-splitting in a single InAs self-assembled quantum dot in AlAs [TIM$^+$98]

In our experiments magnetotunneling spectroscopy was applied to investigate the influence of an external magnetic field on the interactions of magnetic ions located in the vicinity of self-organized quantum dots. A sample was prepared, in which the active part remained a reso-

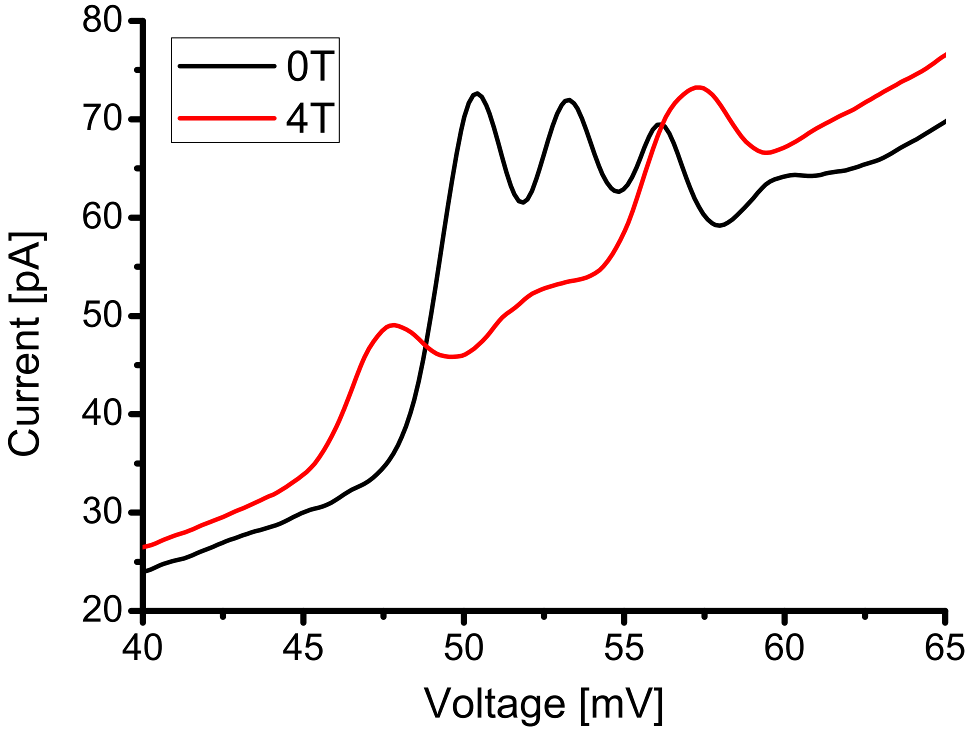

Figure 2.22: *Effect of applied magnetic field on current-voltage characteristic of a RTD with quantum dots embedded into (Zn,Be,Mn)Se DMS barriers*

nant tunneling diode, except that the quantum well between the barriers was replaced by self-assembled CdSe quantum dots with a growth time equal to the deposition of 1.3 monolayers of material.

As barrier material a (Zn,Be)Se layer containing 30% Be mixed with 6% of Mn magnetic ions was used. In this way the quantum dots were surrounded by a DMS (Zn,Be,Mn)Se. The rest of the structure was similar to the devices described in Section 2.2.2.

A mesa structure of 100x100 μm^2 was prepared. When voltage is applied to the device, resonant tunneling peaks on the I-V characteristics indicate the positions of the resonance levels in the quantum dots. An external magnetic field induces the orientation of magnetic ions in the barrier, and, in this way, influences the properties of the quantum dots. The overlap of the dot's electron wave function with the surrounding Mn.

As was olready mentioned, an individual quantum dot comes into resonance at lower voltages, way before the rest of the ensemble. Fig 2.22 presents the current-voltage characteristics of the device taken in ^4He cryostat equipped with superconducting 6T magnet at 1.3K. The black curve presents I-V characteristics without an external magnetic field applied and a I-V characteristic of the device at the 4T external magnetic field is presented in red. The figure shows only the part of the I-V characteristics related to the resonant tunneling through a single quantum dot state. Resonance peaks of the ensemble of quantum dots appear at voltages above 100 mV and can be found in other sources [Slo05].

On the zero magnetic field curve three resonance peaks can bee seen; the peaks correspond to tunneling through levels of an individual quantum dot. As an external magnetic field of 4T is applied, the two side resonance peaks shift apart and the middle peak decreases in intensity. While the nature of the middle peak is difficult to describe, the two side peaks can be attributed to two spin-degenerate sublevels of a single quantum level in the quantum dot [Slo05].

A separation of the resonance peaks and related sublevels in the quantum dot can be expected from the interaction of an electron wave function localized in the quantum dot with magnetic ions in the vicinity of the dot. Although the splitting varies from dot to dot, the individual value and the magnetic field dependence of the splitting remain unchanged during multiple cooling cycles.

The zero field splitting of the resonance peaks related to spin degenerate sublevels without a magnetic field is a novel feature of this device. It is the first experimental observation of a zero-dimensional induced magnetic interaction.

The sublevels are split at a zero magnetic field because of an electron mediated local interaction of Mn atoms located on the vicinity of the quantum dot [GSS^{+}06].

Due to the interaction, a magneto-polaron type complex is formed, which is not stable in bulk material, but is stabilized by zero-dimensional impurities, such as the quantum dots [HGQ91].

The effect has not been observed in optical measurements on similar quantum dots, and also the strong temperature stability is unexpected. We assume that the current flowing through the device by a feedback mechanism stabilizes the splitting [QH05].

Without the external magnetic field, precise orientation of the spin-spit sublevels is undefined. As the magnetic field rises, it first orients the direction of the magnetic ions coupled by ferromagnetic interaction and then starts to induce additional splitting between the sublevels.

Chapter 3

(Zn,Mn)Se on silicon

One of the main goals of the field of spintronics is the search for novel ways to use spin properties of particles. In this context the material science is of great importance. The search for novel materials with long spin-flip times, materials that can produce a high spin polarization, applications of nanostructures for performing computations, and the spin transfer trough interfaces are among the most important directions of current research activities in the field.

Since electrical spin injection from a ferromagnetic metal into a diffusive semiconductor is fundamentally prohibited by the conductivity mismatch problem [SFM$^+$00], other methods for injecting spin-polarized carriers must be used. Dilute magnetic semiconductor (DMS) injectors are recognized as one of the most frequently used solutions to the problem.

As a material for the generation of spin-polarized carriers DMS (Zn,Mn)Se has been chosen, as it is proven to be an efficient spin-injector. Magnetic properties of the semiconductor are well known and high-quality epitaxial films are grown routinely.

Although electrical spin injection from (Zn,Be,Mn)Se into GaAs has been demonstrated succesfully, silicon seems to be the best material for spin injection based devices. It possesses a series of material properties which are extremely interesting for spintronics. Furthermore, the current semiconductor industry is almost exclusively based on silicon, and using this material, an addition of novel (quantum mechanical) functions without too many additional costs would be feasible for modern devices.

However multiple challenges arise while trying to combine DMS and silicon during epitaxial growth.

As a result of careful optimizations and an innovative approach, the quality of epitaxial (Zn,Mn)Se layers was able to be significantly improved, resulting in observations of high crystalline, optical, magnetical, and electrical properties.

3.1 Comparison of (Zn,Mn)Se and Silicon

There is an essential difference between (Zn,Mn)Se and silicon. The first, and the most remarkable, distinction is that the first one is a compound semiconductor and the second a single element semiconductor. Compound semiconductors must maintain a certain element order in the lattice, whereas for single element semiconductors, it is enough to keep the lattice order.

Since compound semiconductors can be grown from separate elementary effusion cells, a single reconstructed surface (for example [001]) can be easily prepared. This is done by covering it, during the epitaxial growth, with only one kind of atomic species. Since the atoms can occupy only one sublattice in the elementary cell, such a surface is formed by the defined sublattice. In a zinc-blende structure, this means that the surface contains only double-atomic steps. To achieve similar steps is very challenging in single-element semiconductors because the atoms can occupy both sublattices in the elementary cell.

The difference in the lattice constants of the semiconductors (5.43Å for silicon and 5.67Å for ZnSe) presents an additional difficulty for epitaxial growth of the semiconductors (see Section 1.3).

There is a pronounced difference in the band gap of both materials, as well. (Zn,Mn)Se can change its band gap as well as its lattice constant depending on the Mn concentration (see Section 1.1.2) while the band gap of silicon is constant at defined conditions.

Another difference is that (Zn,Mn)Se is a direct-band gap semiconductor and silicon is an indirect one. The epitaxial growth of direct band gap materials on silicon has been long recognized as an important step in integrating optoelectronic devices into standard electronics [NHJ$^+$87]. However, this is not a primary goal of this study.

Finally, (Zn,Mn)Se is a diluted magnetic semiconductor; when an external magnetic field is applied, it exhibits a giant Zeeman splitting, leading to a high spin-polarization of the mobile carriers, as described in Section 1.1.3. Silicon, on the other hand, has a very good crystal symmetry and, therefore, can preserve the spin-polarization of free carriers for a very long time.

Relevance to spintronics

The last-mentioned property of silicon is a very attractive feature for spintronics and quantum information processing. As the particles' spin life times increase, it is possible to put more active elements on their way in order to use the spin degree of freedom. The qubits during quantum computation are able to perform more operations without loosing the coherence.

To quote some numbers, it has been shown that the transverse relaxation (decoherence) time,

T_2, in silicon exceeds 60 ms for an isolated spin [TLAR03].

Hence, it is desirable to combine the two materials in order to create spin-polarized carriers in one of them, and use the spin-polarization in the other. The option can provide compatibility with standard silicon electronics and may open up a series of new perspectives for device design.

A few obstacles make the growth of (Zn,Mn)Se on silicon very difficult. First, the Si (100) surface is very reactive. Therefore, special measures must be taken to prepare a reliable surface for further epitaxy. Second, the lattice mismatch between Si (100) and (Zn,Mn)Se is quite large. The band gap difference presents yet another difficulty. The band offset at the interface does not improve the picture, either.

The lattice mismatch of 4.3% can be in principle compensated by adding 45% Be in a (Zn,Be)Se alloy [CTF00]. This approach leads to an improved crystalline quality of the compound, but optical and electrical properties change respectively (see section 1.1.2).

In addition to the other effects described, high Be contents have a big influence on the doping of the samples. The maximum doping of the layers strongly decreases with increasing Be concentration, and a (Zn,Be)Se layer containing 45% Be can barely be *n*-type doped (see Section 1.1.2).

Since low temperature electrical measurements need to be performed, which are impossible without doping, the experiments needed to be restrained to lattice-mismatched growth with low Be content.

Despite all the challenges, a substantial progress in the investigation the ZnSe/Si (100) interface has been achieved [BBS+92]. This development shows that, using sophisticated growth procedures and a smart sample design, most of the obstacles can be overcome.

3.1.1 Surface morphology of (Zn,Mn)Se (100) and Si (100)

The crystal structure of both semiconductors is slightly different. (Zn,Mn)Se as crystallizes into a zinc-blende lattice (see Section 1.1.1), whereas silicon crystallizes into a diamond. The diamond lattice is similar to the (Zn,Mn)Se one, but is made up of atoms of one kind. Therefore, the crystals are compatible from the growth point of view.

In the [001] direction, the (Zn,Mn)Se crystal may be considered as an ordered sequence of Zn and Se layers. A change in the sequence of the atomic layers produces a defect known as an antiphase boundary (APB), which will be discussed later. A stacking fault is produced by a change in the order of atoms inside the layers, which is normally the result of a change in the orientation of elementary cells caused by a change in the dimer orientation of the substrate.

The diamond lattice consists of two interpenetrating face-centered cubic sublattices, which dif-

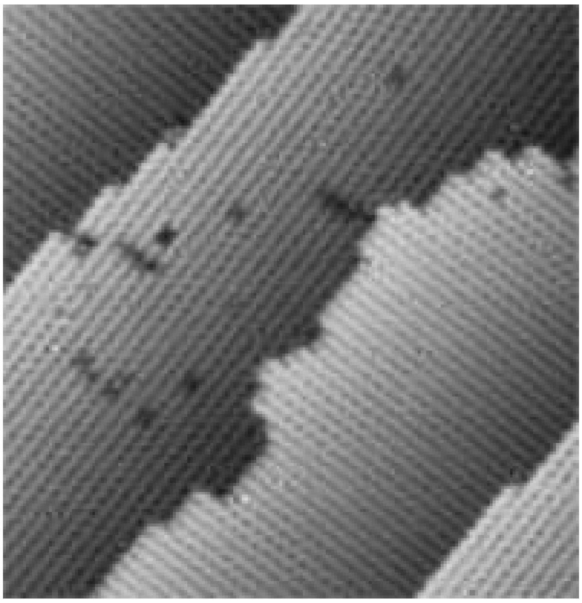

Figure 3.1: *Filled-state scanning tunnel microscopy image of Si (100) - (2x1). The image dimensions 29×29 nm^2. (after [YT97])*

fer from each other only in the spatial orientation of the four tetrahedral bonds that connect each atom to its four nearest neighbors. There is no distinction between the two sublattices otherwise; both are occupied by the same atomic species.

For the surface, this means that single atomic steps lead to a change in the dimer orientation for the two planes. Since it is very difficult to prepare a silicon surface without single atomic steps, it is very difficult to receive a surface with a single dimer orientation.

Fig. 3.1 shows an atomic resolution scanning tunneling microscopy image of Si (100); the image was taken in UHV conditions at room temperature [YT97].

A change in the dimer orientation at atomic step edges can be observed. The orientation of the dimers defines the spatial position and degree of freedom of surface atoms, and this is crucial for the epitaxial growth of compound semiconductors, as was already mentioned.

One of the most common methods to prepare a silicon surface with single dimer orientation is the use of tilted substrates. Experimental observations have shown that a Si (100) surface misoriented towards (011) azimuth by an angle of more than 4° exhibits a single domain orientation of surface atoms after careful annealing [Cha87]. The transition of the surface reconstruction is possible because single-layer steps disappear in favor of double-layer steps. A double-stepped surface with single-dimer orientation in the direction parallel to the step edges is observed.

Detailed calculations show that the step energies favor double-stepped surfaces in the case of tilted surfaces [ABJ$^+$90]. At the same time, the strain relaxation energy is strongly temperature dependant and leads to strong fluctuations of more energetic steps having dimer orientations

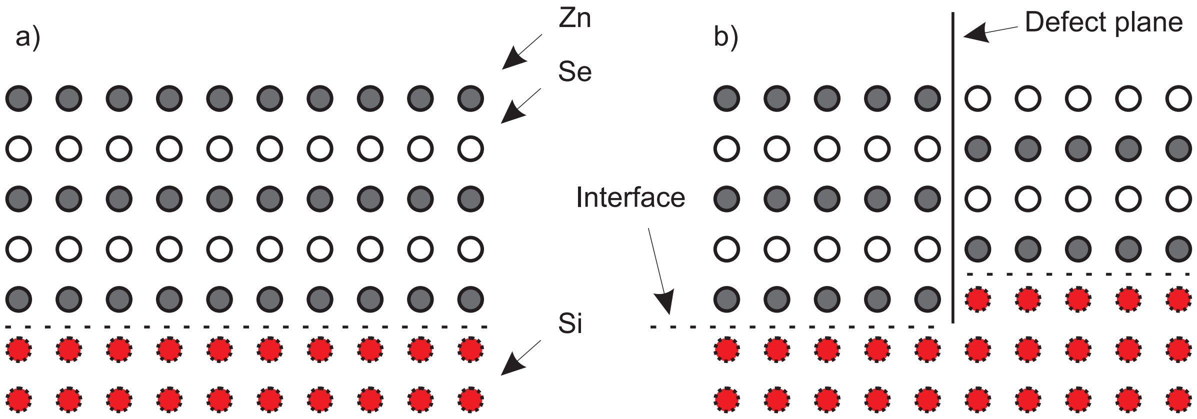

Figure 3.2: *Schematic presentation of an antiphase boundary(APB): a) ZnSe grown on flat Si surface b) single step on Si (100) surface producing ZnSe crystal with APB*

parallel to the step edges. As a result, only the defined temperature range may lead to a stabilization of the double-dimer steps.

Since the double-step surfaces are formed in a probabilistic way, and the process is done at some defined temperature (other than zero, as was assumed by some theories), the surface necessarily exhibits some imperfections of dimer orientations, thus leading to the defect formation. The defects (such as a single atomic step) disturb epitaxial growth, and therefore should be avoided.

The process is demonstrated by the following example: In a crystal without antiphase disorder, the sublattice allocation is the same throughout the crystal Fig. 3.2(a). This means that the (Zn,Mn)Se compound, being a polar semiconductor, can be grown on the surface by preparing an atomic coverage through Zn atomic flux exposure for a time sufficient to create a single monolayer (as is shown in Fig. 3.2(a)). On top of the Zn layer, the Se layer is deposited, and on top of it, Zn is deposited again, and so on. Therefore, the rest of the crystal is grown defect free.

However, if the sublattice allocation changes, as is shown in Fig. 3.2(b), the interface between domains with opposite dimer orientations forms a two-dimensional structural defect [Kro87] in the polar semiconductor, called an antiphase boundary (APB). Since the sublattice allocation necessarily changes on single atomic steps on the Si (100) surface, as indicated by the change in dimer orientation, the APB is bound to single atomic steps.

The APB is created in (Zn,Mn)Se, when it is deposited on top of the Si (100) surface containing single atomic steps. For demonstration purposes the deposition process is assumed to be initiated by deposition of a single Zn atomic layer. Then, all of the planes separated by single-atomic steps on the silicon surface are covered with Zn. This means that the next Se layer covers Zn and forms a plane perpendicular to the growth direction. The plane extends until it reaches another plane, separated by a single-atomic step, but this plane is already occupied by Zn.

As was previously mentioned, zinc-blende crystals must maintain not only the position of atoms in the crystal, but also a defined order of the atoms. In the case of (Zn,Mn)Se crystals grown on top of a single atomic step on the Si (100) surface, the order of atoms is broken. This change in atomic order is an APB, which leads to bonding defects in the plane joining the two sides.

APBs are expected to give rise to deep levels inside the band gap and to act as strong scattering centers for electrons and holes [Kro87, PC87, Pet86]. So, the APBs are very likely to impact the electrical performance of the devices.

One of the ways to deal with such defects requires precise engineering of the growth of large-diameter crystals to ensure that entire planes form simultaneously [VS06]. Unfortunately, this is a very challenging task for a perfectly (100) oriented silicon surface.

Another possibility to decrease APB is to stimulate a strong defect interaction during early growth stages and to choose appropriate growth conditions to reduce APB density through self-annihilation.

It has been shown, by an example of GaAs layers grown on Ge substrates [HK01], that the antiphase boundaries annihilate each other after a thick 3 μm layer of GaAs. Since the lattice mismatch between GaAs and Ge is smaller than the mismatch between (Zn,Mn)Se and Si (100), the defect interaction is expected on the early stages of epitaxial growth.

In our experiment low-temperature growth initiation was used, combined with atomic layer epitaxy and followed by a migration-enhanced epitaxy [SRF$^+$04]. As a result, a highly three-dimensional growth start occurred, leading to a strong defect interaction and a substantial improvement in crystalline quality. The interaction reduced APB density through self-annihilation. Sequential molecular beam epitaxy was done at standard growth temperatures.

3.2 Si (100) surface preparation and characterization

3.2.1 Modified RCA Si (100) surface preparation

The RCA cleaning [KP70] sequence developed by Werner Kern in the 1960s is still used widely in semiconductor manufacturing as a critical clean for the removal of organic, metallic and particle contamination on wafer surfaces prior to oxide growth.

In more recent years, a few modifications were introduced to the process in order to achieve cost-effective cleaning and high-quality thin oxides [HBC$^+$99, CSY00].

In order to prepare a suitable Si (100) surface for further heteroepitaxy several different techniques were tried. Most of them produced reliable surfaces that normally contained a thin oxide layer, which had to be removed in the MBE system by thermal annealing at very high temperatures. The annealing leads to a strong degradation of the surface properties. Therefore, it is

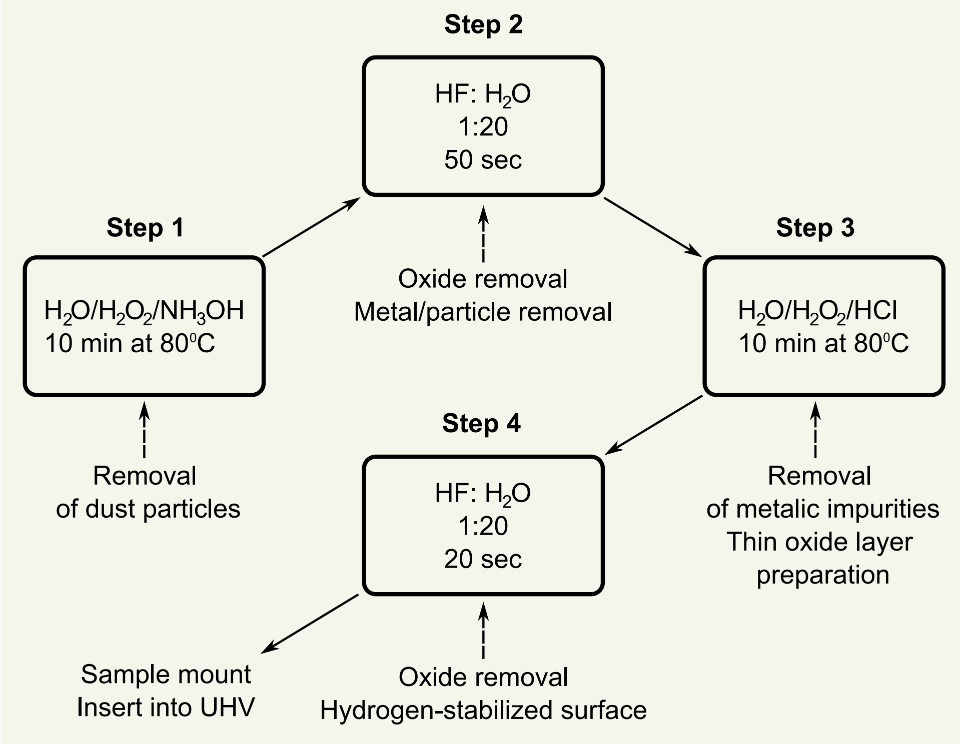

Figure 3.3: *Schematic illustration of the low-temperature Si (100) substrate preparation process*

desirable to limit substrate preparation to low temperatures and avoid high-temperature surface treatment.

As a result, the modified RCA cleaning procedure [IS86] with subsequent hydrogen passivation was found to be the most suitable for the used molecular-beam epitaxy system. The process was simplified in many ways because of advances in the quality of commercially available substrates

Fig. 3.3 presents a schematic illustration of the cleaning process.

Firstly, high-quality, commercial wafers were cleaned with dry nitrogen. Then, the silicon wafers were dipped into a H_2O:H_2O_2:NH_3OH (5:1:1) solution. This alkali treatment removed particle and some organic contaminants from the silicon oxide surface. The solution was heated in a flow box together with the wafers to 80 °C for 10 minutes. Concurrently, the H_2O:HCl solution was prepared and heated to 80 °C.

Then, the samples were cooled down to room temperature by filling the solution with deionized water and rinsing the wafers in running deionized water for 2 minutes.

Secondly, the Si (100) surface was etched with weak solution of hydrofluoric acid HF:H_2O (1:20) for 50 second. This removed natural oxide and cleaned the surface from metals and other particles. At the same time, the HCl solution was completed by adding H_2O_2.

During the next step, the samples were slowly removed from the HF solution and immediately inserted into the H_2O:H_2O_2:HCl (5:1:1) solution where the samples were boiled for 10 minutes. This acid treatment removed metal impurities and prepared a very thin oxide layer. The layer protects the surface from chemisorption of such contaminants as carbon.

After cooling as described above, the samples were emerged into another container of HF:H_2O (1:20) for 20 second. This treatment was one of the most important in the process, since during this step, the thin oxide was removed and replaced with hydrogen passivation.

The obtained hydrogen passivation was found to be stable in air for at least 30 minutes. During this time, the wafers were mounted on molybdenum blocks and transferred into the ultrahigh vacuum (UHV) MBE system. Indium was used as an adhesive to mount the substrates on the molybdenum blocks by heating it to temperatures of about 210 °C, which is below the hydrogen desorption temperature.

3.2.2 Si (100):H surface

Since the hydrogen passivation is a very crucial step, an explanation of the processes happening on the Si (100) surface during HF treatment follows:

Peroxide solution chemical oxidation was used, followed by oxide removal in HF solution. While the procedure leads to very smooth and chemically stable surfaces, the etching mechanism is not trivial.

It has been suggested that the resulting near-perfect chemical stability of the surface is due to F passivation. This suggestion had been brought up by the fact that the Si-F bond strength is more than six times stronger than that of Si-H, and had been supported by the commonly excepted mechanism of oxide removal. However, it has been experimentally shown that the chemical stability of these surfaces is, in fact, attributed to surface passivation by hydrogen [YAC$^+$86]. A more detailed understanding of the process came from a complex theoretical investigation [TRHC90].

A schematic illustration of the cleaning process is shown in a sequence depicted in Fig. 3.4.

Fluorination of the surface silicon and hydrogenation of the second-layer silicon are due to insertion of HF into Si-Si bond [Fig. 3.4(b)]. The latter is performed through the polarization of the silicon back bond by Si-F, which has an ionic nature.

The second HF is inserted in the Si-Si bond on the other side [Fig. 3.4(c)] and the sequence is completed by the removal of the surface silicon atom as an SiF_4 complex, as it is schematically depicted in Fig. 3.4(d). This leaves a hydrogen terminated surface.

The resulting surface may have different forms of H-termination (monohydride, dihydride, and

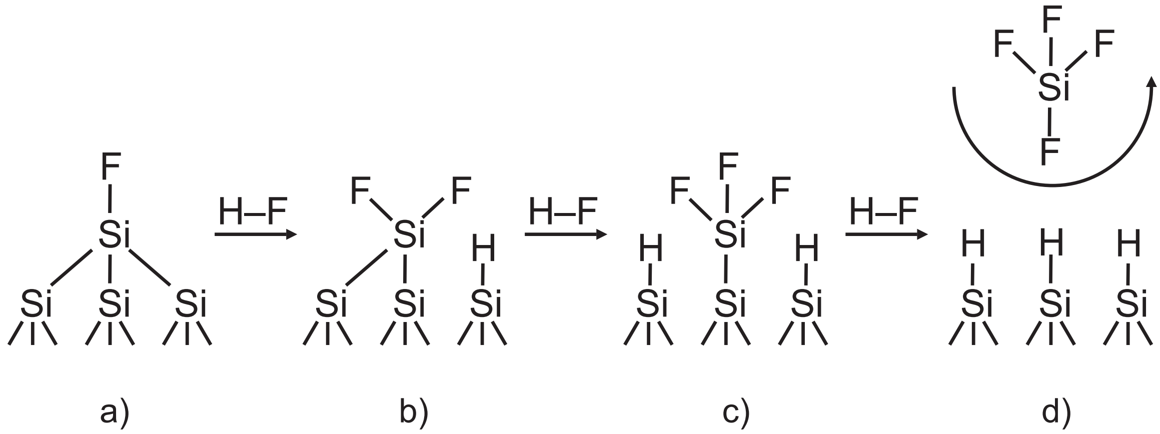

Figure 3.4: *Schematic illustration of H passivation mechanism (after [TRHC90])*

trihydride) depending only on the initial structure of the Si/SiO_2 interface. The reactions leading to a H-terminated surface are more exothermic and more energetically accessible as compared to F-terminated ones.

It has been suggested that the final rinsing of the hydrogen-terminated Si (100) surface in ultrapure water may lead to a more uniform distribution of the termination. However, a detailed investigation using atomically resolved scanning tunneling microscopy of H-terminated Si (100) surfaces after HF cleaning shows that the 1x1 dihydride structure disappears when the surface is subsequently rinsed with ultrapure water [AEK$^+$00].

When Si–H bonds are formed, H atoms attract electrons because the electronegativity of an H atom is larger than that of a Si atom. In the (1×1) dihydride structure, two H atoms belonging to the neighboring Si atoms are in close proximity. Thus, a strong repulsive force occurs between them, causing the surface to become unstable. OH ions are generally known to etch Si surfaces, and ultrapure water contains a large number of OH ions. It has been suggested that every other row of the ideal (1×1) dihydride surface is etched preferentially by OH ions in ultrapure water, leading to (2×1) surface reconstruction.

Such a surface exhibits over a large area, row structures in [110] and $[1\bar{1}0]$ directions, as well as pyramidal-shaped etch pits, which are caused by anisotropic etching with OH ions [EAK$^+$98]. The structures disturb further epitaxial growth and it is recommended to avoid dipping a Si (100) surface into ultra pure water after H passivation and, instead, immediately proceed with further sample preparation.

3.3 Growth of (Zn,Mn)Se on Si (100) surface

3.3.1 Hydrogen desorption and arsenic passivation of Si (100) surface

After degassing at 300 °C for 15 min, the molybdenum blocks were transferred to the III-V growth chamber. Immediately after the transfer, the Reflection High-Energy Electron Diffraction (RHEED) showed (1×1) patterns typical for dihydride surface passivation, as was mentioned before. Hydrogen atoms on such a surface are very stable at temperatures below 600 °C [RH99].

At temperatures above 650 °C, hydrogen diffusion becomes very efficient, leading to more nonequilibrium surface coverage (especially on terrace steps). As the temperature is increased further, the dihydride desorption rate reaches its maximum at approx. 700 °C, and at temperatures about 800 °C, monohydrate desorption takes place [RH99].

From the temperature at which hydrogen desorption takes place, it is possible to determine the nature of hydrogen passivation and use this data for further optimization of the surface preparation procedure.

Since our case, the Si (100) preparation process was optimized to create dihydride passivation of the surface, heating of the samples to approx. 730 °C under constant arsenic flux leads to a change in the RHEED patterns. The patterns changed from (1×1) of a hydrogen-covered surface to (1×2) of a clear silicon surface as a result of the hydrogen passivation desorption [EHC91].

Arsenic works as an efficient surfactant. The surfactant changes the energy barrier needed for the hydrogen atom to desorb from the surface, and in this way, slightly reduces the temperatures needed for the desorption.

Since, after hydrogen desorption, the Si (100) surface is left with dangling bonds that increase reactivity of the surface and modify its morphology, extra measures have to be taken to compensate for the bonds. In Fig. 3.5, a schematic presentation of the Si (100) surface after hydrogen desorption is shown. The dangling bonds appear as a result of unpaired bonds of silicon surface atoms sticking out. The bonds are responsible for high Si (100) surface reactivity and lead to dimer row formation. In fact, the dimer rows are not absolutely symmetric and are buckled in one orientation. The tilt in the dimer position is especially pronounced on stepped surfaces because of the induced anisotropy, which orients all the dimers to have the same buckling direction [BBS$^+$92].

Buckling of the dangling bonds leads to twinning of (Zn,Mn)Se crystal during further epitaxial growth. This means that the crystal planes are tilted in comparison to the substrate. The tilt is sensitive to the substrate miscut (i.e. in the [011] direction) and is about 5°. In addition, a high density of stacking faults, or microtwins, is formed because of the tilt. They separate

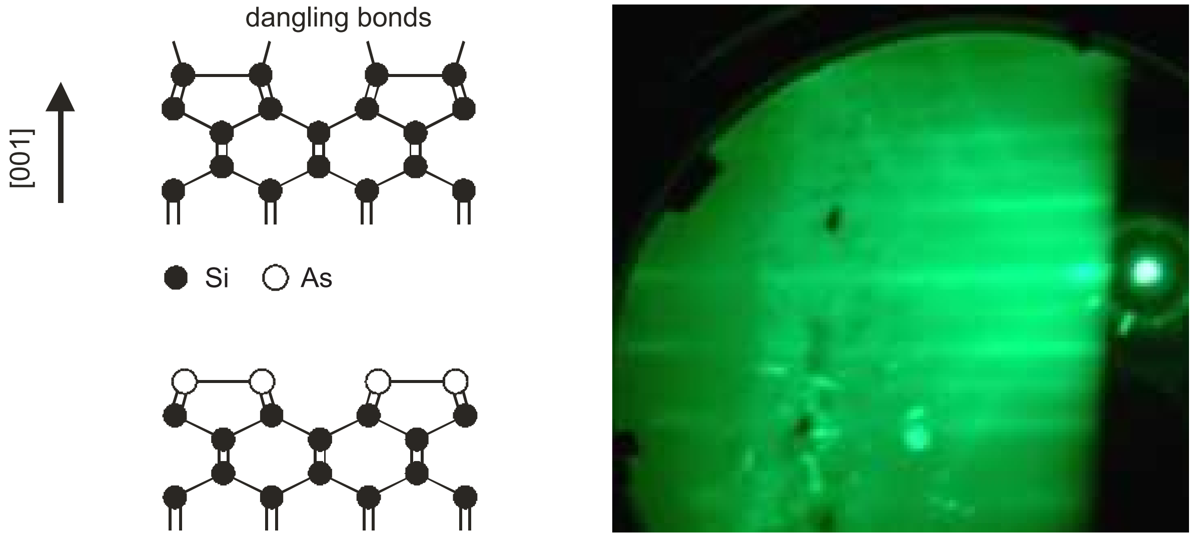

Figure 3.5: *Schematic drawing of pure Si (left top) and As-passivated (left bottom) surfaces and a RHEED image of As-passivated surface showing (1x2) reconstruction (right).*

tilted and untilted fractions of the crystal. As a result of anisotropy in the dimer, the buckling of the microtwins extends mainly in one direction. This leads to a weak interaction between the defects and degrades the quality of the epitaxial films.

The problem can be solved by placing As as an interlayer separating Si and II-VI crystals. The layer saturates the dangling bonds, as is schematically shown in Fig. 3.5. The dimers are symmetric, since every surface atom has only one surface bond to be coordinated. The bonds are locked into (1×2) surface reconstruction and create a chemically stable surface.

The dangling bonds were saturated by preparing an arsenic-terminated surface through cooling the sample under arsenic flux. After this step, the Si surface was covered by a monolayer of As. Such a surface, when tilted 4° toward [110], shows a (2×1) RHEED pattern [KBN$^+$96]. On the exactly (100)-oriented substrates, the patterns are (2×2), which is a result from a superposition of (1×2) and (2×1) patterns. This can be explained by the absence of a preferable orientation for the dimer formation on an exact (100) surface [KBN$^+$96].

In Fig. 3.5 a RHEED image of an As-passivated surface is shown. The image was taken using a 12 kV electron beam at a substrate temperature of approx. 300 °C. A very pronounced double line reconstruction originates from As surface dimers. The reconstruction becomes stronger as the substrate is cooled, indicating an increase in As coverage.

The atomic-steps rearranged on the Si (100)) surface as a result of the interaction with arsenic [BBS91]. It has been demonstrated that, depending on the time order of exposure to As and the surface temperature, the directions of the As-As dimers can reproducibly be prepared perpendicular or parallel to the step edge.

As-deposited surfaces show a strong dependence on the deposition temperatures and on the As

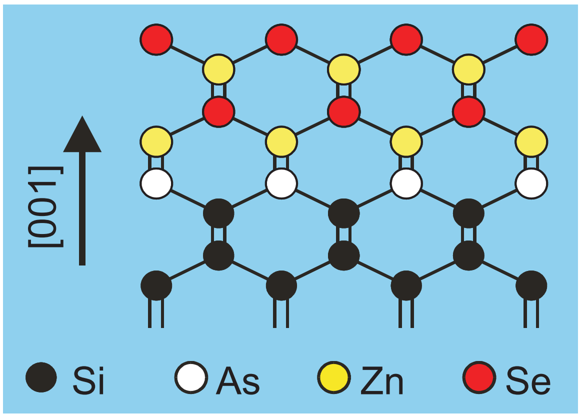

Figure 3.6: *Schematic presentation of stacking sequence at Si (100) - (Zn,Mn)Se interface*

flux during the deposition, while clean, 1° vicinal Si (100) surfaces exhibit a typical double domain that consists of single atomic steps.

As-terminated surface deposited at 500 °C becomes nearly a single domain by the deposition of a half monolayer, and two-dimensional islands appear after more As is deposited [Ide95]. At 600 °C, a one-monolayer As deposition makes the surface nearly a single domain, consisting of double monolayer steps. At 700 °C, a double-domain surface is formed containing triple-atomic steps, where dimer rows in the upper terrace are perpendicular to the step edge.

3.3.2 Si (100)-(Zn,Mn)Se interface

Fig. 3.6 presents a schematic side view of the interface between a Si (100) substrate and a (Zn,Mn)Se epitaxial layer. It is clearly shown that the presence of the As layer on the Si (100) surface increases the separation between silicon and selenium atoms, and in this way, prevents the formation of an amorphous $SiSe_2$ during (Zn,Mn)Se growth [BBS$^+$92]. The layer disturbs the atomic periodicity and makes further epitaxial growth impossible. An attempt to expose the Si (100) surface to a Se flux leads to an instant disappearance of the RHEED patterns, thus indicating an amorphous surface.

The stacking sequence of Si-Si-As-Zn-Se-Zn-Se- in the [100] direction also allows the atoms near the interface to be fully coordinated [BBS$^+$92].

Assuming that the bulk Si and (Zn,Mn)Se materials are fully coordinated, then Zn, Si, and Se atoms contribute 1/2, 1, and 3/2 electrons, respectively, per bond, both in the bulk and at the interface. Without an As interlayer and with the Si-Si-Se-Zn-Se-Zn- stacking sequence, each Se atom at the interface is surrounded by two electrons from the Si layer, one electron from the Zn layer above, and six electrons electrons from itself, a total of nine, or one electron too much for the energetically favorable octet configuration. Alternatively, in the Si-Si-Zn-Se-Zn-Se- case, the interface Zn atom has a total of seven electrons for four bonds, or one too few.

With the interface sequence of Si-Si-As-Zn-Se-Zn-Se-, containing an As interlayer, the As layer has two electrons from the Si layer below, one electron from the Zn layer above, and five electrons from itself, for a total of eight electrons (see Fig. 3.6). The As monolayer therefore allows all bulk and interface atoms to be fully coordinated.

Epitaxial (Zn,Mn)Se films grown on Si (100):As were not tilted relative to the substrate, in contrast to the case of the clean Si (100) substrate, as was mentioned previously. On the other hand, the films do have similar numbers of stacking faults in both possible orientations, allowing microtwin annihilation to take place [BBS$^+$92].

Therefore, arsenic passivation of Si (100) surfaces is absolutely critical for obtaining high-quality epitaxial (Zn,Mn)Se films. The growth start should be initiated by exposure to a group II material, and preferably low temperatures should be used to decrease interdiffusion of Se atoms to the interface.

3.3.3 Growth start and MBE growth

After As passivation and cooling, the samples were transferred to the II-VI growth chamber where the (Zn,Mn)Se films were deposited.

The growth start proved critical for a successful heteroepitaxial growth of (Zn,Mn)Se on As-passivated Si (100) surfaces. The best result was obtained using a low-temperature (240 °C) growth start, consisting of a Zn monolayer deposition, 10 cycles of atomic layer epitaxy (ALE), 5 cycles of migration enhanced epitaxy (MEE), and a standard MBE of (Zn,Mn)Se at 300 °C.

This procedure yielded a good separation of the Si (100) and Se layers and stimulated the relaxation of the epilayer to the lattice constant of bulk (Zn,Mn)Se.

Immediately after the growth start, a three-dimensional (3D) growth mode was observed by RHEED. This 3D growth leads to strong interactions between dislocations and usually yields to a later improvement in structural quality. After the ALE and MEE cycles, the growth mode stabilized and a clear (2×1) RHEED reconstruction could be observed. During the subsequent MBE, stable (2×1) RHEED patterns were observed.

The low-temperature growth start decreased the surface diffusion which is responsible for the 3D islands formation in the early stages of the growth. Limiting the diffusion decreases the height of the islands. This allows for engineering of the properties of the islands, and in this way, affects the relaxation process.

Using a very low (room temperature) epitaxy, it is possible to prevent island formation, but the process leads to an epitaxial quench of the layer because of the strain accumulation after the critical thickness.

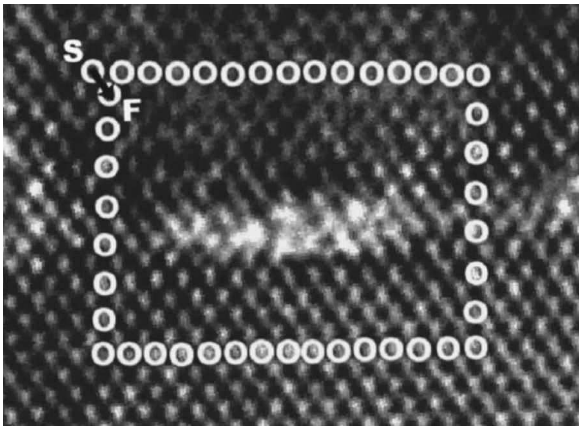

Figure 3.7: *Cross-sectional HRTEM image showing a portion of a Si/Ge heterointerface with two junction pads and a* SiO_2 *patch. (after [LPB*$^+$*05])*

The 3D growth start, combined with a high step density on the vicinal Si (100) surface produces a high interface defect density and stimulates relaxation in this way. The observation of three-dimensional RHEED patterns even, at the early stages of the ALE, supports this assumption.

By proper design of the 3D islands formed at the early growth stages, it is possible to compensate the lattice mismatch without producing a high defect density in the rest of the epitaxial layers.

A higher 3D island density at the interface may, in fact, lead to an improvement in quality of the epilayers grown on such an interface. The epilayer quality is improved due to the strong defect interaction at the interface.

In the early studies of growth on nanopatterned substrates, it was found that a dislocation-free growth of highly lattice-mismatched materials (like Si and Ge) could be engineered [LS86]. Since the growth was initiated on discrete seed pads, the strain relaxation in the epitaxial layer lead to a local order deformation at the interface between the pads, but otherwise the growth was dislocation-free. This result can be generalized to growth on any structured surface.

In this context, it must be mentioned that in the case of (Zn,Mn)Se, a very precise control over material fluxes, the substrate temperatures and the deposition sequence must be maintained. As to the Si substrate, particularities of the As passivation and the surface roughness can strongly influence growth conditions. Taking into account the given factors, the results obtained can be more correctly labeled as a strong defect density reduction rather than a complete annihilation.

To illustrate the process of strain relaxation, a cross-sectional high-resolution transmission electron image of the Si/Ge heterointerface (Fig. 3.7) will be examined. On the image atomic-level details of two Ge junction pads, which are separated by a SiO_2 patch, can be observed. The white circles represent positions of the atoms in the crystal, which are arranged in a Burgers circuit.

The SiO_2 patch gives rise to a Burger's vector of $a/2$ [210] and works as an artificial 60° dislocation. The dislocations form an edge dislocation network. As a result of strong dislocation interaction, strain at the Si/Ge interface is significantly reduced [LPB$^+$05].

Since the lattice mismatch between Si and Ge is very similar to that of Si and (Zn,Mn)Se, it seems logical to assume that the results are well applicable to this material system, as well. We must, however, take into account that in the use of Si and Ge both materials are elementary semiconductors.

In fact, the strain relaxation process has been recently demonstrated to take place in a similar system of the GaAs/Si (100) interface. Vanamu et. al. used $Ge/Si_{1-x}Ge_x$ on nanostructured silicon substrates to evoke the growth of high-quality GaAs epilayers [VDDZ06].

Further experiments may be able to show the extent to which presented theory is applicable to (Zn,Mn)Se DMS grown on Si (100) substrates. Currently, only indirect indications of the process can be provided.

The MEE was done under constant Se flux and alternating Zn and Mn supply. During the process, the substrate temperature was continuously elevated to the standard MBE growth temperature of 300 °C. During the substrate temperature increase, a constant output power was used, and at the end of the MEE growth, the substrate temperature was stabilized under Se flux.

During MEE, the islands were uniformly covered with (Zn,Mn)Se. The defects created during 3D growth started to penetrate in perpendicular directions. At the point where the two defect planes crossed we assume that one or both of the defects annihilated each other because of a local interaction. This process contributed to the improvement in the crystalline quality.

Since electrical measurements were intended to be performed on the structures, the samples were n-type doped during the entire growth process. For the doping, a solid source ZnI_2 cell was used. The flux was adjusted to produce doping in pure ZnSe in excess of 1×10^{19} cm^{-3}.

The interface region is the most critical transport point because of both, the high defect density and the heterointerface band offset. Therefore, the ZnI_2 cell shutter was open every time the Zn shutter was open, including the early growth stages. Such a procedure is still unlikely to produce reliable doping at the early stages of the epitaxial growth, but it may be sufficient for the carrier transport to occur.

The MBE growth was started on the Se-rich surface by opening Zn, Mn and ZnI_2 shutters simultaneously. The growth was done at a standard II-VI flux ratio of about 3.5. During the first few minutes of the growth, the RHEED patterns improved significantly.

Fig. 3.8 presents a RHEED image of a 150 nm (Zn,Mn)Se layer containing 8% Mn grown on an As-passivated Si (100) surface. The image shows a clear two-pattern, where the more intense lines are separated by less intense ones. The lines with higher intensity exhibit intensity patterns placed on the intersection with Kikuchi lines, even though the latter are barely observed. In the

Figure 3.8: *RHEED image of a 150 nm (Zn,Mn)Se layer containing 8% Mn on Si (100) showing (2×1) reconstruction.*

middle, a specular spot is shown. The patterns can be compared with those of high quality (Zn,Mn)Se layers grown on GaAs.

The image is a part of a (2×1) RHEED reconstruction. Another part of the reconstruction is observed when the sample is rotated 45°. As was mentioned before, the (2×1) RHEED reconstruction can be seen when the growth is performed on tilted substrates only. The epilayers grown on exactly [001]-oriented Si (100) substrates exhibit a (2×2) RHEED reconstruction. This can be explained by the absence of a preferable orientation for dimer formation on an exact [100]-oriented Si (100) surface [KBN$^+$96].

3.4 (Zn,Mn)Se layer characterization

After the growth had finished, the samples were taken out of the UHV MBE system and unmounted from the molybdenum blocks by melting the indium at 210 °C. Then, the wafers were split into several samples, and surface, crystalline, magnetic and electrical properties of the samples were examined.

3.4.1 Nomarski differential interference contrast microscopy

The easiest way to access surface properties of the (Zn,Mn)Se epilayers is by optical microscopy. This characterization technique does not require special measurement conditions, is not destructive for the sample and does not need extensive sample preparation.

Nomarski Differential Interference Contrast (NDIC) microscopy is an interference technique and, as such, is not diffraction-limited (i.e., wavelength) except in plane view. An NDIC "photograph" may have a resolution of less than 0.5 micrometers in the plane (x-y) view (as in a normal photomicrograph). However, in the z-direction (height), the resolution is much higher, because it is only limited by the method used to resolve the phase difference of the interference fringes [DHR77].

In this study a Nikon Eclipse ME600 microscope equipped with polarization setup for NDIC configuration imaging, was used. The microscope was- connected to a high-resolution digital camera, and objectives of 2.5x to 100x magnification were available.

Fig. 3.9(a) presents a polarization interference contrast microscopy image of a 200 nm (Zn,Mn)Se layer containing 4% Mn on a Si surface oriented exactly along (100). A slight surface roughness can be observed.

The surface morphology is very homogenous over the entire sample and exhibits no extended defects. The growth conditions are very predictable and can be reproduced for multiple samples, leading to similar surface patterns.

When a nominally identical surface is viewed under higher magnification using a scanning electron microscope, as in Fig. 3.9(b), a wavy surface structure emerges.

This probably originates from the 3D growth start in combination with the lattice mismatch between the epilayer and the substrate. The mismatch leads to strain relaxation by local elastic deformation of the epilayer.

3.4.2 HRXRD analysis of (Zn,Mn)Se layers

A typical High Resolution X-Ray Diffraction (HRXRD) scan of a 200 nm (Zn,Mn)Se layer containing 4% Mn is shown in Fig. 3.10. The right peak corresponds to the silicon substrate and the left peak to the (Zn,Mn)Se layer. The lattice mismatch of 0.23 Å extracted using Bragg's law from the 1.66 degree difference in peak positions, agrees well with the lattice mismatch expected for a fully relaxed (Zn,Mn)Se layer containing 4% Mn on Si (100). An ω scan of the (Zn,Mn)Se peak yields a full width at half maximum of about 700 arcseconds, indicating an epilayer of reasonably good crystalline quality.

A reciprocal space map of a 200 nm (Zn,Mn)Se layer containing 4% Mn on Si (100) taken with a (115) asymmetric reflection is shown in Fig. 3.11. The Si (100) substrate peak is located at the top right corner of the map and the (Zn,Mn)Se layer is placed at bottom left. Multiple intensity maximums on the substrate peak can be attributed to slight deviations in the substrate alignment.

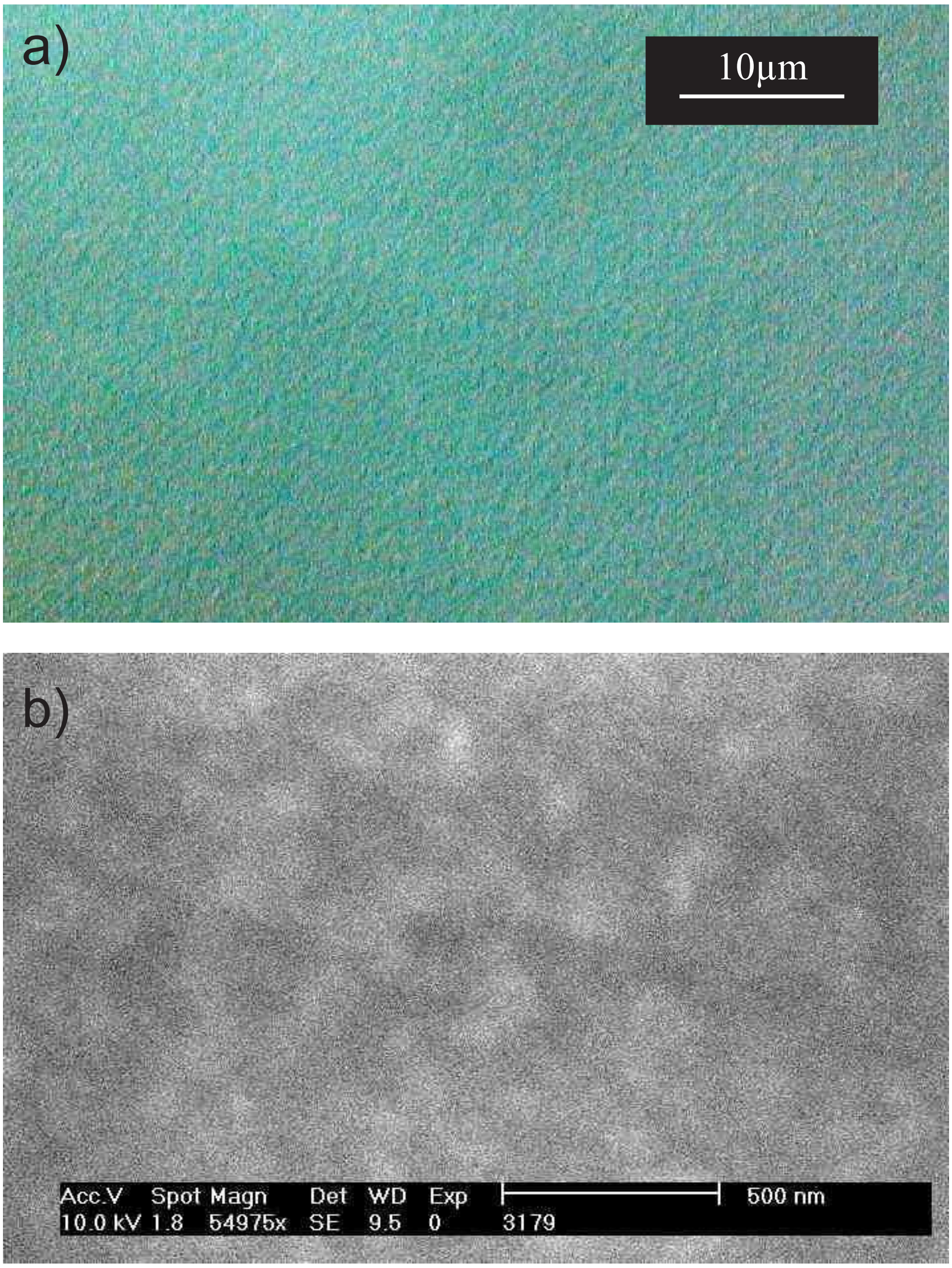

Figure 3.9: *(a) Polarization differential interference contrast microscopy image indicating roughness of the epitaxial surface of a (Zn,Mn)Se layer containing 4% Mn. (b) Scanning electron microscope micrograph of the surface of a nominally identical sample.*

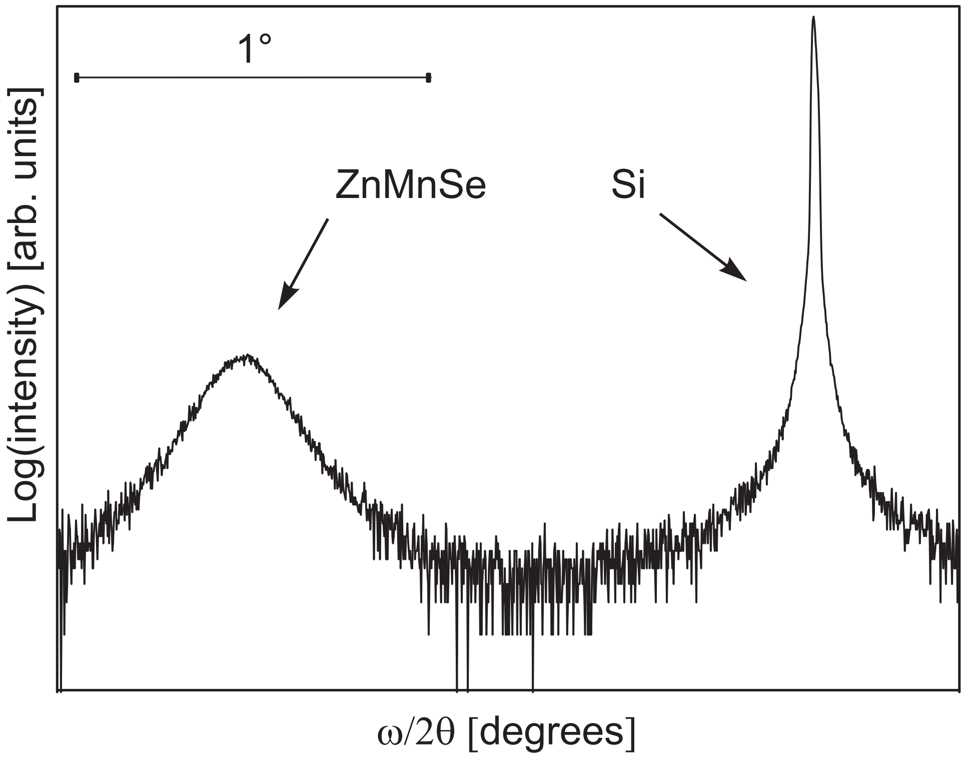

Figure 3.10: *$\omega/2\theta$ scan of a 200 nm (Zn,Mn)Se layer containing 4% Mn taken with a (004) reflex.*

From the scan, it can be observed that the layer is relaxed and that the relaxation takes place at thicknesses below the HRXRD setup resolution. Since layers as thick as 30 nanometers can be measured with the present setup, the conclusion was drawn that the relaxation takes place below this thickness. Combined with the observation of 3D growth start by RHEED, this finding leads to a fair description of the relaxation process as an elastic deformation due to defect interaction during the initial stages of the atomic layer epitaxy and migration enhanced epitaxy. Elliptical shape of the epilayer peak is the further indication of elastic strain.

3.4.3 Layer relaxation

Even though most of the strain related to the lattice mismatch between Si (100) and (Zn,Mn)Se has relaxed close to the interface, there is still a certain amount of strain that deforms the epitaxial layer. The strain can be attributed mainly to the elastic deformation of the epilayer.

Strain in the lattice, induced by elastic deformation, is known to affect properties of epitaxial films. The strain in the valance band in (Zn,Mn)Se epilayers leads to a magnetoanisotropy (in Voigt geometry) and reversal of the light-hole exciton component sequence (in Faraday geometry) [YTF$^+$95].

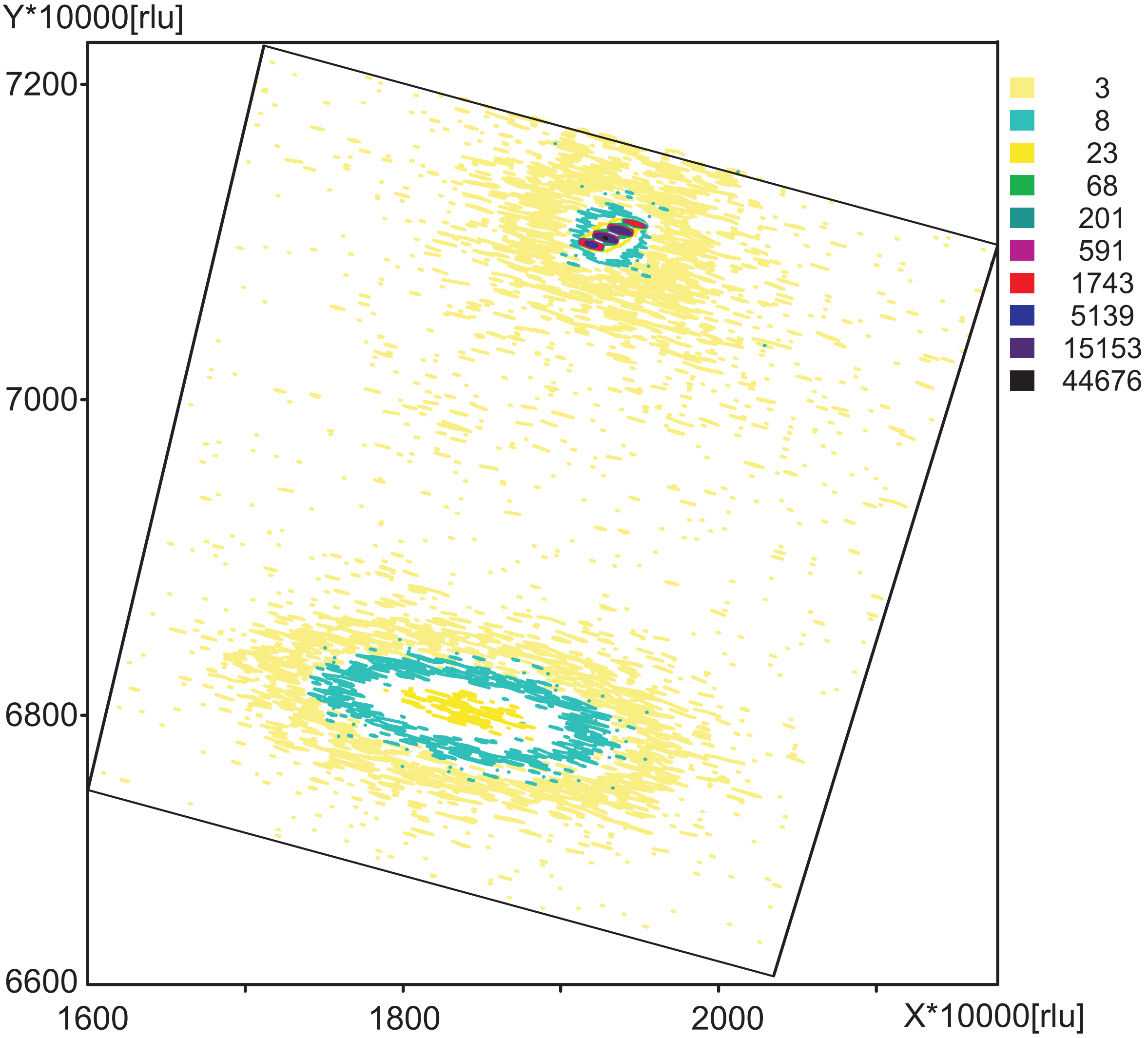

Figure 3.11: *Reciprocal space map of a 200 nm (Zn,Mn)Se layer containing 4% Mn taken with a (115) asymmetric reflection.*

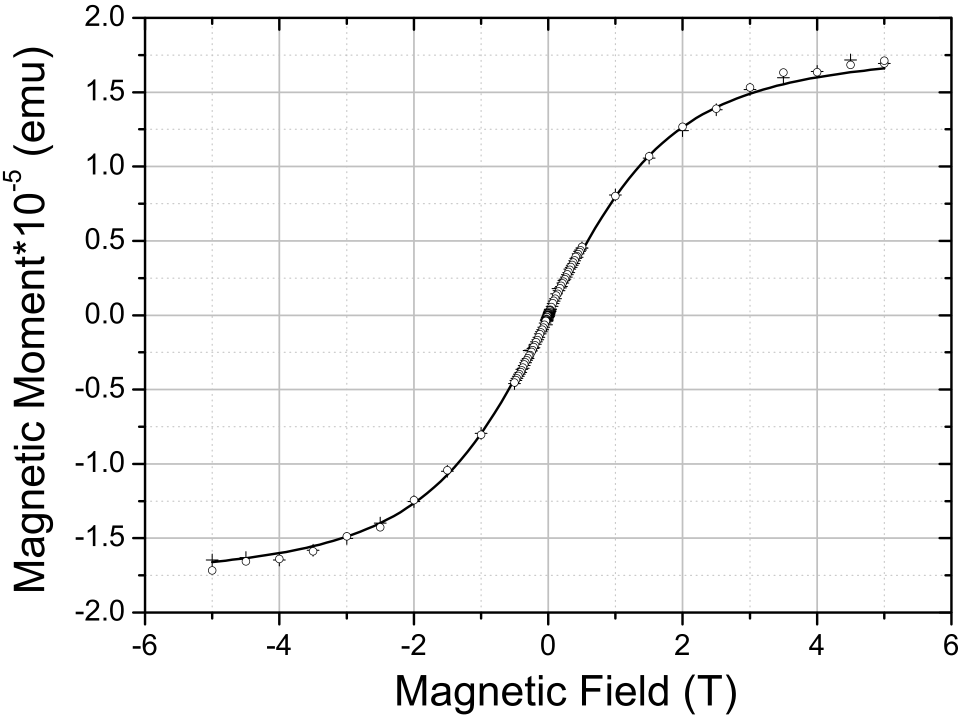

Figure 3.12: *Magnetic moment of a 200 nm thick (Zn,Mn)Se epilayer with 4% Mn as a function of an external magnetic field as determined by SQUID magnetometry.*

In addition to elastic strain relaxation, accompanying high defect density is hard to avoid. Moreover, the transmission electron microscopy studies on (Zn,Mn)Se/GaAs heterointerface indicate a strong influence of high Mn-content on the dislocation density [LGD$^+$06]. Namely, the introduction of 14% Mn ions into the ZnSe compound increases the defect density by several orders of magnitude as compared to pure ZnSe. A high stacking fault defect density ($\sim 10^9$ cm^{-2}) in [111] planes is observed.

The dopability decreases continuously with increasing Mn content in (Zn,Mn)Se layers [DALS$^+$05]. The Hall mobility decreases and the resistivity increases as a function of Mn incorporation due to the increasing scattering rates and the decreasing carrier concentration. A lower electron effective mass in manganese-containing samples, compared to ZnSe, is deduced from optical measurements [DALS$^+$05].

3.4.4 SQUID measurements

The magnetic properties of a 200 nm thick (Zn,Mn)Se epilayer with 4% nominal Mn concentration and a volume of about 100 μm^3 are characterized in a Quantum Design SQUID magnetometer. A 1.8 K hysteresis loop of magnetization is presented in Fig. 3.12. The open circles and crosses represent the experimental data. No hysteretic behavior is observed down to the lowest resolution of the SQUID as expected.

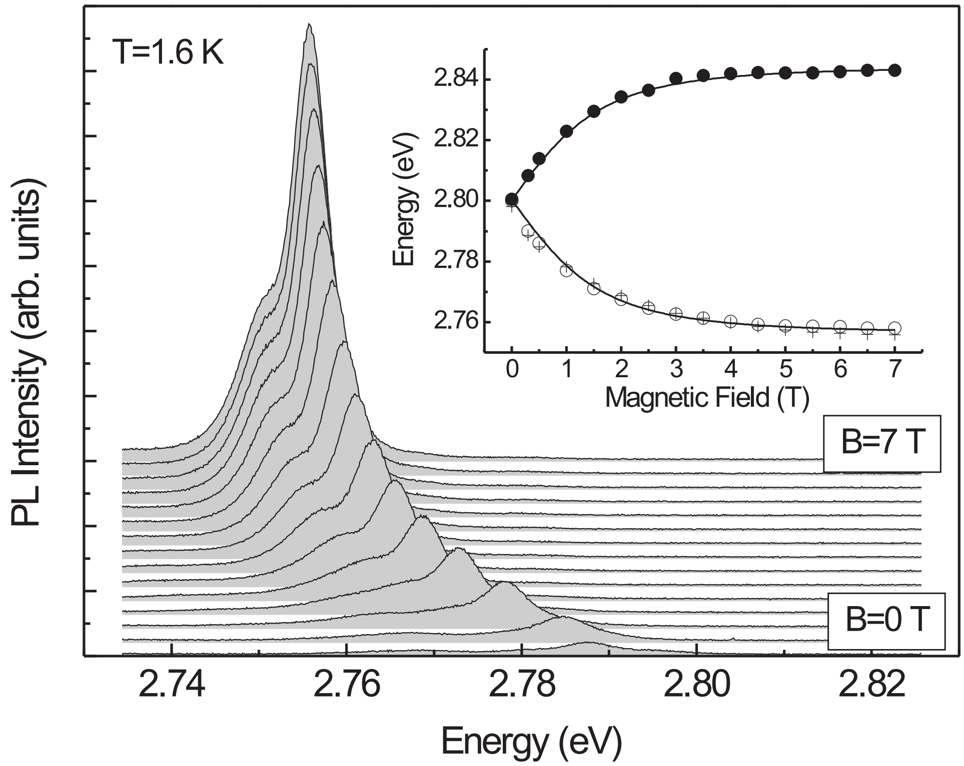

Figure 3.13: *Photoluminescence spectra of a 1000 nm thick (Zn,Mn)Se layer containing 2% Mn on Si(100) at various magnetic fields, detected in σ^+ - polarization. The energy dependence of the free exciton peak versus magnetic field is shown in the inset (crosses). Closed and open circles are reflectivity data for σ^+ - and σ^- - polarized light, respectively.*

The data is fitted well by the solid line in the figure, which corresponds to a modified Brillouin function [GPF79] that is known to describe the functional dependence of the magnetization on field in (Zn,Mn)Se. This allows the extraction of an effective temperature parameter T_e [GPF79] of 1.45 K, which indicates [YTF$^+$95] a Mn concentration of about 4%. The saturation magnetization is 0.2 Bohr magnetons per unit cell. Using the effective Mn spin for the interacting Mn system of (Zn,Mn)Se from Ref. [YTF$^+$95], this corresponds to a Mn concentration of about 3.5%. Given the fairly large uncertainty in the determination of the volume of the sample, these numbers are considered to be in fair agreement. The magnetic data is therefore entirely consistent with the incorporation of about 4% of Mn into the ZnSe lattice.

3.4.5 Magneto optical measurements

The optical quality of a 1000 nm thick (Zn,Mn)Se layer containing 2% Mn is examined by photoluminescence and reflectivity measurements in a magneto-optical cryostat at 1.6 K. Fig. 3.13 shows σ^+ - polarized luminescence spectra of the structure for magnetic fields from 0 to 7 T. Due to the large Zeeman splitting of the carriers, σ^- - polarized luminescence is completely suppressed already at a very small field of about 0.3 T. At B=0, the luminescence spectrum is dominated by a donor-bound exciton line.

With the magnetic field applied, the giant Zeeman splitting results in a suppression of the bound exciton and thus in a gain of intensity of the free exciton line. The energy position of the free exciton is depicted by crosses in the inset of Fig. 3.13. The open and closed circles in this figure represent reflectivity data, detected for σ^+ - and σ^- - polarized light, respectively. The Mn concentration of the epilayer can be deduced by fitting the experimental value of the Zeeman splitting with a modified Brillouin function again [KYK$^+$02].

The result of the fitting procedure is indicated by lines in the inset of Fig. 3.13. The obtained value of 3% for the Mn concentration is in good agreement with the growth parameters and the magnetization measurements, and it indicates a good incorporation of the Mn into the host material.

Since the magneto-optical measurements are very sensitive to material quality, conclusion based on the shape and intensity of the photoluminescence signal can be drawn such that the quality of the paramagnetic epitaxial layers is comparable to the quality of layers grown on GaAs, however, relatively thick samples are needed.

Therefore, the high-quality growth of paramagnetic (Zn,Mn)Se epilayers on a Si (100) surface has been demonstrated. The growth technique and surface preparation procedure are optimized by using As-passivation and a sophisticated low-temperature growth start. Magneto-optical and magnetic characterizations demonstrate that the quality of the epilayers may be suitable for spin-injection experiments.

3.5 Electrical properties of Si (100)-(Zn,Mn)Se interface

3.5.1 Band offset

Theoretical calculations using an effective dipole theory for band lineups in semiconductor heterojunctions predict the value of the band offset to be 1.17 eV [RC87]. The value is in very good agreement with previous experimental results [KM83].

Due to the high lattice mismatch between a (Zn,Mn)Se epitaxial layer and Si (100) substrate, considerable strain is created at the interface. The strain leads to a significant change in the valence band offset between the two semiconductors [dWM86].

The absolute value of the interface strain depends on the lattice mismatch. A change in Mn concentration in the (Zn,Mn)Se compound leads to a change in its lattice constant. The lattice mismatch therefore is dependant on the Mn content of the epitaxial layers.

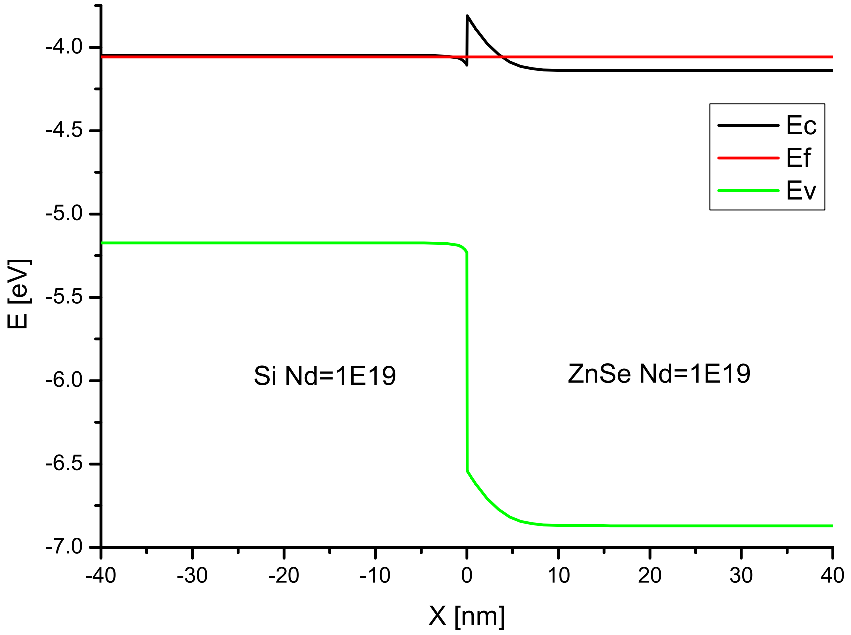

Figure 3.14: *Calculated band diagram for Si(n-2e19)-ZnSe(n-1e19) at 0.0V applied bias.*

Details of strain relaxation at the early growth stages determine the magnitude of the effect, as well. Using ultaviolet- and X-ray-photoemission, as well as low-energy electron-diffraction during room-temperature growth of the Si/ZnSe(100) heterojunction, the valence band offset was found to be 1.65±0.1 eV, and the Fermi-level-pinning position was 1.85±0.1 eV above the valence-band maximum of ZnSe [XVS+88].

The discrepancy in the values of the experimental valence band offset observed by different authors may be explained by the difference in strain relaxation details at the interface. In this experiment, the complete values are more complex because of the presence of Mn magnetic ions in the crystal.

Fig. 3.14 presents a calculated band diagram for Si(n-2e19)-ZnSe(n-1e19) at 0.0V applied bias. The value of the valence band offset of 1.23 is the most accepted value in the literature. Doping values in the ZnSe layer and in the Si (100) substrate are chosen to reflect the most common experimental conditions.

A Schottky diode is formed at the heterointerface. Absolute parameters of the diode depend on the details of the interface. Strain, defects, doping, Mn content and crystallinity of the epilayer, as well as the interface electric field, change the electrical profile at the interface (see Section 1.3). This text is limited to a qualitative description of the heterojunction, since it is difficult to account for all the details of a particular interface.

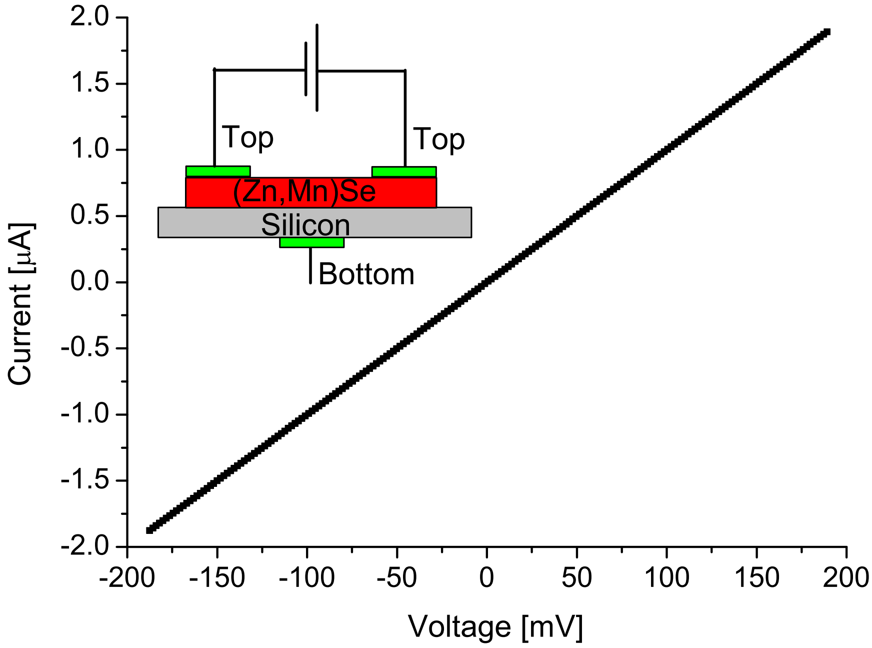

Figure 3.15: *Room temperature I-V characteristics of a 600 nm (Zn,Mn)Se layer containing 8% Mn. The current is flowing between the two top contacts.*

In the Schottky diode, the electric field directed from ZnSe into Si (100) produces no current as the diode is closed, and an increase in voltage leads to an extension of the depletion region. When the field is applied in the opposite direction, no current flows until an activation energy is reached. The energy is proportional to the conduction band offset and, therefore, the height of the tunnel barrier.

As soon as electric field exceeds the activation energy, the current starts to flow. The slope of the linear part of the I-V characteristic is defined by the sum of the internal resistance of the device and the resistance of the rest of the circuit. Hence, by measuring the resistance, the serial resistance of the device may be estimated.

3.5.2 I-V characteristics

(Zn,Mn)Se samples n-type doped with Iodine were processed into stripe structures and measured in a ^{4}He cryostat. In-situ metallization of the layers decrease the contact resistance. Quasi 4 probe measurements had been applied due to a relatively large area of the contact pads.

Fig. 3.15 shows a room-temperature I-V characteristic of a 600 nm (Zn,Mn)Se layer containing 8% Mn. The measurement layout is shown in the insert. The top contacts are placed on the (Zn,Mn)Se layer, and the bottom contact is placed on the back side of the highly doped Si substrate. The (Zn,Mn)Se layer is nominally doped to $\sim 8 \times 10^{18}$ with Iodine. 100 kOhm resistance, extracted from the slope of the curve, leads to a room-temperature resistivity of

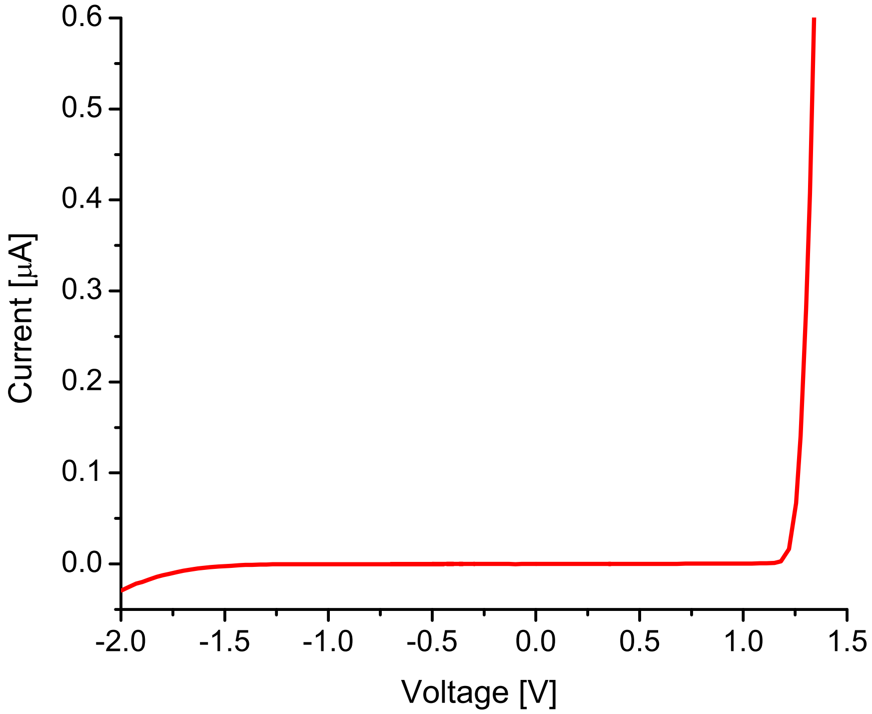

Figure 3.16: *Room temperature I-V characteristics of a 600 nm (Zn,Mn)Se layer containing 8% Mn measured from the (Zn,Mn)Se layer to the Si substrate.*

approx. 9×10^{-2} ohm-meters for the layer.

When the distance between the contact pads is increased, the resistance increases proportionally. This indicates that the current probably flows through the layer and not through the highly conductive substrate. The reason for this might be the Schottky barrier, as was discussed in the previous Section.

When the same sample is measured in the top to bottom configuration, meaning from the top of the epitaxial layer, through the interface, to the substrate (see insert in Fig. 3.15), the I-V characteristics presented in Fig. 3.16 is observed. The characteristic is typical for a Schottky diode. At voltages higher than approx. 1.25 V, a significant increase in the current is observed. This increase is linear, and the slope of the curve is determined by the serial resistance of the device.

The built-in voltage of approx. 1.3 V is extracted by extrapolating the linear part of the I-V characteristics. 125 kOhm resistance of the linear part is the sum of the epitaxial layer, the interface, and the contact resistances. The negative side of the I-V characteristic shows an increase in the current after approx. -1.5 V which is most likely attributed to an imperfection of the diode.

The temperature stability of the junction is important for the experimental observation of the electrical spin injection from (Zn,Mn)Se into Si (100). Since the giant Zeeman splitting is

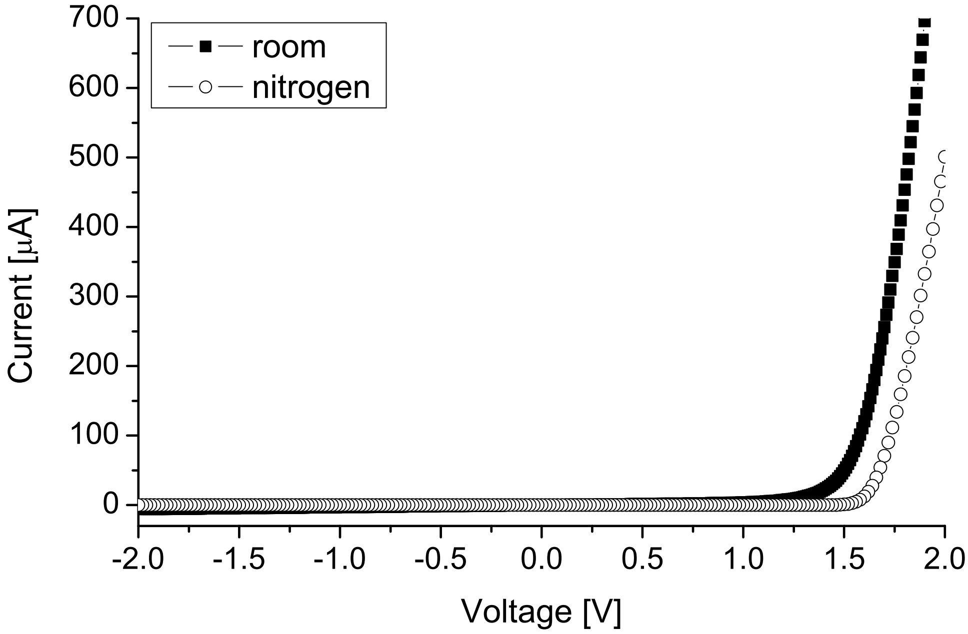

Figure 3.17: *Temperature dependence of the I-V characteristics of a 250 nm (Zn,Mn)Se layer containing 4% Mn measured from the top of (Zn,Mn)Se layer to the bottom of the Si substrate.*

strongly temperature dependant, it is desired to decrease the sample temperature to Helium temperatures.

Fig. 3.17 shows the I-V characteristics of a 250 nm (Zn,Mn)Se layer containing 4% Mn measured in the top-to-bottom configuration. The layer is nominally doped to 8×10^{18}. The data taken at room temperature is represented by the squares, and the data taken at the liquid nitrogen temperature is represented by the circles.

By extrapolating the linear part of the I-V characteristics, approx. 1.6 V built-in voltage may be extracted. The voltage does not exhibit a strong temperature dependence. The 432 Ohm resistance at room temperature, which increases to 635 Ohm at nitrogen temperature, is extracted from the slope of the linear part.

Since the aim is spin injection from DMS into NMS, one of the central questions is the influence of the high defect density at the interface on spin injection efficiency. Precisely this question was investigated by Stroud and Jonker [SHP$^+$02]. The authors found no strong effect of defects on the spin injection efficiency.

So there is some hope that, although the dislocations density is considerably higher that in experiments by Jonker, spin injection from (Zn,Mn)Se into Si may be possible.

Summary

In pursuit of a novel generation of devices, exploration of spin properties of the particles is needed. Spintronics is a modern field in physics which exploits spin properties to be used in addition to the charge degree of freedom.

Since the conductivity mismatch problem presents a fundamental obstacle for electrical spin injection from a ferromagnetic metal into a diffusive semiconductor [SFM$^+$00], other means for injecting spin-polarized carriers must be used. With a tunnel contact, it is possible to achieve a highly spin-polarized room-temperature tunnel injection [JWS$^+$05]. We used a novel approach and applied magnetic RTDs for spin manipulation.

In this work, properties of all-II-VI magnetic resonant tunneling diodes (RTDs), as applied to spintronics, were reported. Growth conditions were optimized to increase the peak-to-valley ratio, and the design of the RTDs was optimized for observation of spin related transport effects. When an external magnetic field was applied, spin manipulation became possible. Self-organized CdSe quantum structures were grown and investigated using optical means. After embedding them into a (Zn,Be)Se tunneling barrier, the properties were assessed by the resonant tunneling.

A screening buffer consisting of a 5-period (Zn,Be)Se/ZnSe superlattice was developed and applied to avoid the negative influence of the interface charge depletion on the transport structures. On the surfaces prepared this way, the RTDs were grown and optimized.

By incorporating a (Zn,Be)Se layer in the injector of the RTDs the important role of the charge accumulation in the tunneling processes in this part of the device could be demonstrated. Using a (Zn,Mn)Se layer as injector, it could be shown that the injector band profile strongly influences the I-V characteristics of RTDs, and the collector band profile was shown to have no strong influence on the characteristics because it is located below the energy of the tunneling carriers.

Spin filtering in magnetic RTDs was achieved by placing a magnetic (Zn,Mn)Se layer in the quantum well of the RTDs. When an external magnetic field was applied, resonant levels in the quantum well were split as a result of the giant Zeeman Splitting in the diluted magnetic semiconductor (DMS).

To simulate I-V characteristics of the RTDs at different magnetic fields, a model based on the giant Zeeman splitting of the spin degenerate sublevels was developed and applied [SGS+03].

Analysis of the strain accumulation in the structure showed the crucial role of the quantum well in compensating the strain collected in the barriers. In the absence of the quantum well, the barriers are expected to relax, producing multiple defects. Analysis of the HRXRD data obtained on the structures showed no relaxation in the RTDs.

Changes in the width of the quantum well, as well as in the height of the barriers, lead to changes in transport characteristics of a magnetic RTD as expected and similar to ones observed in the nonmagnetic structures. A decrease in the width of the well leads to a strong increase in the nonresonant current. A decrease in the height of the barriers leads to a similar effect.

Magneto-transport investigations showed that magnetic impurities in RTDs are not only a powerful tool for the investigation of spin-related phenomena, but also provide a new mechanism for investigation of the influence of the band profile and charge accumulation on the structures. The splitting of the spin-degenerate sub-bands in an external magnetic field provides a very detailed insight into resonant tunneling processes.

Extending RTD structures to double quantum well triple barrier RTDs, gives an unprecedented flexibility to the devices. The internal structure of a double quantum well device can by altered, leading to a change in the coupling strength between the quantum wells. The device exhibits an enhanced magnetic field dependence, which is explained using the giant Zeeman splitting.

Using lattice mismatch between two semiconductors, self-organized CdSe quantum dots were prepared in a ZnSe matrix. Because the morphology of the surface on which CdSe quantum dots are grown plays an important role in defining the properties of the dots, by changing the growth conditions, CdSe quantum dots may be grown strongly anisotropic.

The low symmetry of the dots naturally induces quantum interference between linearly and circularly polarized photon states. The interference leads to circular-to-linear and linear-to-circular conversions of optical polarization by semiconductor quantum dots [AKP+06]. Since the anisotropy in the quantum dots is created during epitaxial growth, it requires no magnetic atoms. The polarization conversion occurs in CdSe quantum dots under continuous wave excitation in the absence of the magnetic field.

When such self-organized quantum dots are placed between (Zn,Be,Mn)Se barriers in a magnetic RTD, an interaction between the magnetic atoms in the vicinity of the dots and the electron wave function is triggered by tunneling carriers [GSS+06]. This interaction was investigated by means of magnetotunneling spectroscopy (see Section 2.4.3).

When an external magnetic field is applied, the spin degenerate sublevels in the quantum dots split and the splitting follows the Brillouin function in most of the range, as is expected from the giant Zeeman caused by magnetic ions. However, the splitting persists down to a zero magnetic field. Theoretical calculations support the idea and suggest that the presence of a single electron in the quantum dot can mediate ferromagnetic interaction between Mn ions in the vicinity.

The discussed quantum dots and the resonant tunneling devices are all realized in the II-VI material system. While II-VI DMS's are already proven as efficient spin injectors [FKR$^+$99], these compound semiconductors are by no means the optimal nonmagnetic semiconductor materials for spin injection experiments because of their limited spin lifetime. Hence, is desirable to inject spin-polarized carriers into a material with much longer spin lifetimes.

Silicon, due to its higher crystalline symmetry can preserve spin-polarization of free carriers for a very long time [FG59, TLAR03]. It is used in modern microelectronics and, therefore, presents an important target for spintronics.

Due to Si (100) surface reactivity, a hydrogen passivation was used to protect the surface during the ex-situ processing. After desorbing the passivation in the UHV system, an As-passivated surface was prepared by cooling the sample under an As flux. The passivation was an essential step in coordinating the dangling bonds at the (Zn,Mn)Se/Si (100) interface. It was essential in preventing the formation of amorphous $SiSe_2$ [BBS$^+$92] during sequential (Zn,Mn)Se growth.

Since the growth start proved critical during heteroepitaxial growth of (Zn,Mn)Se on the As-passivated Si (100) surfaces, a low temperature growth start was used, followed by a standard molecular beam epitaxy of (Zn,Mn)Se [SRF$^+$04].

Three-dimensional growth was observed in the initial phases of the heteroepitaxy. The growth start produced a high defect density and stimulated the layer relaxation by defect interactions. It has been demonstrated that a completely defect-free growth may be conducted even for high lattice-mismatched layers on patterned surfaces [LPB$^+$05]. Hence, by optimizing the growth start, it is possible to strongly improve the quality of the epitaxial layers.

Photoluminescence and reflectivity measurements of the epilayers were performed in a magneto-optical cryostat at 1.6 K. The Mn concentration of the epilayers was deduced by fitting the experimental values of the giant Zeeman splitting with a modified Brillouin function. The obtained value for the Mn concentration indicates a good incorporation of Mn into the host material.

The magnetic properties of the (Zn,Mn)Se epilayers were characterized in a Quantum Design superconducting quantum interference device (SQUID) magnetometer. No hysteretic behavior was observed down to the lowest resolution of the SQUID.

The data were well-fitted with a modified Brillouin function that is known to describe the functional dependence of the magnetization on the field in (Zn,Mn)Se. From the fit, an effective temperature parameter Te [GPF79], which indicates the Mn concentration was extracted. The magnetic data were entirely consistent with good incorporation of Mn into the ZnSe lattice.

Electrical measurements of highly-doped (Zn,Mn)Se layers and the (Zn,Mn)Se/Si (100) interface were performed at different temperatures. The layers showed linear transport characteristics, even though the contacting of the layers proved to be difficult, even with in-situ techniques. Despite the strong Schottky diode behavior observed on the interface, spin-polarized transport may be possible.

Zusammenfassung

Für zukünftige Technologien ist die Erforschung von der verwendeten Teilchen nötig. Spintronik ist ein modernes Gebiet der Physik, welches neben der Ladung auch die Spineigenschaften als zusätzlichen Freiheitsgrad nutzbar macht.

Der "conductivity mismatch" stellt ein fundamentales Problem für elektrische Spininjektion aus einem ferromagnetischem Metal in einen diffusiven Halbleiter dar [SFM$^+$00]. Daher müssen andere Methoden für die Injektion spin-polarisierter Ladungsträger benutzt werden. Mit einem Tunnelkontakt ist es möglich, eine hoch spin-polarisierte, Raumtemperatur Tunnel-Injektion zu erzielen [JWS$^+$05]. Wir benutzten einen neuen Ansatz und verwendeten magnetische RTDs zur Spinmanipulation.

In dieser Arbeit wurden die Eigenschaften von magnetischen, resonanten Tunneldioden (RTDs) aus rheinen II-VI-Halbleitern in ihrer Verwendung für die Spintronik beschrieben. Wachstumsbedingungen wurden optimiert, um das Peak-to-Valley-Verhältnis zu vergrößern. Das Design der RTDs wurde optimiert, um spinbezogene Transporteffekte beobachten zu könen. Mit einem externen Magnetfeld war Spinmanipulation möglich. Selbstorganisierte CdSe Quanten-Strukturen wurden hergestelt und mit optischen Techniken untersucht. Sie würden in (Zn,Be)Se Tunnelbarrieren eingebettet, so dass ihre Eigenschaften durch resonantes Tunneln zugänglich wurden.

Ein abschirmender Puffer, bestehend aus einem 5-periodischem (Zn,Be)Se/ZnSe Übergitter, wurde entwickelt und genutzt, um negative Einflüsse der Ladungsverarmung an der Grenzfläche zum Substrat die Transportstrukturen zu vermeiden. Auf einer so vorbereiteten Oberfläche wurden die RTDs gewachsen und optimiert.

Durch den Einbau einer (Zn,Be)Se Schicht im Injektor der RTDs konnte die wichtige Rolle der Ladungsakkumulation beim Tunnelprozess in diesem Teil der Struktur gezeigt werden. Mit einer (Zn,Mn)Se Schicht als Injektor konnte gezeigt werden, dass das Injektor-Bandprofil stark die I-V Charakteristik der RTDs beeinflußt und das Kollektor-Bandprofil keinen starken Einfluß auf die Charakteristik hat, weil es sich unterhalb der Energie der tunnelnden Ladungsträger befindet.

Spinfilterung in magnetischen RTDs wurde durch eine magnetische (Zn,Mn)Se Schicht im

Quantentrog der RTDs erreicht. Wenn ein externes magnetisches Feld angelegt wurde, wurden die resonanten Niveaus im Quantentrog aufgrund des Giant-Zeeman Effekts im semimagnetischen Halbleiter (DMS) aufgespalten.

Zur Simulation der I-V Charakteristik der RTDs bei verschiedenen magnetischen Feldern wurde ein Modell basierend auf der Giant-Zeeman Aufspaltung der spinentarteten Unterniveaus entwickelt und angewandt [SGS+03].

Die Analyse der Verspannungsakkumulation in der Struktur zeigte die entscheidende Rolle des Quantentrogs bei der Kompensation der Verspannung, die von den Barrieren stammt. Ohne Quantentrog wäre von einer Relaxation der Barrieren auszugehen, was viele Defekte zur Folge hätte. Die Analyse der HRXRD Daten dieser Strukturen zeigte keine Relaxation in den RTDs.

Änderungen in der Breite des Quantentrogs oder in der Höhe der Barrieren führen wie erwartet zu Änderungen der Transportcharakteristik der magnetischen RTD und entsprechen denen in nichtmagnetischen Strukturen. Eine Abnahme in der Dicke des Trogs führt zu einer starken Zunahme des nichtresonanten Stroms. Eine Abnahme in der Höhe der Barriere führt zu einem ähnlichen Effekt.

Magneto-transport Untersuchungen zeigten, dass magnetische Verunreinigungen in RTDs nicht nur ein wichtiges Werkzeug zur Untersuchung von Spinphänomenen sind, sondern auch einen neuen Mechanismus zur Untersuchung des Einflusses auf das Bandprofil und die Ladungsakkumulation in den Strukturen hervorbringen. Die Aufspaltung der spinentarteten Subbänder in einem externen magnetischen Feld gibt einen sehr detaillierten Einblick in den Prozess des resonanten Tunnelns.

Eine Erweiterung der RTD Strukturen zu Doppelquantentrog-Dreifachbarrieren-RTDs eröffnet völlig neue Möglichkeiten. Die interne Struktur eines Doppelquantentrogs kann verändert werden, und damit zu einer Veränderung der Kopplungsstärke zwischen den Quantentrögen führen. Damit weist ee eine erhöhte Magnetfeldabhängigkeit auf, welche durch die Giant-Zeeman Auschpaltung erklärt wird.

Unter Ausnutzung der Gitterfehlanpassung zwischen zwei Halbleitern, wurden selbstorganisierte CdSe Quantenpunkte in einer ZnSe Matrix hergestellt. Weil die Morphologie der Oberfläche, auf der die CdSe Quantenpunkte gewachsen werden, eine wichtige Rolle in der Definition der Eigenschaften der Punkte spielt, können CdSe Quantenpunkte stark anisotrop abgeschieden werden, wenn man die Wachstumsbedingungen entsprechend anpasst.

Die niedrige Symmetrie der Punkte induziert naturgemäß Quanteninterferenz zwischen linearen und zirkular polarisierten Photonzuständen. Die Interferenz führt zu zirkular-zu-linear und linear-zu-zirkular Konversionen der optischen Polarisation durch Halbleiter Quantenpunkte [AKP+06]. Da die Anisotropie in den Quantenpunkten während des epitaktischen Wachstums erzeugt wird, benötigt es keine magnetischen Atome. Die Polarisationskonversion findet in den CdSe Quantenpunkten bei kontinuierlicher Erregung ohne Magnetfeld statt.

Wenn solche selbstorganisierten Quantenpunkte zwischen (Zn,Be,Mn)Se Barrieren in einer magnetischen RTD platziert werden, wird eine magnetische Wechselwirkung zwischen den magnetischen Atomen in der Nachbarschaft der Punkte und der Punktwellenfunktion durch Tunnelladungsträger ausgelöst [GSS$^+$06]. Diese Wechselwirkung wurde mittels Magnetotunnel-Spektroskopie untersucht. (see Section 2.4.3).

Sobald ein magnetisch Feld anliegt, spalten sich die spinentarteten Subniveaus in den Quantenpunkten auf und die Aufspaltung folgt der Brillouinfunktion für nahezu den gesamten Messbereich, wie es von einer Giant-Zeeman Aufspaltung durch magnetische Ionen erwartet wird. Allerdings verbleibt eine Aufspaltung auch ohne magnetisches Feld. Theoretische Berechnungen unterstützen die Idee, dass die Existenz eines einzelnen Elektrons in dem Quantenpunkt eine ferromagnetische Wechselwirkung zwischen Mn-Ionen in der Nachbarschaft vermitteln kann.

Die erwähnten Quantenpunkte und die resonanten Tunnelstrukturen sind alle im II-VI Materialsystem realisiert worden. Während II-VI DMS's effiziente Spininjektoren sein können [FKR$^+$99], sind diese zusammengesetzten Halbleiter wegen ihrer begrenzten Spinlebenszeit keineswegs optimale nichtmagnetische Halbleitermaterialien für die Spininjektion. Daher ist es wünschenswert spinpolarisierten Strom in ein Material mit langer Spinlebenszeit zu injizieren.

Silizium kann wegen seiner höheren kristallinen Symmetry eine Spinpolarisation von freien Ladungsträgern für eine sehr lange Zeit erhalten [FG59, TLAR03]. Es wird in moderner Mikroelektronik verwendet und stellt daher ein wichtiges Ziel für Spintronik dar.

Wegen der Reaktivität der Si (100) Oberfläche wurde diese mit Wasserstoff passiviert, um die Oberfläche während der ex-situ Prozessierung zu schützen. Nach dem Entfernen der Passivierung im UHV-System, wurde eine As-passivierte Oberfläche durch Abkühlen der Probe unter As-Fluss erzeugt. Diese Passivierung war ein wesentlicher Schritt zur Kontrolle der dangling bonds des (Zn,Mn)Se/Si (100) Übergangs. Es war essenziell, um der Entstehung von amorphen $SiSe_2$ [BBS$^+$92] während dem anschließenden (Zn,Mn)Se Wachstum vorzubeugen.

Da sich der Wachstumsstart während des heteroepitaktischen Wachstums von (Zn,Mn)Se auf As-passivierten Si (100) Oberflächen als kritisch erwies, wurde ein Wachstumsstart bei niedrigen Temperaturen benutzt, auf welchen dann die normale Molekular-Strahl-Epitaxie von (Zn,Mn)Se folgte [SRF$^+$04].

Dreidimensionales Wachstum wurde in den Anfangsphasen der Heteroepitaxie beobachtet. Der Wachstumsstart produzierte eine hohe Defektdichte und stimulierte die Schichtrelaxation durch Defektwechselwirkungen. Es wurde gezeigt, dass ein komplett defektfreies Wachstum sogar bei großer Gitterfehlanpassung durch strukturierte Oberflächen herbeigeführt werden kann [LPB$^+$05]. Daher ist es möglich, durch die Optimierung des Wachstumsstarts, die Qualität der epitaktischen Schichten sehr zu verbessern.

Photolumineszenz- und Reflektivitätsmessungen der Schichten wurden in einem magneto-optischen Kryostat bei 1,6 K durchgeführt. Die Mn Konzentration der Schichten wurde durch das Anpassen der Giant-Zeeman Aufspaltung mit einer modifizierten Brillouinfunktion an die experimentellen Daten bestimmt. Dieser Wert für die Mn Konzentration zeigt eine gute Einbindung des Mn in das Basismaterial.

Die magnetischen Eigenschaften der (Zn,Mn)Se Schicht wurde in einem Quantum Design superconducting quantum interference device (SQUID) Magnetometer charakterisiert. Selbst in der höchsten Auflösung des SQUIDs wurde keine Hysterese entdeckt.

Die Daten passen gut zu einer modifizierten Brillouinfunktion, welche bekannt dafür ist, die funktionale Abhängigkeit der Magnetisierung vom Feld für (Zn,Mn)Se zu beschreiben. Von diesem Fit konnte ein effektiver Temperaturparameter Te [GPF79], welcher ein Indikator für die Mn Konzentration ist, bestimmt werden. Die magnetischen Daten waren vollständig konsistent mit einer guten Einbindung von Mn in das ZnSe Gitter.

Elektrische Messungen von hochdotierten (Zn,Mn)Se Schichten und des (Zn,Mn)Se/Si (100) Übergangs wurden bei verschiedenen Temperaturen durchgeführt. Die Schichten zeigten lineare Transportcharakteristiken, auch wenn die Kontaktierung der Schichten sich selbst mit insitu Technichen als schwierig erwiesen hat. Trotz des starken Schottky-Dioden-artigen Verhaltens am Übergang kann spinpolarisierter Transport eventuell möglich sein.

Bibliography

[ABJ^{+}90] O. L. Alerhand, A. Nihat Berker, J. D. Joannopoulos, David Vanderbilt, R. J. Hamers, and J. E. Demuth. Finite-temperature phase diagram of vicinal si(100) surfaces. *Phys. Rev. Lett.*, 64(20):2406, 1990.

[AEK^{+}00] Kenta Arima, Katsuyoshi Endo, Toshihiko Kataoka, Yasushi Oshikane, Haruyuki Inoue, and Yuzo Mori. Atomically resolved scanning tunneling microscopy of hydrogen-terminated Si(001) surfaces after HF cleaning. *Appl. Phys. Lett.*, 76:463, 2000.

[AKP^{+}06] G.V. Astakhov, T. Kiessling, A.V. Platonov, T. Slobodskyy, S. Mahapatra, W. Ossau, G. Schmidt, K. Brunner, and L.W. Molenkamp. Circular-to-linear and linear-to-circular conversion of optical polarization by semiconductor quantum dots. *Phys. Rev. Lett.*, 96:027402, 2006.

[BBK^{+}86] R. B. Bylsma, W. M. Becker, J. Kossut, U. Debska, and D. Yoder-Short. Dependence of the energy gap on x and t in ZnMnSe: The role of exchange interaction. *Phys. Rev. B*, 33:8207, 1986.

[BBS91] R. D. Bringans, D. K. Biegelsen, and L.-E. Swartz. Atomic-step rearrangement on si(100) by interaction with arsenic and the implication for gaas-on-si epitaxy. *Phys. Rev. B*, 44(7):3054, 1991.

[BBS^{+}92] R. D. Bringans, D. K. Biegelsen, L.-E. Swartz, F. A. Ponce, and J. C. Tramontana. Effect of interface chemistry on the growth of ZnSe on the Si(100) surface. *Phys. Rev. B*, 45:13400, 1992.

[BME78] K. Britze and G. Meyer-Ehmsen. High energy electron diffraction at Si(001) surfaces. *Surface Science*, 77:131, 1978.

[CC76] James R. Chelikowsky and Marvin L. Cohen. Nonlocal pseudopotential calculations for the electronic structure of eleven diamond and zinc-blende semiconductors. *Phys. Rev. B*, 14:566, 1976.

[Cha87] D. J. Chadi. Stabilities of single-layer and bilayer steps on si(001) surfaces. *Phys. Rev. Lett.*, 59(15):1691, 1987.

[Cha94] D. J. Chadi. Doping in znse, znte, mgse, and mgte wide-band-gap semiconductors. *Phys. Rev. Lett.*, 72:534–537, 1994.

[CMC86] Federico Capasso, Khalid Mohammed, and Alfred Y. Cho. Sequential resonant tunneling through a multiquantum well superlattice. *Appl. Phys. Lett.*, 48:478, 1986.

[CNCRF$^+$98] M. E. Constantino, H. Navarro-Contreras, G. Ramirez-Flores, M. A. Vidal, A. Lastras-Martinez, I. Hernandez-Calderon, O. de Melo, and M. Lopez-Lopez. Observation of stress effects on GaAs at the interface of molecular beam epitaxy grown ZnSe/GaAs(100) heterostructures. *Applied Surface Science*, 134:95, 1998.

[CSBB94] G. Cohen-Solal, F. Bailly, and M. Barbe. Critical thickness in heteroepitaxial growth of zinc-blende semiconductor compounds. *Journal of Crystal Growth*, 138:68, 1994.

[CSY00] M.S. Carroll, J.C. Sturm, and M. Yang. Low-temperature preparation of oxygen- and carbon-free silicon-germanium surfaces for silicon and silicon-germanium epitaxial growth by rapid thermal chemical vapor deposition. *J. Electrochem. Soc.*, 147:4652–4659, 2000.

[CTF00] C. Chauvet, E. Tournieé, and J.-P. Faurie. Nature of the band gap in $Zn_{1-x}Be_xSe$ alloys. *Phys. Rev. B*, 61:5332, 2000.

[CW92] Y. W. Choi and C. R. Wie. Increased peak current in alas/gaas resonant tunneling structures with $GaInAs$ emitter spacer. *Journal of Applied Physics*, 71(4):1853–1859, 1992.

[DA91] A. R. Denton and N. W. Ashcroft. Vegard's law. *Phys. Rev. A*, 43(6):3161, Mar 1991.

[DALS$^+$05] B. Daniel, K. C. Agarwal, J. Lupaca-Schomber, C. Klingshirn, and M. Hetterich. Carrier concentration, mobility, and electron effective mass in chlorine-doped n-type $\mathrm{Zn}_{1-x}\mathrm{Mn}_x\mathrm{Se}$ epilayers grown by molecular-beam epitaxy. *Appl. Phys. Lett.*, 87:212103, 2005.

[DHR77] Michael B. Dowell, Carl A. Hultman, and Gerd M. Rosenblatt. Determination of slopes of microscopic surface features by Nomarski polarization interferometry. *Review of Scientific Instruments*, 48:1491, 1977.

[DiV99] David P. DiVincenzo. Quantum computing and single-qubit measurements using the spin-filter effect (invited). *J. Appl. Phys.*, 85:4785, 1999.

[DKK85] R. A. Davies, M. J. Kelly, and T. M. Kerr. Tunneling between two strongly coupled superlattices. *Phys. Rev. Lett.*, 55(10):1114–1116, Sep 1985.

[dWM86] Chris G. Van de Walle and Richard M. Martin. Theoretical calculations of heterojunction discontinuities in the Si/Ge system. *Phys. Rev. B*, 34(8):5621–5634, Oct 1986.

[EAK+98] Katsuyoshi Endo, Kenta Arima, Toshihiko Kataoka, Yasushi Oshikane, Haruyuki Inoue, and Yuzo Mori. Atomic structures of hydrogen-terminated Si(001) surfaces after wet cleaning by scanning tunneling microscopy. *Appl. Phys. Lett.*, 73:1853, 1998.

[EC90] D. J. Eaglesham and M. Cerullo. Dislocation-free stranski-krastanow growth of ge on si(100). *Phys. Rev. Lett.*, 64(16):1943–1946, Apr 1990.

[EHC91] D. J. Eaglesham, G. S. Higashi, and M. Cerullo. 370 °C clean for Si molecular beam epitaxy using a HF dip. *Applied Physics Letters*, 59:685, 1991.

[FAFF99] Mitsuru Funato, Satoshi Aoki, Shizuo Fujita, and Shigeo Fujita. Tunable band offsets via control of interface atomic configuration in GaAs-on-ZnSe.001. heterovalent heterostructures. *J. Appl. Phys.*, 85(3):1514, 1999.

[FG59] G. Feher and E. A. Gere. Electron Spin Resonance Experiments on Donors in Silicon. II. Electron Spin Relaxation Effects. *Phys. Rev.*, 114(5):1245–1256, Jun 1959.

[FJ01] A. Fert and H. Jaffrès. Conditions for efficient spin injection from a ferromagnetic metal into a semiconductor. *Phys. Rev. B*, 64(18):184420, Oct 2001.

[FKR+99] R. Fiederling, M. Keim, G. Reuscher, W. Ossau, G. Schmidt, A. Waag, and L. W. Molenkamp. Injection and detection of a spin-polarized current in a light emitting diode. *Nature*, 402:787, 1999.

[Fur88] J. K. Furdyna. Diluted magnetic semiconductors. *Journal of Applied Physics*, 64(4):R29–R64, 1988.

[GaAFL+00] C. Guenaud, E. Deleporte adn A. Filoramo, Ph. Lelong, C. Delalande C. Morhain, E. Tournie, and J. P. Faurie. Study of the band alignment in (Zn, Cd)Se/ZnSe quantum wells by means of photoluminescence excitation spectroscopy. *Journal of Applied Physics*, 87:1863, 2000.

[Gai94] J. M. Gaines. In-situ characterization of II/VI molecular beam epitaxy growth using reflection high-energy electron diffraction oscillations. *Journal of Crystal Growth*, 137:187, 1994.

[GF01] S. Gundel and W. Faschinger. First-principles calculation of p-type doping of znse using nitrogen. *Phys. Rev. B*, 65(3):035208, 2001.

[GGM+85] L. Goldstein, F. Glas, J. Y. Marzin, M. N. Charasse, and G. Le Roux. Growth by molecular beam epitaxy and characterization of InAs/GaAs strained-layer superlattices. *Appl. Phys. Lett.*, 47:1099, 1985.

[GKF+01] Th. Gruber, M. Keim, R. Fiederling, G. Reuscher, W. Ossau, G. Schmidt, and L. W. Molenkamp. Electron spin manipulation using semimagnetic resonant tunneling diodes. *Appl. Phys. Lett.*, 78:1101, 2001.

[GPF79] J. A. Gaj, R. Planel, and G. Fishman. Relation of magneto-optical properties of free exitons to spin alignment of Mn^{2+} ions in $Cd_{1-x}Mn_xTe$. *Solid State Commun.*, 29:435, 1979.

[GSS$^+$04] C. Gould, A. Slobodskyy, T. Slobodskyy, P. Grabs, C. R. Becker, G. Schmidt, and L. W. Molenkamp. Magnetic resonant tunnelling diodes as voltage-controlled spin selectors. 241:700, 2004.

[GSS$^+$06] C. Gould, A. Slobodskyy, D. Supp, T. Slobodskyy, P. Grabs, P. Hawrylak, F. Qu, G. Schmidt, and L.W. Molenkamp. Remanent Zero Field Spin Splitting of Self-Assembled Quantum Dots in a Paramagnetic Host. *Phys. Rev. Lett.*, 97:017202, 2006.

[GTC87] V. J. Goldman, D. C. Tsui, and J. E. Cunningham. Evidence for lo-phonon-emission-assisted tunneling in double-barrier heterostructures. *Phys. Rev. B*, 36:7635–7637, 1987.

[Has02] J E Hasbun. Conductance in double quantum well systems. *J. Phys.: Condens. Matter*, 14:R143–R175, 2002.

[HBC$^+$99] M. M. Heyns, T. Bearda, I. Cornelissen, S. De Gendt, R. Degraeve, G. Groeseneken, C. Kenens, D. M. Knotter, L. M. Loewenstein, P. W. Mertens, S. Mertens, M. Meuris, T. Nigam, M. Schaekers, I. Teerlinck, W. Vandervorst, R. Vos, and K. Wolke. Cost-effective cleaning and high-quality thin gate oxides. *IBM Journal of Research and Development*, 43 (3):339, 1999.

[HBH$^+$03] T. E. Harveya, K. A. Bertnessa, R. K. Hickernella, C.M. Wangb, and J. D. Splett. Accuracy of AlGaAs growth rates and composition determination using RHEED oscillations. *J. Crystal Growth*, 251:73, 2003.

[HGQ91] Pawel Hawrylak, Marek Grabowski, and J. J. Quinn. Tunneling in a periodic array of semimagnetic quantum dots. *Phys. Rev. B*, 44(23):13082, Dec 1991.

[HK01] M. K. Hudait and S. B. Krupanidhi. Self-annihilation of antiphase boundaries in GaAs epilayers on Ge substrates grown by metal-organic vapor-phase epitaxy. *Journal of Applied Physics*, 89:5972, 2001.

[HPS$^+$97] S. Heun, J. J. Paggel, L. Sorba, S. Rubini, A. Franciosic, J.-M. Bonardd, and J.-D. Ganie‘re. Interface composition and stacking fault density in II-VI/III-V heterostructures. *Appl. Phys. Lett.*, 70:237, 1997.

[Ide95] Takashi Ide. Formation of step structures by as deposition on a double-domain si(001) substrate. *Phys. Rev. B*, 51(3):1722, 1995.

[IM] K. M. Indlekofer and J. Malindretos. ”wingreen simulation package v2.1”, http://www.fz-juelich.de/isg/mbe/wingreen.html.

[IS86] A. Ishizaka and Y. Shiraki. Low temperature surface cleaning of silicon and its application to silicon MBE. *Journal of the Electrochemical Society*, 133:666, 1986.

[JWS$^+$05] X. Jiang, R. Wang, R. M. Shelby, R. M. Macfarlane, S. R. Bank, J. S. Harris, , and S. S. Parkin. Highly Spin-Polarized Room-Temperature Tunnel Injector for Semiconductor Spintronics using MgO(100). *Phys. Rev. Lett.*, 94:056601, 2005.

[KBN$^+$96] Lutz Kipp, D. K. Biegelsen, J. E. Northrup, L.-E. Swartz, and R. D. Bringans. Reflectance Difference Spectroscopy: Experiment and Theory for the Model System Si(001):As and Application to Si(001). *Phys. Rev. Lett.*, 76:2810–2813, 1996.

[KKL$^+$00] M. Kim, C. S. Kim, S. Lee, J. K. Furdyna, and M. Dobrowolska. Band offset determination in ZnSe-based heterostructures involving ZnBeSe. *Journal of Crystal Growth*, 214-215:325, 2000.

[KM83] A. D. Katnani and G. Margaritondo. Microscopic study of semiconductor heterojunctions: Photoemission measurement of the valance-band discontinuity and of the potential barriers. *Phys. Rev. B*, 28(4):1944–1956, Aug 1983.

[KOT$^+$01] Makoto Kohda, Yuzo Ohno, Koji Takamura, Fumihiro Matsukura, and Hideo Ohno. A Spin Esaki Diode. *Jpn. J. Appl. Phys.*, 40:L1274, 2001.

[KP70] W. Kern and D. A. Poutinen. Cleaning solutions based on hydrogen peroxide for use in silicon semiconductor technology. *RCA REVIEW*, 31 (2):187, 1970.

[Kro87] Herbert Kroemer. Polar-on-nonpolar epitaxy. *Journal of Crystal Growth*, 81:193, 1987.

[KYK$^+$02] D. Keller, D. R. Yakovlev, B. König, W. Ossau, Th. Gruber, A. Waag, L. W. Molenkamp, and A. V. Scherbakov. Heating of the magnetic ion system in (Zn,Mn)Se/(Zn,Be)Se semimagnetic quantum wells by means of photoexcitation. *Phys. Rev. B*, 65:035313, 2002.

[LAE$^+$89] M. L. Leadbeater, E.S. Alves, L. Eaves, M. Henini, O.H. Hughes, A. Celeste, J.C. Portal, G. Hill, and M.A. Pate. Magnetic field studies of elastic scataring and optic-phonon emission in resonant-tunneling devices. *Phys. Rev. B*, 39:3438, 1989.

[LB99] Landolt-Börnstein. *II-VI and I-VI Compounds; Semimagnetic Compounds*, volume III, chapter 41b. Springer, Berlin, 1999.

[LdWNP91] D. B. Laks, C. G. Van de Walle, G. F. Neumark, and S. T. Pantelides. Role of native defects in wide-band-gap semiconductors. *Phys. Rev. Lett.*, 66:648–651, 1991.

[Leh05] Frank Lehmann. *Prozessierung und elektrische Charakterisierung von ZnSe Heterostrukturen in verschiedenen Messgeometrien zum eindeutigen Nachweis der elektrischen Spininjektion*. PhD thesis, Bayerisches Julius-Maximilians-Universität Würzburg, 2005.

[LGD$^+$06] D. Litvinov, D. Gerthsen, B. Daniel, C. Klingshirn, and M. Hetterich. Defects and phase distribution in epitaxial ZnMnSe layers analyzed by transmission electron microscopy. *J. Appl. Phys.*, 100:023523, 2006.

[LLV02] S Lavagne, C Levade, and G Vanderschaeve. <310> misfit dislocations in ZnSe/GaAs(001) heterostructure. *J. Phys.: Condens. Matter*, 14:13291–13298, 2002.

[LMS$^+$94] M. L. F. Lerch, A. D. Martin, P. E. Simmonds, L. Eaves, and M. L. Leadbeater. A new technique for directly probing the intrinsic tristability and its temperature dependence in a resonant tunneling diode. *Solid-State Electronics*, 37:961, 1994.

[LP94] D. Li and M. D. Pashley. Znse nucleation on the gaas001-se2x1 surface observed by scanning tunneling microscopy. *J Vac Sci Technol B*, 12:2547, 1994.

[LPB$^+$05] Qiming Li, Belliappa Pattada, Steve R. J. Brueck, Stephen Hersee, and Sang M. Han. Morphological evolution and strain relaxation of Ge islands grown on chemically oxidized Si(100) by molecular-beam epitaxy. *J. Appl. Phys.*, 98:073504, 2005.

[LS86] Serge Luryi and Ephraim Suhir. New approach to the high quality epitaxial growth of lattice-mismatched materials. *Appl. Phys. Lett.*, 46:140, 1986.

[MB96] Z Mitura and J L Beeby. Theoretical studies on the quantitative interpretation of RHEED data. *J. Phys.: Condens. Matter*, 8:8717, 1996.

[MBC$^+$96] L. D. Macks, S. A. Brown, R. G. Clark, R. P. Starrett, M. A. Reed, M. R. Deshpande, C. J. L. Fernando, and W. R. Frensley. Resonant tunneling in double-quantum-well triple-barrier heterostructures. *Phys. Rev. B*, 54:4857, 1996.

[MBV91] Andrea K. Myers-Beaghton and Dinitri D. Vvedensky. Generalized Burton-Cabrera-Frank theory for groeth and equilibration on stepped surfaces. *Physical review A*, 44:2457, 1991.

[MLSE94] A. D. Martin, M. L. F. Lerch, P. E. Simmonds, and L. Eaves. Observation of intrinsic tristability in a resonant tunneling sructure. *Appl. Phys. Lett.*, 64:1248–1250, 1994.

[Moo65] G.E. Moore. Cramming more components onto integrated circuits. *Electronics*, 38 (8), 1965.

[MSaFL$^+$04] S. Maximov, T. Slobodskyy, A. Gröger adn F. Lehmann, P. Grabs, L. Hansen, C. R. Becker, C. Gould, G. Schmidt, and L.W. Molenkamp. Micro-patterned (Zn,Be)Se/(Zn,Mn)Se resonant tunnelling diodes. *Semicond. Sci. Technol.*, 19:946, 2004.

[MWD03] *Merriam-Webster's Collegiate Dictionary, 11th Edition.* 2003.

[NHJ+87] D. W. Nam, N. Holonyak, K. C. Hsieh Jr., R. W. Kaliski, J. W. Lee, H. Shichijo, J. E. Epler, R. D. Burnham, and T. L. Paoli. Stable continuous room-temperature laser operation of $\mathrm{Al}_x\mathrm{Ga}_{1-x}\mathrm{As}$-GaAs quantum well heterostructures grown on Si. *Appl. Phys. Lett.*, 51:39, 1987.

[NIKO86] T. Nakagawa, H. Imamoton, T. Kojima, and K. Ohta. Observation of resonant tunneling in algaas/gaas triple barrier diodes. *Appl. Phys. Lett.*, 49:73, 1986.

[NVM+94] R. Nicolini, L. Vanzetti, Guido Mula, G. Bratina, L. Sorba, and A. Franciosi. Local Interface Composition and Band Discontinuities in Heterovalent Heterostructures. *Phys. Rev. Lett.*, 72:294, 1994.

[PC87] P. R. Pukite and P. I. Cohen. Suppression of antiphase domains in the growth of GaAs on Ge(100) by molecular beam epitaxy. *J. Appl. Phys.*, 81:214, 1987.

[PC95] C. H. Park and D. J. Chadi. First-principles study of DX centers in CdTe, ZnTe, and $\mathrm{Cd}_x\mathrm{Zn}_{1-x}\mathrm{Te}$ alloys. *Phys. Rev. B*, 52:11884, 1995.

[Pet86] P. M. Petroff. Nucleation and growth of GaAs on Ge and the structure of antiphase boundaries. *J. Vac. Sci. Technol. B*, 4:874, 1986.

[PJJ+98] K. Pinardi, U. Jain, S. C. Jain, H. E. Maes, R. Van Overstraeten, and M. Willander. Critical thickness and strain relaxation in lattice mismatched II–VI semiconductor layers. *J. Appl. Phys.*, 83:4724, 1998.

[PTY+03] V. I. Perel’, S. A. Tarasenko, I. N. Yassievich, S. D. Ganichev, V. V. Bel’kov, and W. Prettl. Spin-dependent tunneling through a symmetric semiconductor barrier. *Phys. Rev. B*, 67:201304, 2003.

[QH05] Fanyao Qu and Pawel Hawrylak. Magnetic Exchange Interactions in Quantum Dots Containing Electrons and Magnetic Ions. *Phys. Rev. Lett.*, 95:217206, 2005.

[Ras00] E. I. Rashba. Theory of electrical spin injection: Tunnel contacts as a solution of the conductivity mismatch problem. *Phys. Rev. B*, 62(24):R16267–R16270, Dec 2000.

[RC87] Ying-Chao Ruan and W. Y. Ching. An effective dipole theory for band lineups in semiconductor heterojunctions. *Journal of Applied Physics*, 62:2885, 1987.

[Reß98] Heiko Roland Reß. *NEUE MESSMETHODEN IN DER HOCHAUFLÖSENDEN RÖNTGENDIFFRAKTOMETRIE*. PhD thesis, Bayerisches Julius-Maximilians-Universität, 1998.

[Reu00] Frank Reuß. Heteroepitaxie von II-VI-Verbindungshalbleitern auf Silizium und Germanium. Master’s thesis, Physikalisches Institut der Julius-Maximilians-Universität Würzburg, 2000.

[RH99] M. B. Raschke and U. Höfer. Equilibrium and nonequilibrium hydrogen coverages on vicinal Si(001) surfaces: Diffusion barriers and binding energies. *Phys. Rev. B*, 59(4):2783–2789, Jan 1999.

[RWWE96] J. Riley, D. Wolfframm, D. Westwood, and A. Evans. Studies in the growth of ZnSe on GaAs(001). *Journal of Crystal Growth*, 160(3-4):193–200, March 1996.

[SAD+99] A. Souifi, R. Adhiri, R. Le Dantec, G. Guillot, P. Uusimaa, A. Rinta-Moykky, and M. Pessa. ZnSe/GaAs band-alignment determination by deep level transient spectroscopy and photocurrent measurements. *JOURNAL OF APPLIED PHYSICS*, 85:7759, 1999.

[SBTH88] C. J. Summers, K. F. Brennan, A. Torabi, and H. M. Harris. Resonant tunneling and negative differential resistance in a variably spaced superlattice energy filter. *Appl. Phys. Lett.*, 52:132, 1988.

[SCM+96] Werner Seifert, Niclas Carlsson, Mark Miller, Mats-Erik Pistol, Lars Samuelson, and L. Reine Wallenberg. In-situ growth of quantum dot structures by the Stranski-Krastanow growth mode. *Progress in Crystal Growth and Characterization of Materials*, 33:423, 1996.

[SFM+00] G. Schmidt, D. Ferrand, L. W. Molenkamp, A. T. Filip, and van B. J. Wees. Fundamental obstacle for electrical spin injection from a ferromagnetic metal into a diffusive semiconductor. *Phys. Rev. B*, 62(8):R4790–R4793, Aug 2000.

[SGS+03] A. Slobodskyy, C. Gould, T. Slobodskyy, C. R. Becker, G. Schmidt, and L.W. Molenkamp. Voltage-Controlled Spin Selection in a Magnetic Resonant Tunneling Diode. *Phys. Rev. Lett.*, 90:246601, 2003.

[SHG+99] D. Seghier, I. S. Hauksson, H. P. Gislason, K. A. Prior, and B. C. Cavenett. Evidence of strong effect from the interface on the electrical characteristics of ZnSe/GaAs heterojunctions. *J. Appl. Phys.*, 85:3721, 1999.

[SHP+02] R. M. Stroud, A. T. Hanbicki, Y. D. Park, G. Kioseoglou, A. G. Petukhov, B. T. Jonker, G. Itskos, and A. Petrou. Spin superlattice formation in ZnSe/ZnMnSe multilayers. *Phys. Rev. Lett.*, 89:166602, 2002.

[sim] One-dimensional Poisson/Schrödinger solver (SimWindows Semiconductor Device Simulator V.1.5).

[Sim63] John G. Simmons. Generalized formula for the electric tunnel effect between similar electrodes separated by a thin insulating film. *J. Appl. Phys.*, 34:1793, 1963.

[SK38] I. N. Stranski and L. Krastanov. Zur Theorie der orientierten Ausscheidung von Ionenkristallen aufeinander [eng-theory of orientation separation of ionic crystals]. *Sitzungsber. Wien. Akad. Wiss. Math.-Nat. Kl. IIb*, 146:797, 1938.

[SKW+06] M. Scheibner, T. A. Kennedy, L. Worschech, A. Forchel, G. Bacher, T. Slobodskyy, G. Schmidt, and L. W. Molenkamp. Coherent dynamics of locally interacting spins in self-assembled $Cd_{1-x}Mn_xSe$/ZnSe quantum dots. *Phys. Rev. B*, 73:081308(R), 2006.

[Slo05] Anatoliy Slobodskyy. *Resonant Tunneling Structures for spin manipulation*. PhD thesis, Bavarian Julius–Maximilians–Universität Würzburg, 2005.

[SRF+04] T. Slobodskyy, C. Rüster, R. Fiederling, D. Keller, C. Gould, W. Ossau, G. Schmidt, and L. W. Molenkamp. Molecular-beam epitaxy of (Zn,Mn)Se on Si(100). *Appl. Phys. Lett.*, 85:6215, 2004.

[SRG+01] G. Schmidt, G. Richter, P. Grabs, C. Gould, D. Ferrand, and L. W. Molenkamp. Large magnetoresistance effect due to spin injection into a nonmagnetic semiconductor. *Phys. Rev. Lett.*, 87:227203, 2001.

[SY92] V.I. Sugakov and S. A. Yazkevich. Electron tunneling through magnetically doped double barrier junction in parallel electric and magnetic fields. *Sov. Phys. pisma v JETP*, 18:15, 1992.

[Tak99] Masao Takahashi. Coherent-potential approach to magnetic and chemical disorder in diluted magnetic semiconductors. *Phys. Rev. BPhys. Rev. B*, 50:15858, 1999.

[TBN+91] M. C. Tamargo, M. J. S. P. Brasil, R. E. Nahory, R. J. Martin, A. L. Weaver, and H. L. Gilchrist. MBE growth of the (Zn,Cd)(Se,Te) system for wide-bandgap heterostructure lasers. *Semicond. Sci. Technol.*, 6:A8, 1991.

[TDD83] A. Twardowski, T. Dietl, and M. Demianiuk. The study of the s-d type exchange interaction in $Zn_{1-x}Mn_xSe$ mixed crystals. *Solid State Commun.*, 48:845, 1983.

[TIM+98] A. S. G. Thornton, T. Ihn, P. C. Main, L. Eaves, and M. Henini. Observation of spin splitting in single InAs self-assembled quantum dots in AlAs. *Appl. Phys. Lett.*, 73:354, 1998.

[TLAR03] A. M. Tyryshkin, S. A. Lyon, A. V. Astashkin, and A. M. Raitsimring. Electron spin relaxation times of phosphorus donors in silicon. *Phys. Rev. B*, 68:193207, 2003.

[TMM64] R. S. Title, G. Mandel, and F. F. Morehead. Self-compensation-limited conductivity in binary semiconductors. II. n-ZnTe. *Phys. Rev.*, 136(1A):A300–A302, Oct 1964.

[TRHC90] G. W. Trucks, Krishnan Raghavachari, G. S. Higashi, and Y. J. Chabal. Mechanism of HF etching of silicon surfaces: A theoretical understanding of hydrogen passivation. *Phys. Rev. Lett.*, 65:504, 1990.

[TSY85] Masahiro Tsuchiya, Hiroyuki Sakaki, and Junji Yoshino. Room Temperature Observation of Differential Negative Resistance in an AlAs/GaAs/AlAs Resonant Tunneling Diode. *Jpn. J. Appl. Phys.*, 24:L466, 1985.

[TvODP84] A. Twardowski, M. von Ortenberg, M. Demianiuk, and R. Pauthenet. Magnetization and exchange constants in $Zn_{1-x}Mn_xSe$. *Solid State Communications*, 51(11):849–852, 1984.

[VDDZ06] G. Vanamu, A. K. Datye, R. Dawson, and Saleem H. Zaidi. Growth of high-quality GaAs on Ge/$\mathrm{Si}_{1-x}\mathrm{Ge}_x$ on nanostructured silicon substrates. *Appl. Phys. Lett.*, 88:251909, 2006.

[VLP$^+$00] E. E. Vdovin, A. Levin, A. Patanè, L. Eaves, P. C. Main, Yu. N. Khanin, Yu. V. Dubrovskii, M. Henini, and G. Hill. Imaging the electron wave function in self-assembled quantum dots. *Science*, 290:122, 2000.

[VS06] Alexander Valladares and A P Sutton. First principles simulations of antiphase defects on the SP 90^O partial dislocation in silicon. *J. Phys.: Condens. Matter*, 18:3735–3744, 2006.

[WC91] C. R. Wie and Y. W. Choi. Designing resonant tunneling structures for increased peak current density. *Appl. Phys. Lett.*, 58(10):1077–1079, 1991.

[WEWR00] D. Wolfframm, D. A. Evans, D. I. Westwood, and J. Riley. A detailed surface phase diagram for ZnSe MBE growth and ZnSe/GaAs(0 0 1) interface studies. *Journal of Crystal Growth*, 216:119, 2000.

[WON$^+$00] L. Worschech, W. Ossau, J. Nürnberger, W. Faschinger, and G. Landwehr. Optical characterization of relaxation processes in nitrogen-doped ZnSe layers. *Appl. Phys. Lett.*, 77(26):4301, 2000.

[WZ98] Su-Huai Wei and Alex Zunger. Calculated natural band offsets of all II–VI and III–V semiconductors: Chemical trends and the role of cation d orbitals. *Appl. Phys. Lett.*, 72:2011, 1998.

[XVS$^+$88] F. Xu, M. Vos, J. P. Sullivan, Lj. Atanasoska, Steven G. Anderson, J. H. Weaver, and H. Cheng. Band-gap discontinuities for Ge/ZnSe(100) and Si/ZnSe(100): A photoemission study. *Phys. Rev. B*, 38(11):7832–7835, Oct 1988.

[YAC$^+$86] E. Yablonovitch, D. L. Allara, C. C. Chang, T. Gmitter, and T. B. Bright. Unusually low surface-recombination velocity on silicon and germanium surfaces. *Phys. Rev. Lett.*, 57(2):249–252, Jul 1986.

[YSP$^+$97] W. Y. Yu, M. S. Salib, A. Petrou, B. T. Jonker, and J. Warnock. Band alignment in ZnSe/ZnCdMnSe quantum-well structures. *Phys. Rev. B*, 55:1602, 1997.

[YT97] Takashi Yokoyama and Kunio Takayanagi. Dimer buckling induced by single-dimer vacancies on the Si(001) surface near T_C. *Phys. Rev. B*, 56:10483, 1997.

[YTF$^+$95] W. Y. Yu, A. Twardowski, L. P. Fu, A. Petrou, and B. T. Jonker. Magnetoanisotropy in $\mathrm{Zn}_{1-x}\mathrm{Mn}_x\mathrm{Se}$ strained epilayers. *Phys. Rev. B*, 51:9722, 1995.

[ZLEKEA99] Xinglin Zeng, Bo Lin, Ibrahim El-Kholy, and Hani E. Elsayed-Ali. Time-resolved reflection high-energy electron diffraction study of the $ge(111)-c(2\times 8)-(1\times 1)$ phase transition. *Phys. Rev. B*, 59(23):14907, Jun 1999.

[ZWZ98] S. B. Zhang, Su-Huai Wei, and Alex Zunger. A phenomenological model for systematization and prediction of doping limits in II–VI and I–III–VI$_2$ compounds. *Journal of Applied Physics*, 83:3192, 1998.

List of publications

i. *Remanent Zero Field Spin Splitting of Self-Assembled Quantum Dots in a Paramagnetic Host* C. Gould, A. Slobodskyy, D. Supp, T. Slobodskyy, P. Grabs, P. Hawrylak, F. Qu, G. Schmidt, and L. W. Molenkamp **Phys. Rev. Lett. 97, 017202 (2006)**

ii. *Circular-to-Linear and Linear-to-Circular Conversion of Optical Polarization by Semiconductor Quantum Dots* G. V. Astakhov, T. Kiessling, A. V. Platonov, T. Slobodskyy, S. Mahapatra, W. Ossau, G. Schmidt, K. Brunner, and L. W. Molenkamp **Phys. Rev. Lett. 96, 027402 (2006)**

iii. *Electric field control of magnetization dynamics in ZnMnSe/ZnBeSe diluted-magnetic-semiconductor heterostructures* M. K. Kneip, D. R. Yakovlev, and M. Bayer, T. Slobodskyy, G. Schmidt, and L. W. Molenkamp **Appl. Phys. Lett. 88, 212105 (2006)**

iv. *Anomalous in-plane magneto-optical anisotropy of self-assembled quantum dots* T. Kiessling, A. V. Platonov, G. V. Astakhov, T. Slobodskyy, S. Mahapatra, W. Ossau, G. Schmidt, K. Brunner, and L. W. Molenkamp **Phys. Rev. B 74, 041301(R) (2006)**

v. *Coherent dynamics of locally interacting spins in self-assembled* $Cd_{1-x}Mn_xSe/ZnSe$ *quantum dots* M. Scheibner, T. A. Kennedy, L. Worschech, A. Forchel, G. Bacher, T. Slobodskyy, G. Schmidt, and L. W. Molenkamp **Phys. Rev. B 73, 081308(R) (2006)**

vi. *Enhanced Zn–Cd interdiffusion and biexciton formation in self-assembled CdZnSe quantum dots in thermally annealed small mesas* E. Margapoti, L. Worschech, A. Forchel, T. Slobodskyy, and L. W. Molenkamp **J. Appl. Phys. 100, 113111 (2006)**

vii. *Optical anisotropy of CdSe/ZnSe quantum dots* T. Kiessling, G. V. Astakhov, A. V. Platonov, T. Slobodskyy, S. Mahapatra, W. Ossau, G. Schmidt, K. Brunner, L. W. Molenkamp **Phys. stat. sol. (c) 3, No. 4, 912 (2006)**

viii. *Thermal annealing of self-assembled CdZnSe quantum dots studied by photoluminescence spectroscopy* E. Margapoti, L. Worschech, T. Slobodskyy, L. W. Molenkamp, A. Forchel **Phys. stat. sol. (c) 3, No. 4, 920 (2006)**

ix. *Energy relaxation in CdSe/ZnSe quantum dots under the strong exciton-phonon coupling regime* A. V. Platonov, T. Kiessling, G. V. Astakhov, A. A. Maksimov, A. V. Larionov, D. R. Yakovlev, T. Slobodskyy, S. Mahapatra, W. Ossau, G. Schmidt, K. Brunner, M. Bayer, L. W. Molenkamp **Phys. stat. sol. (c) 3, No. 4, 924 (2006)**

x. *Magneto-optics of two-dimensional electron gases modified by strong Coulomb interactions in ZnSe quantum wells* D. Keller, D. R. Yakovlev, G. V. Astakhov, W. Ossau, S. A. Crooker, T. Slobodskyy, A. Waag, G. Schmidt, and L. W. Molenkamp **Phys. Rev. B 72, 235306 (2005)** (12 pages)

xi. *Molecular-beam epitaxy of (Zn,Mn)Se on Si(100)* T. Slobodskyy, C. Rüster, R. Fiederling, D. Keller, C. Gould, W. Ossau, G. Schmidt, and L. W. Molenkamp **Appl. Phys. Lett. 85, 6215 (2004)**

xii. *Micro-patterned (Zn,Be)Se/(Zn,Mn)Se resonant tunnelling diodes* S. Maximov, T. Slobodskyy, A. Gröger, F. Lehmann, P. Grabs, L. Hansen, C. R. Becker, C. Gould, G. Schmidt and L. W. Molenkamp **Semicond. Sci. Technol. 19 946 (2004)**

xiii. *Magnetic resonant tunneling diodes as voltage-controlled spin selectors* C. Gould, A. Slobodskyy, T. Slobodskyy, P. Grabs, C. R. Becker, G. Schmidt, and L. W. Molenkamp **Phys. stat. sol. (b) 241, No. 3, 700 (2004)**

xiv. *Voltage-Controlled Spin Selection in a Magnetic Resonant Tunneling Diode* A. Slobodskyy, C. Gould, T. Slobodskyy, C. R. Becker, G. Schmidt, and L. W. Molenkamp **Phys. Rev. Lett. 90, 246601 (2003)**

Curriculum vitae

- Taras Slobodskyy
- **PERSONAL DATA**
- Address: Petrinistrasse 21, 97080 Würzburg
  Email: tslob@physik.uni-wuerzburg.de
  Date of birth: 24.10.1976
  Place of birth: Ivano-Frankivsk, Ukraine
- **PROFESSIONAL EXPERIENCE**
- from Jan 2002: Julius Maximilians Universität Würzburg,
  - *Scientific staff member and IT administrator* at the chair of experimental physics III, supervisor: Prof. Laurens Molenkamp
- Sept 1999 to Dec 2001: Institute of Material Sciences Problems NAS of Ukraine,
  - *Scientific staff member* at the Chernivtsi Department, supervisor: Prof. Zakhar Kovaluk
- Nov 1997 to Sept 1999: City council, Chernivtsi city, Ukraine,
  - *Information Technology advisor* of the mayor
- Sept 1997 to July 1999: Gymnasium N5, Chernivtsi city, Ukraine,
  - *Teacher*, Chief of educational section
- **EDUCATION**
- Sep 1994 to Aug 1999: **Master of sciences** at Y. Fedkovich Chernivtsi State University.
  - Diploma work “Properties of $Hg_3In_2Te_6$ doped by manganese”

Acknowledgements

To summarize all the years along my long way to gain the experience I poses now, I would like to mention those people who had the biggest influence on me.

First of all, I would like to thank to my twin-brother Dr. A. Slobodskyy, who has made my life comfortable by his presence and by his friendly spirit. Our, to the highest degree meaningful discussions, which have lasted for as long as I consciously remember, only strengthen my understanding the world.

I thank my parents (one of whom regretfully passed away) for their love and troubles, and my wife, who has motivated me and took care of our small daughter while I was writing this work.

I would like to thank Prof. Dr. L. W. Molenkamp for the possibility to work in his group and for the continuous support and supervision. The unique scientific atmosphere in the chair is, in most cases, inspired by his motivation and his scientific spirit.

Furthermore, I thank Priv. Doz. Dr. G. Schmidt, the chief of the spintronics group, for the supervision and support. Dr. A. Slobodskyy, Dr. C. Gould, D. Supp, Dr. C. Rüster and K. Pappert for the transport measurements and fruitful discussions of the results.

I would like to thank Dr. G. Astakhov, T. Kießling, Dr. D. Keller, Dr. R. Fiederling, E. Margepotti and M. Scheibner for the optical measurements and inspiring discussions of the results.

I thank Dr. P. Grabs, Dr. C. Schumacher, D. Groß, S. Mahapatra, F. Schmitt, Dr. I. Chado, J. Wenisch, P. Bach, V. Hock, Dr. Tanja Borzenko, A. Gebhardt, P. Wolf-Müller, R. Ebert and A. Schönteich for their sample preparation, processing, cooperation and the friendly environment in the lab.

In addition, I sincerely thank Prof. Dr. K. Brunner, Prof. Dr. W. Ossau, Prof. Dr. G. Karczewski, Prof Dr. G. Landwehr, Priv. Doz. Dr. H. Buhmann, Prof. Dr. J. Geurts, Dr. C. Kumpf, U. Bass, F. Lochner, Dr. G. Schott, M. König, M. Lentze and M. Leufgen.

My special thanks to the people not mentioned on this page.